

BRNO UNIVERSITY OF TECHNOLOGY

Faculty of Mechanical Engineering

MASTER'S THESIS

Brno, 2017

Bc. Mojmír Komora





# BRNO UNIVERSITY OF TECHNOLOGY

VYSOKÉ UČENÍ TECHNICKÉ V BRNĚ

## FACULTY OF MECHANICAL ENGINEERING

FAKULTA STROJNÍHO INŽENÝRSTVÍ

## INSTITUTE OF PHYSICAL ENGINEERING

ÚSTAV FYZIKÁLNÍHO INŽENÝRSTVÍ

# ENVIRONMENT-DEPENDENT SURFACE STRUCTURE OF FE<sub>2</sub>O<sub>3</sub>(012)

ZÁVISLOST POVRCHOVÉ STRUKTURY FE<sub>2</sub>O<sub>3</sub>(012) NA PROSTŘEDÍ

## MASTER'S THESIS

DIPLOMOVÁ PRÁCE

## AUTHOR

AUTOR PRÁCE

Bc. Mojmír Komora

## SUPERVISOR

VEDOUCÍ PRÁCE

doc. Ing. Jan Čechal, Ph.D.

BRNO 2017



# Specification Master's Thesis

Department: Institute of Physical Engineering  
Student: **Bc. Mojmír Komora**  
Study programme: Applied Sciences in Engineering  
Study field: Physical Engineering and Nanotechnology  
Leader: **doc. Ing. Jan Čechal, Ph.D.**  
Academic year: 2017/18

Pursuant to Act no. 111/1998 concerning universities and the BUT study and examination rules, you have been assigned the following topic by the institute director Master's Thesis:

## Environment–Dependent Surface Structure of Fe<sub>2</sub>O<sub>3</sub>(012)

### Concise characteristic of the task:

Purpose: The Fe<sub>2</sub>O<sub>3</sub>(012) surface, the low–energy, non–polar orientation of hematite, forms two terminations in UHV: a bulk–terminated (1×1) structure under oxidizing conditions, and a (2×1) reconstruction under reducing conditions. The response of these surface structures to various environments will be investigated.

Work plan: At TU Wien, the interaction of the surfaces with liquid water will be investigated with XPS, LEED, STM, and LEIS using the newly–designed ‘cold–finger’. As part of the project, the cleanliness of the cold finger dispenser and the transfer into UHV needs to be tested/established. A new Fe<sub>2</sub>O<sub>3</sub> single crystalline sample with appropriate dimensions will be prepared and characterized, and it will be used for the experiments to be conducted at BUT CEITEC.

At BUT CEITEC, LEEM will be used to study the phase transition from (1×1) to (2×1) during annealing in UHV. Further reduction to other surface phases will be investigated, as well as the influence of a reducing CO atmosphere (up to the highest pressure possible at the LEEM setup).

### Goals Master's Thesis:

- (1) Test the cleanliness of water drops prepared using the cold finger dispenser.
- (2) Describe the interaction of the Fe<sub>2</sub>O<sub>3</sub>(012) surface with liquid water.
- (3) Use LEEM to study the phase transitions on Fe<sub>2</sub>O<sub>3</sub>(012) during annealing in UHV and reduction in CO atmosphere.

### Recommended bibliography:

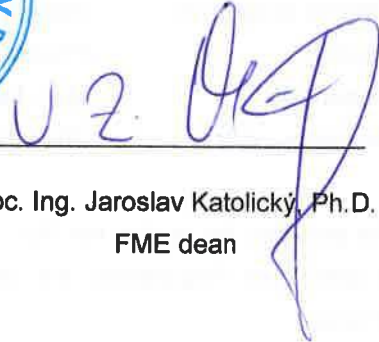
KRAUSHOFER, F, Master thesis 2016, Vienna University of Technology.

Students are required to submit the thesis within the deadlines stated in the schedule of the academic year 2017/18.

In Brno, 29. 10. 2017



prof. RNDr. Tomáš Škola, CSc.  
Director of the Institute



doc. Ing. Jaroslav Katolický, Ph.D.  
FME dean

## **ABSTRACT**

This thesis deals with study of  $\alpha$ -Fe<sub>2</sub>O<sub>3</sub>(012) exposed to water environment. The up to date knowledge of different oxides with focus on  $\alpha$ -Fe<sub>2</sub>O<sub>3</sub> and its R-cut (012) non polar surface is briefly reviewed. The experimental part of this work start with the description of the state of the art ultra high vacuum compatible experimental setup for dosing liquid water onto single crystal surfaces. Individual features of the system are thoroughly discussed and the tests of the system were performed on silver foil and on Fe<sub>3</sub>O<sub>4</sub>(001) single crystal surface. The chemical composition and surface morphology of the crystal after liquid water experiment is discussed. The proposed setup was used to study interaction of water with known (1×1) and (2×1) surface reconstruction of  $\alpha$ -Fe<sub>2</sub>O<sub>3</sub>(012). The experimental data shows that water binds to both reconstruction dissociatively with some molecular water bound to adsorbed hydroxyls. The (1×1) reconstruction appears to survive exposure to different pressures of water vapor, while the (2×1) seems to change into (1×1) after exposures to higher pressures or by exposing it to electron beam. Further, this thesis presents the first real time study of (1×1)-to-(2×1) transition by Low Energy Electron Microscopy. These results show initiation of the transition at atomic step edges and defects, which then continues to the centers of terraces at lower temperatures. Onservation of gradual transition at higher temperatures suggets creation of numerous nucleation centers from which then (2×1) spread. The beam damage is believed to also play role in the transformation as documented in the thesis.

## **KEYWORDS**

Condensation liquid water doser, cold finger, drop maker, oxides, iron oxides, Hematite,  $\alpha$ -Fe<sub>2</sub>O<sub>3</sub>(012), STM, LEEM, XPS, LEED, LEIS

## ABSTRAKT

Táto diplomová práca sa zaoberá štúdiom  $\alpha\text{-Fe}_2\text{O}_3(012)$  vystaveného vodnému prostrediu. Súčasný stav poznania ohľadom oxidov železa s pozornosťou vkladanou do popisu  $\alpha\text{-Fe}_2\text{O}_3$  a jeho (012) povrchu je stručne zhrnutá. Experimentálna časť tejto práce začína s popisom unikátného zariadenia na depozíciu kvapalnej vody na povrchy monokryštalických vzoriek kompatibilného s podmienkami ultra vysokého vákuua. Jednotlivé konštrukčné časti a detaily sú diskutované. Navrhnutý systém bol testovaný na vzorkách striebornej fólie a monokryštálu  $\text{Fe}_3\text{O}_4(001)$ . Chemické zloženie a morfológia povrchu po experimente s kvapalnou vodou je diskutovaná. Navrhnuté zariadenie bolo použité na štúdium interakcie vody so známymi  $(1\times 1)$  a  $(2\times 1)$  povrchovými  $\alpha\text{-Fe}_2\text{O}_3(012)$ . Experimentálne dáta ukazujú, že voda sa viaže na obe rekonštrukcie disociatívne s určitým množstvom molekulárnej vody naviazanej na adsorbované hydroxydi.  $(1\times 1)$  sa zdá javiť stabilná po expozícii rôznym tlakom vodnej pary, zatiaľ čo  $(2\times 1)$  vykazuje zmenu na  $(1\times 1)$  pri expozíciách vyšším tlakom vodnej pary alebo po niekoľko minútovej expozícii elektrónovému zväzku. Ďalej sú v tejto práci prezentované prvé výsledky z štúdie prechodu  $(1\times 1)$  rekonštrukcie na  $(2\times 1)$  pomocou mikroskopie nízkoenergiových elektrónov. Výsledky ukazujú, že táto premena na nižších teplotách je iniciovaná na hranách atomárnych vrstiev a defektov na povrchu, ktorá potom postupuje smerom k stredu atomárnych terás. Meranie na vyšších teplotách vykazuje postupnú premenu povrchu naznačujúcu viacero nukleačných centrech z ktorých sa  $(2\times 1)$  povrch širi ďalej.

## KLÍČOVÁ SLOVA

dávkovač kvapalnej vody kondezačného typu, vymrazovačka, oxidy, oxidy železa, Hematit,  $\alpha\text{-Fe}_2\text{O}_3(012)$ , STM, LEEM, XPS, LEED, LEIS

KOMORA, Mojmir. *Environment-Dependent Surface Structure of  $\alpha\text{-Fe}_2\text{O}_3(012)$* . [Master's Thesis]. Brno: Brno University of Technology, Faculty of Mechanical Engineering, Institute of Physical Engineering, 2018. 95 p. Supervised by doc. Ing. Jan Čechal, Ph.D.

## DECLARATION

I declare that I have elaborated my master's thesis on the theme of "Environment-Dependent Surface Structure of  $\alpha\text{-Fe}_2\text{O}_3(012)$ " independently, under the supervision of the master's thesis supervisor and with the use of technical literature and other sources of information which are all quoted in the thesis and detailed in the list of literature at the end of the thesis.

As the author of the master's thesis, I furthermore declare that, concerning the creation of this master's thesis, I have not infringed any copyright. In particular, I have not unlawfully encroached on anyone's personal copyright and I am fully aware of the consequences in the case of breaking Regulation § 11 and the following of the Copyright Act No 121/2000 Vol., including the possible consequences of criminal law resulted from Regulation § 152 of Criminal Act No 140/1961 Vol.

Brno .....

.....

(author's signature)



This work/Part of the work was carried out with the support of CEITEC Nano Research Infrastructure (ID LM2015041, MEYS CR, 2016–2019), CEITEC Brno University of Technology.

Financial support from the Thermo Fisher Scientific is gratefully acknowledged.

## Acknowledgement

This work was made possible by help and support of many people. First of all, I would like to thank Ing. Jan Balajka and Ing. Jiří Pavelec for their leadership and significant contribution to the cold finger project. Herbert and Rainer for their masterful skill and precision in production of the experimental setup. Dipl.-Ing. Florian Kraushofer and Ing. Pavel Procházka, PhD., who provided valuable advice and consultations on matter of iron oxides and Low Energy Electron Microscopy with great patience for often senseless questions and doc. Ing. Jan Čechal, PhD. for his excellent supervision since bachelor thesis. I'd like to thank prof. RNDr. Tomáš Šikola, Csc. and prof. Ulrike Diebold for making this project possible. Secondly, I'd like to thank all my classmates, especially Bc. Juraj Karlovský and Bc. Michal Andryšek for providing motivation and endless stream of good mood during often difficult times during work on Master's thesis. Last, but not least I'd like to thank my family for the support during my whole studies.

Bc. Mojmír Komora



# CONTENTS

<b>Motivation</b>	<b>1</b>
<b>1 Iron Oxides</b>	<b>3</b>
1.1 $\text{Fe}_{1-x}\text{O}$ (Wüstite)	3
1.1.1 Bulk Structure	4
1.2 $\text{Fe}_3\text{O}_4$ (Magnetite)	4
1.2.1 Bulk Structure	5
1.3 $\gamma\text{-Fe}_2\text{O}_3$ (Maghematite)	6
1.3.1 Bulk Structure	6
1.4 $\alpha\text{-Fe}_2\text{O}_3$ (Hematite)	6
1.4.1 Bulk Structure	7
1.4.2 $\alpha\text{-Fe}_2\text{O}_3$ (012) "R-cut" Surface	9
<b>2 Experimental Techniques</b>	<b>11</b>
2.1 Low Energy Electron Diffraction (LEED)	11
2.1.1 General Principle	11
2.1.2 Construction Design	13
2.1.3 Interpretation of the Diffraction Pattern	13
2.2 Low Energy Electron Microscopy (LEEM)	14
2.2.1 General Principle	14
2.2.2 Construction Design	15
2.2.3 Imaging Modes	16
2.3 X-ray Photoelectron Spectroscopy (XPS)	18
2.3.1 General Principle	18
2.3.2 Construction Design	19
2.3.3 Interpretation of the XPS Spectrum	20
2.4 Additional Experimental Techniques	22
2.4.1 Low Energy Ion Scattering (LEIS)	22
2.4.2 Scanning Tunneling Microscopy (STM)	23
<b>3 Design of Condensation Liquid Water dosing device</b>	<b>27</b>
3.1 General Principle	27
3.2 Condensation Liquid Water Dosing Device (Cold Finger)	29
3.2.1 Vacuum Connections	29
3.2.2 Heating and Temperature Measurement	30
3.2.3 Liquid Nitrogen Supply	33
3.2.4 Insulation	37

3.3	Experimental Setup . . . . .	39
3.3.1	Chamber for Liquid Water Dosing Experiments . . . . .	39
3.3.2	Sample Holder . . . . .	42
3.3.3	Cryo-Trap . . . . .	42
<b>4</b>	<b>Testing of the Experimental Setup</b>	<b>45</b>
4.1	Experimental Procedure . . . . .	45
4.2	Results of the Experimental Testing . . . . .	47
4.2.1	Ag Foil . . . . .	47
4.2.2	Fe <sub>3</sub> O <sub>4</sub> (001) . . . . .	50
4.3	Possible improvements of the Experimental setup . . . . .	57
4.4	Design Summary . . . . .	58
<b>5</b>	<b>α-Fe<sub>2</sub>O<sub>3</sub> (012) Surface Interaction with H<sub>2</sub>O</b>	<b>61</b>
5.1	Sample Preparation . . . . .	61
5.2	(1×1) Surface Reconstruction . . . . .	63
5.2.1	Surface Oxygen Exchange . . . . .	66
5.3	(2×1) Surface Reconstruction . . . . .	68
5.4	Discussion . . . . .	73
<b>6</b>	<b>α-Fe<sub>2</sub>O<sub>3</sub> (012) (1×1)-to-(2×1) Surface Reconstruction Transition</b>	<b>77</b>
6.1	Sample preparation . . . . .	77
6.1.1	Surface Inclusions . . . . .	77
6.2	(1×1)-to-(2×1) Surface Reconstruction reduction . . . . .	78
6.3	Discussion . . . . .	84
<b>7</b>	<b>Conclusion</b>	<b>85</b>
	<b>Bibliography</b>	<b>87</b>
	<b>List of symbols, physical constants and abbreviations</b>	<b>95</b>

## MOTIVATION

Iron and oxygen belong to the four most abundant elements in Earth's crust besides silicon and aluminum. The iron oxides form naturally by weathering the Fe containing rocks both on land and in the oceans. What is more, there has been reports that  $\alpha$ -Fe<sub>2</sub>O<sub>3</sub> is responsible for red hue on the Mars surface with analysis offering clues to the history of liquid water on the planet [1]. Here on Earth, the iron oxides can be found in various biological systems like the beaks of birds and to some extent in human brain.

Throughout the history, the iron oxide have played a vital role in development of the mankind, starting from pre-historic era, when men decorated the walls of caves with iron oxide containing pigments. The first experience with magnetism came from rocks containing Fe<sub>3</sub>O<sub>4</sub> in compasses for naval navigation from ancient China. By the 20th century, the iron oxides became front-runners in scientific research. The Fe<sub>3</sub>O<sub>4</sub> became the first crystallographic structure described by Bragg [2] or the first prototype for description of the theory of ferrimagnetism by Néel [3].

One of the most promising scientific area involving oxides ( $\alpha$ -Fe<sub>2</sub>O<sub>3</sub> and TiO<sub>2</sub>) is research of photoelectrochemical water splitting. This process uses semiconductor materials to convert solar energy directly to chemical energy in the form of hydrogen. The  $\alpha$ -Fe<sub>2</sub>O<sub>3</sub> has emerged as a promising candidate for such device due to its low cost, non toxicity and suitable band gap.

There have been various studies performed on a water-oxide surface interaction, which provided atomic level of insights on titanium oxide-water [5,6] or iron oxide-water [7–9] interface. However, majority of these experiments involved water in vapor phase. Experiments involving liquid water deposited on the sample in some cases require venting experimental setup, which usually done with inert gases (Ar,N) in order to limit contamination of samples by elements present in ambient air. However contaminants on sample can still be present by back streaming of the air in the flow of inert gas. Experimental setups for liquid water dosing experiments reported in literature, involve transferring sample out of vacuum system in flow of high purity Ar gas [5] or by exposing the samples to ambient air completely [6].

The previous experimental setup used at TU Vienna Surface Science Research group involved glass compartment coupled to load-lock of vacuum chamber with connection port for a drop maker, based on applying pressure through a syringe to form a drop on a pipete-like end [7]. Although this setup enables to interconnect Ultra high vacuum (UHV) chamber with electrochemical cell, the glass connections are not tight, which can in principle allow contaminants to enter the setup. Moreover, the possibility exist for contamination from glass parts by dissolution of glass [10], although it was not experimentally observed.

The part of the thesis was to redesign liquid water dosing experiment. To limit the possible contaminations UHV compatible experimental setup was built and tested. In this setup, water is transferred via vapor phase with only stainless steel coming into contact with liquid water quickly before dosing onto sample. Experiment is designed in the way that there is no need of introducing inert gases into system. The samples are transported into and out of setup at UHV pressures to achieve clean experiment. With this new experimental setup the interaction of  $\alpha$ -Fe<sub>2</sub>O<sub>3</sub> surface with different exposures to water was investigated.

In present, the most important use (by volume) of iron oxides can be found in its industrial reduction to Fe and subsequent production of steel. Rocks containing high amounts of  $\alpha$ -Fe<sub>2</sub>O<sub>3</sub> and Fe<sub>3</sub>O<sub>4</sub> are reduced by carbo-thermal reduction ( $\text{Fe}_2\text{O}_3 + 3\text{CO} \rightarrow 2\text{Fe} + 3\text{CO}_2$ ) [4]. Although this process is known, it is very complicated surface mediated reaction. The initial reduction of bulk terminated (1×1) surface reconstruction of  $\alpha$ -Fe<sub>2</sub>O<sub>3</sub> to (2×1) can be achieved by annealing in ultra high vacuum and its real time study using Low Energy Electron Microscopy is one of the parts of this thesis.

The thesis is divided into six chapters. The first chapter provides a brief description on iron oxides with more attention given to  $\alpha$ -Fe<sub>2</sub>O<sub>3</sub> as the oxide, which was investigated. Second chapter describes experimental techniques used in the experiments providing information on general principle, construction design and data measurements. Third chapter describes unique design of liquid water dosing setup with explanation of all parts involved. Fourth chapter provides information on the testing of proposed setup with evaluation of elemental composition of tested surfaces and contaminations present during testing. Fifth chapter then provides information on water interaction with  $\alpha$ -Fe<sub>2</sub>O<sub>3</sub>(012) surface focusing on experimental techniques of X-ray Photoelectron Spectroscopy, Low Energy Electron Diffraction and Low Energy Ion Scattering. The last sixth chapter describes the (1×1)-to-(2×1) surface transition of  $\alpha$ -Fe<sub>2</sub>O<sub>3</sub>(012) using Low Energy Electron Microscopy.

# 1 IRON OXIDES

The iron oxides are based on close packed anion arrays of  $O^{2-}$ , with Fe cations occupying octahedral or tetrahedral interstices. As the anions are larger than cations ( $r_{O^{2-}} = 0.14$  nm,  $r_{Fe^{2+}} = 0.082$  nm and  $r_{Fe^{3+}} = 0.065$  nm), the arrangement of anions governs the crystal structure and topological interconversion between different oxides [11]. The most common arrangement of anion arrays in three dimensions is hexagonal close packing (hcp) with A-B-A-B periodicity stacking and cubic close packing (ccp) with A-B-C-A-B-C periodicity stacking. The basic structural unit in iron oxides is the  $Fe(O)_6$  octahedron or less commonly,  $Fe(O)_4$  tetrahedron.

Individual oxides differ in arrangement of cation interstices and stacking of arrays of anions. The FeO,  $Fe_3O_4$  and  $\alpha$ - $Fe_2O_3$  are the stable phases under thermodynamic equilibrium, which results in bulk crystal stoichiometries depending on temperature and  $O_2$  pressures [12]. According to phase diagram shown in Fig. 1.1, the  $\alpha$ - $Fe_2O_3$  is the most stable phase at 620 K and  $p_{O_2} = 10^{-22}$  mbar and extends to 1600 K at 1 bar.

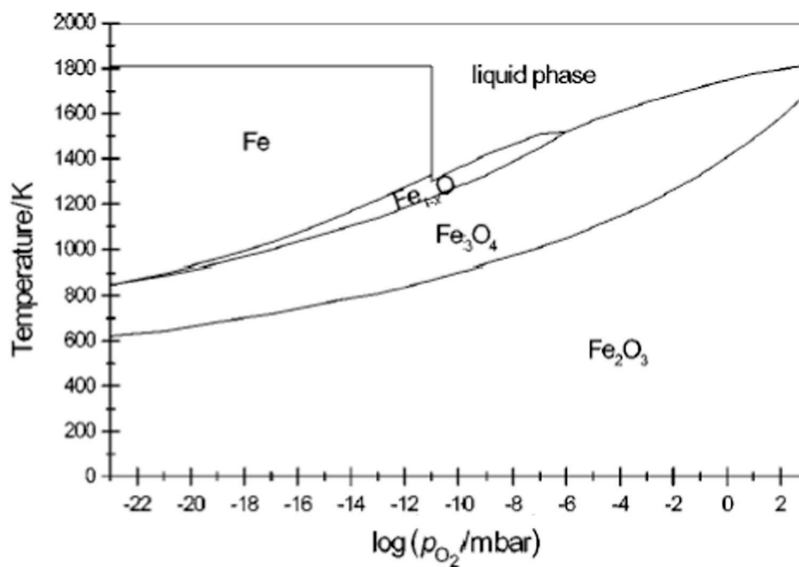


Fig. 1.1: Temperature-pressure phase diagram for iron-oxygen system. Picture reprinted from [13].

## 1.1 $Fe_{1-x}O$ (Wüstite)

This iron oxide is one of the most studied non-stoichiometric compound. It has received interest by mineralogists as a component in mineral systems, as end-member of a lower mantle phase, magneto-wüstite by geologists [14], or for its occurrence in ceramics and steel by material scientists.

### 1.1.1 Bulk Structure

$\text{Fe}_{1-x}\text{O}$  crystallizes in the cubic hex-octahedral structure (Fig.1.2) with  $\text{Fe}^{2+}$  cations in octahedral sites. It consists of a symmetrical unit cell with parameter  $a = 4.3 \text{ \AA}$ . In the  $[111]$  direction, the material is built from alternating planes of fcc O anions and Fe cations. In practice, this compound is always defective, with  $(1-x)$  values ranging from 0.83 to 0.95. The defects, so-called Koch–Cohen defects, are  $\text{Fe}^{3+}$  cations on tetrahedral sites linked to four  $\text{Fe}_{\text{oct}}$  vacancies, which merge into clusters of four  $\text{Fe}_{\text{tet}}$  interstitials linked to 13  $\text{Fe}_{\text{oct}}$  vacancies [15].  $\text{Fe}_{1-x}\text{O}$  is stable at temperature above 840 K in a reducing environment, but splits into Fe and  $\text{Fe}_3\text{O}_4$  when cooled slowly. Rapid quenching from 840 K can produce a metastable rhombohedral phase, but this process is still debated [16].

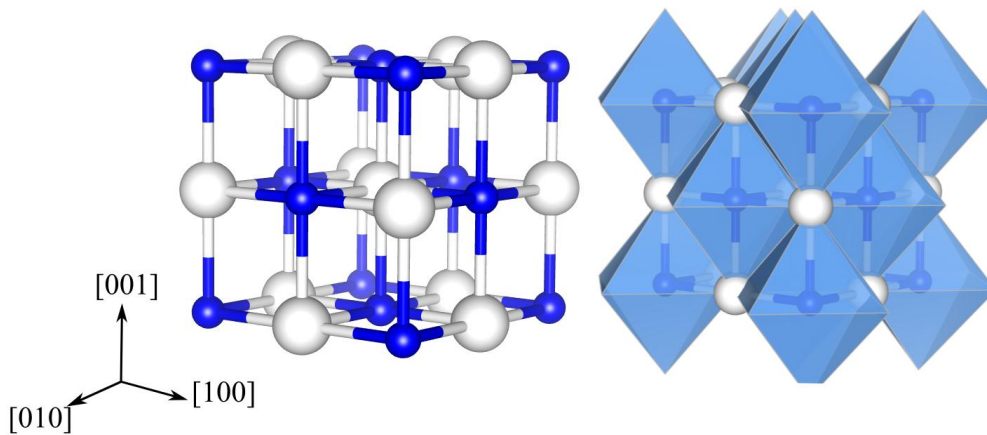


Fig. 1.2: Ball-and-stick and polyhedral models of wüstite ( $\text{O}^{2-}$  anions-white balls and  $\text{Fe}^{3+}$ -blue balls). The cubic rock salt structure with unit cell with parameter  $a = 4.3 \text{ \AA}$  is based on alternating planes of fcc O anions and Fe cations octahedrally coordinated to oxygen.

## 1.2 $\text{Fe}_3\text{O}_4$ (Magnetite)

The name of this oxide is derived from the district of Magnesia in Asia Minor, where large deposits of magnetite were discovered. In present time a great effort is put in to investigation of this material. Magnetite nanoparticles can be incorporated into systems for environmental contaminant removal [17] and cell separation [18], guided drug delivery [19], sealing components [20] and as contrast agents for magnetic resonance imaging (MRI) [21].

One of the most interesting areas of research of  $\text{Fe}_3\text{O}_4$  is in the field of Single Atom Catalysis (SAC) involving isolated metal atoms stabilized on appropriate substrates. There has been active search for miniaturization and improved stability since

catalytic dependence on size nanoclusters was reported [22]. Subsequently it was found out that these clusters doesn't play a role in catalysis at all and all catalytic activity was due to single atom species present on a surface [23].

Promising support for SAC shows (001) surface of  $\text{Fe}_3\text{O}_4$ . It has been reported that it provides stability for single atoms up to high coverages, preventing coalescence even at higher temperatures [24]. There has been several extensive studies ([25–27]) concerning this surface as base for SAC, using advantage of known surface structure and possibility of probing reaction on atomic scale using Scanning Tunneling Microscopy (STM).

### 1.2.1 Bulk Structure

$\text{Fe}_3\text{O}_4$  crystallizes (Fig.1.3) in inverse spinel structure [11]. The cubic unit cell includes eight formula units  $(\text{Fe}^{3+})_{\text{tet}}[\text{Fe}^{2+}\text{Fe}^{3+}]_{\text{oct}}\text{O}_4^{2-}$  and has a lattice constant of 8.396 Å.

The general formula for spinel crystals is  $\text{A}^2\text{B}_2\text{O}_4^{2-}$ , with A and B being Fe cations for iron oxides. The normal spinel structure is based on a close-packed array of anions. The A-site cations occupy 1/8 of the tetrahedral sites and the B-site cations occupy 1/2 of the octahedral sites. Inverse spinel structure is formed due to large crystal field stabilization energy [28]. Divalent cations can occupy 1/2 octahedral sites, displacing trivalent cations, which then occupy all the available tetrahedral sites creating the inverse spinel structure.

Thanks to  $\text{Fe}^{3+}$  and  $\text{Fe}^{2+}$  coexisting in octrahedral sites,  $\text{Fe}_3\text{O}_4$  exhibits relatively high conductivity ( $\approx 10^2 (\Omega \cdot \text{cm})^{-1}$ ) above 125 K. At this temperature the transition from monoclinic to inverse spinel structure takes place and is known as Verwey transition temperature. Bellow this temperature the electron hopping between  $\text{Fe}^{3+}$  and  $\text{Fe}^{2+}$  is limited and conductivity drops by two orders of magnitude [29].

$\text{Fe}_3\text{O}_4$  is ferrimagnetic<sup>1</sup> at room temperature. The intrinsic magnetization of  $\text{Fe}_3\text{O}_4$  can be explained by assuming the spins within individual sublattices to be ferromagnetically aligned but antiferromagnetically coupled between two sublattices. In addition, the magnitude of magnetic moments of two types of spins of  $\text{Fe}^{2+}$  and  $\text{Fe}^{3+}$  are not equal, which causes ferrimagnetism. The Curie temperature for  $\text{Fe}_3\text{O}_4$  is 858 K.

---

<sup>1</sup> Atoms in ferrimagnetic material exhibit opposing magnetic moments such as in antiferromagnetic material. However these moments are unequal giving raise to spontaneous magnetization

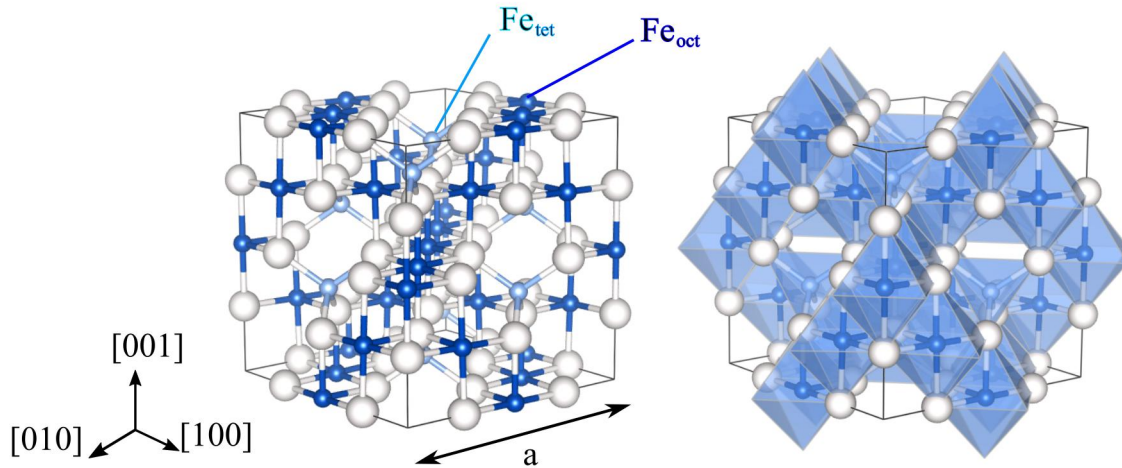


Fig. 1.3: Ball-and-stick and polyhedral models of magnetite ( $\text{O}^{2-}$  anions-white balls and  $\text{Fe}^{3+}$ -blue balls). The spinel structure is based on fcc lattice of  $\text{O}^{2-}$ . Cations occupy 1/8 of the tetrahedral sites and 1/2 of the octahedral sites. Cations in the tetrahedral sites are  $\text{Fe}^{3+}$ , the octahedral sites are filled with  $\text{Fe}^{2+}$  and  $\text{Fe}^{3+}$  with 50:50 ratio.

### 1.3 $\gamma\text{-Fe}_2\text{O}_3$ (Maghematite)

Maghematite, similar to hematite, is a fully oxidized iron oxide polymorph. Research of this iron oxide was focused mainly on synthesis of its nanoparticles with goal of removing heavy metals from contaminated water [30] and biomagnetic precursors [31].

#### 1.3.1 Bulk Structure

$\gamma\text{-Fe}_2\text{O}_3$  is iso-structural with  $\text{Fe}_3\text{O}_4$  and is often formed by its oxidation. There are only  $\text{Fe}^{3+}$  cations present in the spinel structure and thus Fe vacancies are required to ensure the charge neutrality. These ordered vacancies represent the lowest energy configuration and are responsible for band gap of  $E_g = 2.07$  eV [32]. The size of band gap is different for different spin polarizations, which makes this material interesting candidate for spin filters in spinotronic devices.

The lattice parameter of  $0.83474$  Å is slightly smaller than that of  $\text{Fe}_3\text{O}_4$  ( $0.8396$  Å), and this compound is also ferrimagnetic with Currie temperature of  $\approx 950$  K.

### 1.4 $\alpha\text{-Fe}_2\text{O}_3$ (Hematite)

Hematite is the most thermodynamically stable phase of iron oxides with n-type semiconducting properties under ambient conditions [33]. For its abundance in Earth's

crust it has received attention for its role in processes as dissolution [34] or organic transport [35]. It has also been extensively investigated for technical applications as catalysts [36], pigments [37], gas sensors [38], optical devices [39], and electromagnetic devices [33] owing to its non-toxicity, low processing cost, and high resistance to corrosion.

In recent years much of the interest in  $\alpha\text{-Fe}_2\text{O}_3$  has been focused on using it as a photoanode material for photoelectrochemical cells. These cells offer the ability to convert solar energy to chemical through splitting of water into molecular oxygen and hydrogen. Photoelectrochemical cells use photoexcitation of electron–hole pairs in semiconductors to supply a net current to split water. The ideal semiconductor for such process has a bandgap that can take advantage of most of the standard AM 1.5 solar spectrum ( $\sim 1\text{--}2\text{ eV}$ ).  $\alpha\text{-Fe}_2\text{O}_3$  has risen as a strong candidate in the photoassisted water oxidation reaction due to its stability in aqueous environment, low cost, easy synthesis, and the band gap ( $\sim 2\text{ eV}$  [40,41]) that allows the absorption of visible light. In theory,  $\alpha\text{-Fe}_2\text{O}_3$  can achieve maximal solar-to hydrogen efficiency of 15% [42]. However, in reality its performance as a water-oxidizing photoanode has been limited by a very short electron–hole pair lifetime ( $\sim 1\text{ ps}$ ), low hole diffusion length (2–4 nm), poor electron mobility (in the order of  $10^{-2}\cdot\text{cm}^2\cdot\text{V}^{-1}\cdot\text{s}^{-1}$  at room temperature), and stagnant oxygen evolution reaction [42].

Various strategies have been developed to overcome limitations of  $\alpha\text{-Fe}_2\text{O}_3$  photoanodes. Oxygen vacancy engineering, doping, nanophotonic structures, plasmonic structures are tested to improve efficiency. The charge transfer, limited by low hole diffusion length, can be significantly enhanced by changes in morphological structure, i.e. array of nanowires, nanotubes, dendrites, nanosheets etc. Lowering the high overpotential needed for the oxygen evolution reaction at the photoanode surface remains a great challenge, which has been addressed by introducing co-catalysts, surface passivation layers or surface chemical corrosion.

### 1.4.1 Bulk Structure

$\alpha\text{-Fe}_2\text{O}_3$  crystallizes in corundum structure. It can be described in hexagonal system, with lattice parameters  $a = 0.5034\text{ nm}$  and  $c = 1.375\text{ nm}$  (six formula units per unit cell). Along the  $c$  direction, this structure can be viewed as a hexagonal close packed (hcp) stacking of  $\text{O}^{2-}$  anions, in such fashion that iron cations  $\text{Fe}^{3+}$  occupy two thirds of the octahedral interstices [15]. Cations in the octahedral sites which share faces are repelled along the direction normal to [001], causing the cations to shift closer to the unshared faces and thus causing the distortion from ideal packing of the cation sub-lattice [42].

$\alpha\text{-Fe}_2\text{O}_3$  shows interesting magnetic characteristics. At temperatures lower than

260 K (known as Morin temperature), it exhibits antiferromagnetic behavior. Above this temperature, the reorientation of spins takes place causing the destabilization of their anti parallel ordering. This leads to a weak spontaneous magnetization of  $\alpha\text{-Fe}_2\text{O}_3$ , which becomes weakly ferromagnetic [43]. The Néel temperature, at which antiferromagnetic material becomes paramagnetic, due to thermal energy becoming large enough to destroy the microscopic magnetic ordering, is for  $\alpha\text{-Fe}_2\text{O}_3$  frequently reported to be at 950 K.

Electrical properties of  $\alpha\text{-Fe}_2\text{O}_3$  have been studied since 1930s. It has been reported that compared to other n-type semiconductors such as  $\text{TiO}_2$ ,  $\text{WO}_3$  and  $\text{BiVO}_4$ ,  $\alpha\text{-Fe}_2\text{O}_3$  has very low electrical conductivity ( $10^{-14} \Omega^{-1}\text{cm}^{-1}$ ) [44], which is highly anisotropic. It means that conductivity along [001] direction is four times lower than conductivity along basal plane [45]. This phenomenon can be explained by considering magnetic ordering of the crystal. Spins of Fe cations are coupled antiferromagnetically along [001] direction and ferromagnetically in (001) basal plane. That's why electrons would be allowed to move from one Fe atom to another in basal plane and would be forbidden to move along the direction [001] [46].

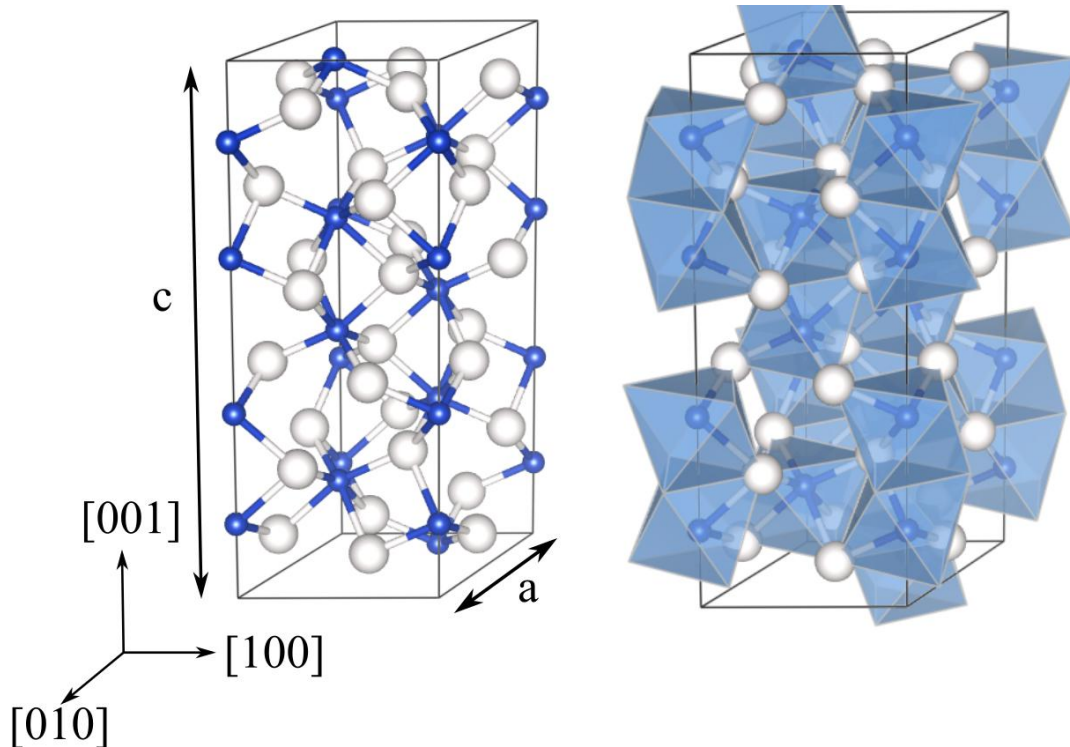


Fig. 1.4: Ball-and-stick and polyhedral models of hematite unit cell with  $\text{O}^{2-}$  anions represented by white balls and  $\text{Fe}^{3+}$  with blue balls. This structure can be viewed as a hexagonal close packed (hcp) stacking of  $\text{O}^{2-}$  anions with slight distortion caused by octahedral sites being repelled along the direction normal to [001].

### 1.4.2 $\alpha$ -Fe<sub>2</sub>O<sub>3</sub> (012) "R-cut" Surface

Commonly known as  $\alpha$ -Fe<sub>2</sub>O<sub>3</sub> ( $1\bar{1}02$ ), (012) surface haven't received much attention. Studies of this non-polar surface on single crystals were done on several occasions. There are two stable surface reconstructions that can be formed in ultra high vacuum reported in experiments namely ( $1\times 1$ ) and ( $2\times 1$ ) in works of Henderson [9] Gautier-Soyer [47] and Lad [48].

The ( $1\times 1$ ) structure is the most stable surface reconstruction of  $\alpha$ -Fe<sub>2</sub>O<sub>3</sub> in ambient conditions can be formed by oxidation in UHV (see Fig.1.5). This surface is thought to be stoichiometric and bulk-terminated. Unit cell is roughly square, and contains an equal number of under-coordinated Fe cation and O anion sites. Cation sites are Fe<sup>3+</sup> with core level energies identical to the bulk atoms. The O<sup>2-</sup> sites form zig-zag rows, with iron cation sites on each side of oxygen rows.

The ( $2\times 1$ ) structure results from vacuum reduction of the surface in UHV, but its atomic structure isn't completely known. It was suggested that the reconstruction is restricted to the surface layer with every second oxygen row either partially [49] or completely [9] missing (Fig.1.5). This surface reconstruction adsorbs oxygen, both molecular and dissociated, which stabilizes some hydroxyls on the surface and destabilizes molecularly adsorbed water [50]. Recently, Kraushofer et. al. [51] proposed „alternating-trench“ model for this surface using scanning probe measurements and density functional theory to support his model. Calculations show that this model is the most energetically favorable surface over wide range of chemical potentials. It is based on vacancy model with two rows of oxygen atoms removed, creating alternating narrow and wide trenches, based on distance of the top-layer oxygen rows. Cation sites are occupied by Fe<sup>2+</sup>.

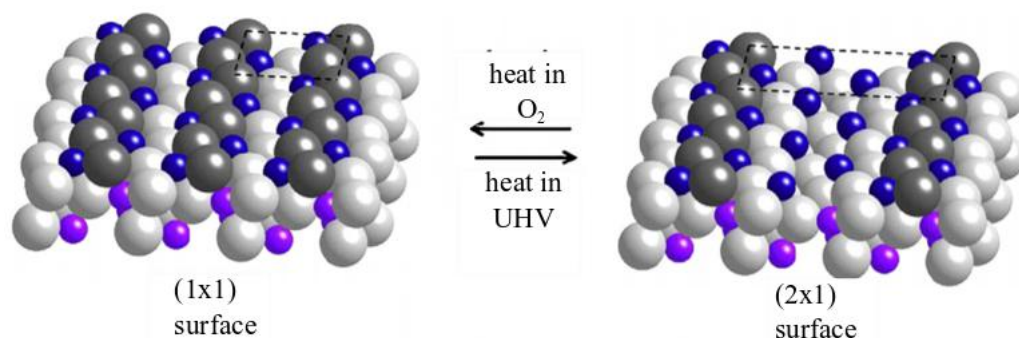


Fig. 1.5: Surface reconstructions of hematite (012). The ( $1\times 1$ ) surface is bulk terminated, it features oxygen (gray) rows (highlighted by dark gray) straddled by iron (blue). The surface structure of the ( $2\times 1$ ) is still debated. Picture reprinted from [49].



## 2 EXPERIMENTAL TECHNIQUES

This chapter provides brief insight into experimental methods used in this project. The main focus is laid on Low Energy Electron Diffraction, Low Energy Electron Microscopy and X-ray Photoelectron Spectroscopy as the main techniques used for analysis. The additional techniques used in this project include Low Energy Ion Scattering and Scanning Tunneling Microscopy are briefly mentioned.

### 2.1 Low Energy Electron Diffraction (LEED)

The standard technique in surface science for obtaining structural information about surfaces is elastic scattering of the electrons. In almost every surface-physics laboratory Low-Energy Electron Diffraction (LEED) is used to check the crystallographic quality of either a clean surface, or in ordered adsorbate overlayers. In the experiment a beam of electrons with a primary energy between 50 and 300 eV is incident on the surface and the elastically backscattered electrons create the diffraction pattern that is imaged on a phosphorous screen.

#### 2.1.1 General Principle

As stated by de Broglie theorem that all matter can exhibit wave-like behavior, electrons can be assigned wavelength described with equation (2.1):

$$\lambda = \frac{h}{\sqrt{2mE}}, \quad (2.1)$$

where  $h$  stands for Planck's constant,  $m$  stands for mass and  $E$  for kinetic energy of electrons. Waves impinging on the ordered surface are scattered and reflected interfering with each other giving rise to diffraction pattern. This pattern portray lattice in reciprocal space as a Fourier transform image of the real 2D surface ordered structure. It can be described by reciprocal lattice vector  $\vec{G}$ , which is linear combination of translational vectors  $\vec{g}_1$  and  $\vec{g}_2$  described by equation (2.2):

$$\vec{G} = h\vec{g}_1 + k\vec{g}_2, \quad (2.2)$$

where  $h$  and  $k$  are arbitrary integers. The relation between unit vectors of real and reciprocal lattice can be written as:

$$\vec{g}_1 = 2\pi \frac{\vec{a}_1 \times \vec{n}}{|\vec{a}_1 \times \vec{a}_2|}, \quad \vec{g}_2 = 2\pi \frac{|\vec{a}_2 \times \vec{n}|}{|\vec{a}_1 \times \vec{a}_2|}, \quad (2.3)$$

where  $\vec{a}_1$  and  $\vec{a}_2$  represent unit vectors of real lattice and  $\vec{n}$  is vector normal to the surface. To create constructive interference and thus bright spot in diffraction pattern, electrons must fulfill Laue condition, which states:

$$\vec{G}_{\parallel} = \vec{K}_{\parallel} = \vec{k}_i - \vec{k}_f, \quad (2.4)$$

where  $\vec{k}_i$  is wave vector of incident electron,  $\vec{k}_f$  is wave vector of scattered electron and  $\vec{G}_{\parallel}$  is reciprocal lattice vector as given in (2.2). Laue condition can be visualized by constructing the Ewald sphere (Fig. 2.1). In X-ray diffraction, waves can be diffracted from all layers of the crystalline sample. In reciprocal space this means that constructive interference can occur only when Ewald sphere intersects with discrete points defined by reciprocal values of interatomic distances in crystalline lattice. In ideal case (Fig. 2.1(a)), distance between discrete points in vertical axis in reciprocal space would go to zero as the electrons would diffract only on the top layer and thus distance between top two atomic layers would be virtually infinite. Change of size of the Ewald sphere induced by the change of energy of incident electrons would result in pattern with constant intensity of diffraction spots. In reality the electron beam can be diffracted also on the few layers below the surface. In Ewald construction (Fig. 2.1(b)), this results in rods with „thicker“ and „thinner“ regions. Considering this, the intensity of specific spots in diffraction pattern can be different for different energy of incident electrons. This phenomenon as well as multiple scattering events are taken into consideration when analyzing *LEED I-V* curves. In this measurement, the intensity of each diffraction spot at wide range of energies is measured and the set of intensity spectra is fitted by a model curve calculated for a specific proposed model with aim to achieve certain degree of the agreement.

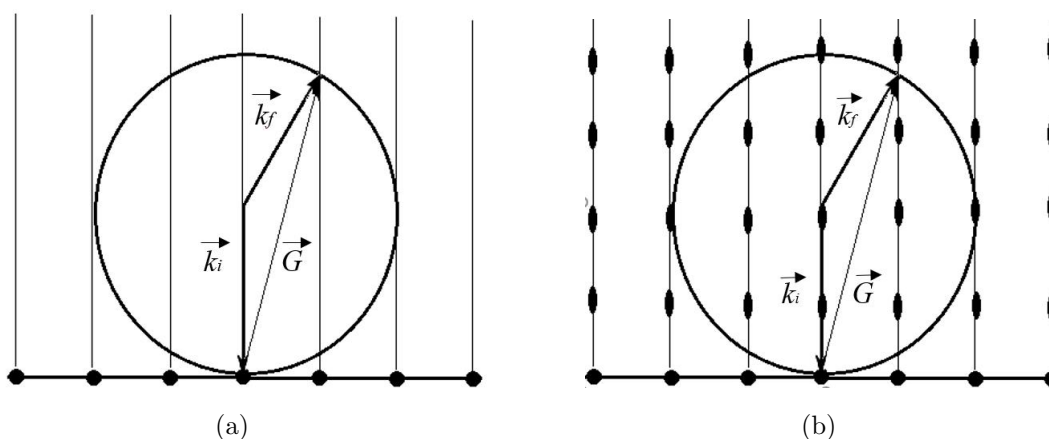


Fig. 2.1: Construction of the Ewald sphere. (a) Ewald's construction for perfect 2D surface lattice. (b) Ewald's construction of quasi-2D surface lattice

## 2.1.2 Construction Design

The configuration of LEED can be seen in Fig. 2.2. The electrons are emitted by thermo-emission from Tungsten filament. Set of electrostatic lenses collimates and focus electron beam onto the sample. The reflected electrons pass through a several concentric grids, that filter out inelastically scattered electrons and accelerate the elastically scattered ones to the concentric fluorescent screen. The diffraction pattern is acquired by the CCD camera.

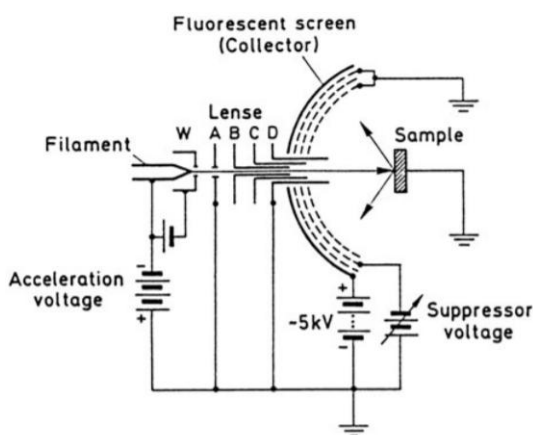


Fig. 2.2: Schematic view of the LEED instrumentation. Picture reprinted from [52].

## 2.1.3 Interpretation of the Diffraction Pattern

Simple inspection of a LEED pattern and measurement of the geometrical spot positions can carry a lot of useful information about a surface. The information obtained

about the surface always originates from an area with a diameter smaller than the coherence width of the electron beam ( $\approx 10$  nm). The LEED pattern must exhibit sharp spots with high contrast and low background intensity for good crystallographic quality of the surface. Random defects or crystallographic imperfections will broaden the spots and increase the background intensity due to scattering from these statistically distributed centers [52].

Other surface features, that can be identified using LEED are regular atomic step edges and facets. First one results in spot splitting at certain beam energies. Faceted surface creates a set of diffraction spots, that is centered around different point than the original LEED pattern. This can be noticed in LEED pattern if a continuous change of energy during measurement is realized. With higher energies spots are moving closer towards the central spot. In faceted surface these spots will be moving in two different directions as there are two central spots.

## 2.2 Low Energy Electron Microscopy (LEEM)

Low-energy electron microscopy is an imaging method that uses elastically backscattered electrons with energies in range of 0 – 50 eV. This technique was proposed and developed by Ernst Bauer over a multi-decade period of time [53, 54]. LEEM as technique stands out for exceptional surface sensitivity, real-time imaging capability, and utilize a different contrast mechanisms that take advantage of the wave nature of the electrons. This technique employs an ultrahigh vacuum conditions and in situ surface modification processes (eg. deposition, gas dosing) can be performed during imaging. These properties then allow to study of structure, morphology and dynamic processes with excellent spatial and temporal resolution.

### 2.2.1 General Principle

Low Energy Electron Microscope uses highly collimated electron beam to illuminate sample. This beam (10 – 20 keV) is decelerated by objective lens optics to orders of several eV and impinges on a surface. Images are formed with low-energy electrons that are reflected from solid surfaces without energy loss, that is the so-called elastically backscattered electrons. This technique is based on diffraction imaging, that is intimately related to the LEED technique described in section 2.1. The typical LEEM imaging electron energy is in the range 0–50 eV, which covers low energy interval of typical LEED experiment. Electron scattering in this energy range is surface sensitive resulting from short inelastic electron mean free path in solids. The reflectivity of very low-energy electrons is also very high compared to electrons with higher incident energies. This is result of several factors such as forward scattering

effects, the exponential dependence of the Debye–Waller factor of the intensity on the magnitude of momentum transfer and sharing of elastically scattered electrons among an increasing number of allowed diffraction conditions at higher energy [55].

### 2.2.2 Construction Design

LEEM is an ultra-high vacuum instrument, with typical base pressure of  $1 \times 10^{-10}$  mbar and operational pressure under experimental conditions of up to  $10^{-6}$  mbar. The pressure limitation during experimental operation is imposed by high voltage isolation between the sample and objective lens.

Design of an uncorrected LEEM instrument is shown in Fig. 2.3. It shows the commercially available FE-LEEM P90 from SPECS GmbH (Berlin) available at CEITEC facility. A cold field emission gun emits an electron beam at 15 keV electron energy and 25 meV energy width [56]. Beam goes through magnetic gun lens followed by a condenser lens, which vary the illumination of system and focuses the electron beam into the entrance plane of a square magnetic prism. Magnetic prism then deflects the beam by  $90^\circ$  and focuses it into exit plane located near the transfer lens. Beam is again refocused into objective lens of the instrument. In the objective lens the electrons are decelerated and impinge on the sample. Backscattered electrons are then accelerated through the same objective lens system and deflected by magnetic prism to another transfer lens system and to the CCD detector.

This system is also equipped with different contrast and diffraction apertures that can be positioned in non-specular diffraction spot in LEED pattern by tilting the beam and thus performed dark field measurements or in real space image to specific areas of the sample to measure local diffraction pattern also known as micro-diffraction.

To further improve resolution of the microscope the aberration corrector can be implemented. It was shown [57] that third order spherical aberration of objective lens can be corrected by reflecting them from electron mirror in such fashion that electrons are slowed down, reflected on equipotent surface and again accelerated to previous energies. Another design presented in work of prof. Rose [58] employing four electrodes enables independent adjustment of the focal length  $f$ , as well as chromatic and third order spherical aberration

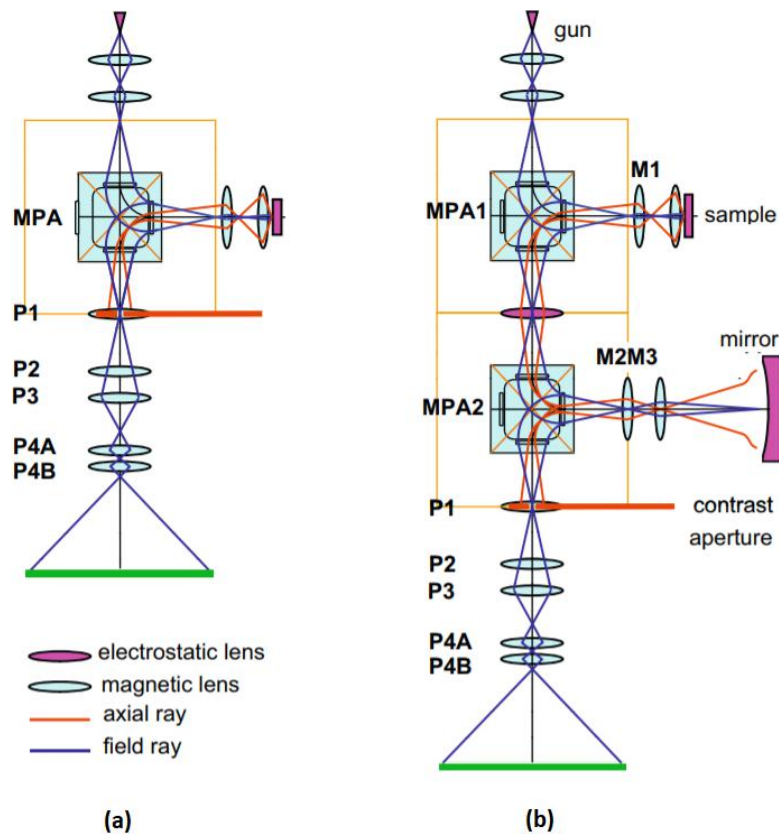


Fig. 2.3: Illustration of the schematic assembly of the uncorrected LEEM instrument (a), and assembly with aberration corrector (b). MPA - Magnetic prism array, P1 - transfer lens for real space image, P2 - transfer lens for LEED pattern, P3, P4A/B - projector lens system. Picture reprinted from [56].

### 2.2.3 Imaging Modes

Compared to other microscopic techniques using electrons as probes (SEM, TEM), spatial resolution of LEEM is limited to range of 2-20 nm. The capability of real-time image acquisition originates from the high signal-to-noise ratio of reflected low-energy electrons. This, with combination of parallel illumination/detection is favorable for fast imaging acquisition. Besides the spatial resolution, contrast is generally the most important aspect of an imaging technique that defines its range of application and usefulness. The image contrast is a direct consequence of the interaction of electron waves, arising from the local variation in diffraction conditions in *amplitude contrast* or from the interference between electrons with different optical paths in *phase contrasts*.

### **Bright-Field/Dark-Field**

Image in the microscope is formed by selecting particular diffraction spot using contrast aperture located in back focal plane of objective lens. The normal exit geometry of (0,0) diffraction spot represent electrons that have not undergone any momentum transfer parallel to the surface and is often referred to as a bright-field. Different amplitude and phase contrast mechanisms are visible in the this imaging mode.

Dark-field mode uses low-order integer diffraction spots to form images. Electrons that undergo diffraction with non-zero parallel momentum transfer along these non-specular spots are reflected from the sample at trajectories that are not normal to the surface. This causes distortion of the image due to spherical aberration of objective lens. To compensate this distortion, in practice the use of beam tilt by specific angle that places the non-specular imaging beam along a trajectory normal to the surface is used. Regions on the surface for which the diffraction condition is fulfilled will appear bright in the image, whereas other regions will appear dark in the image. This is used to distinguish regions with different structures or differently rotated domains.

### **Mirror Electron Microscopy**

In this technique high-velocity electrons are decelerated in the electrostatic mirror field and are turned back just before reaching the negatively charged surface [59]. The reflection in the MEM mode is very sensitive to the electromagnetic field variations that result from the surface topography, electrostatic potential, magnetic field, surface charges and work function, and so on [55].

### **Low Energy Electron Diffraction**

A LEEM instrument also allows observing LEED patterns by imaging the back focal plane of the objective lens. The area from which the information is gathered can be restricted by inserting an aperture in the image plane in the input side of the beam separator, thus revealing surface structure at length scales much shorter than in a conventional LEED, this is so called  $\mu$ -LEED.

This technique is also excellent tool for measurement of *LEED-IV* curves. As the diffracted electrons are deflected during their acceleration away from the surface in a way that exactly cancels the change in initial emission angle with energy, the position of the diffraction spots doesn't change with variation of energy of incoming electron beam [60]. This eliminates the need of complex tracking algorithm of diffracted beams with energy while measuring their intensity.

## 2.3 X-ray Photoelectron Spectroscopy (XPS)

X-ray photoelectron spectroscopy (XPS) is one of the most common techniques used in surface science. It provides quantitative analysis of chemical composition and state of studied samples. Although considered as a surface sensitive technique, the XPS can also be used to determine the thickness of thin film by employing angle resolved measurements.

### 2.3.1 General Principle

This technique is based on photoelectric effect. Electron leaves the sample when atom absorbs photon with energy higher than is binding energy of electron and work function of the sample. Kinetic energy of photoelectron is then determined as difference these energies and is shown in equation (2.5)

$$E_{kin} = E_{photon} - (E_B + \Phi_{spec}), \quad (2.5)$$

where  $E_B$  is binding energy of electron and  $\Phi_{spec}$  is work function of spectrometer. The process of generating photoelectrons described in previous equation can be explained by figure 2.4.

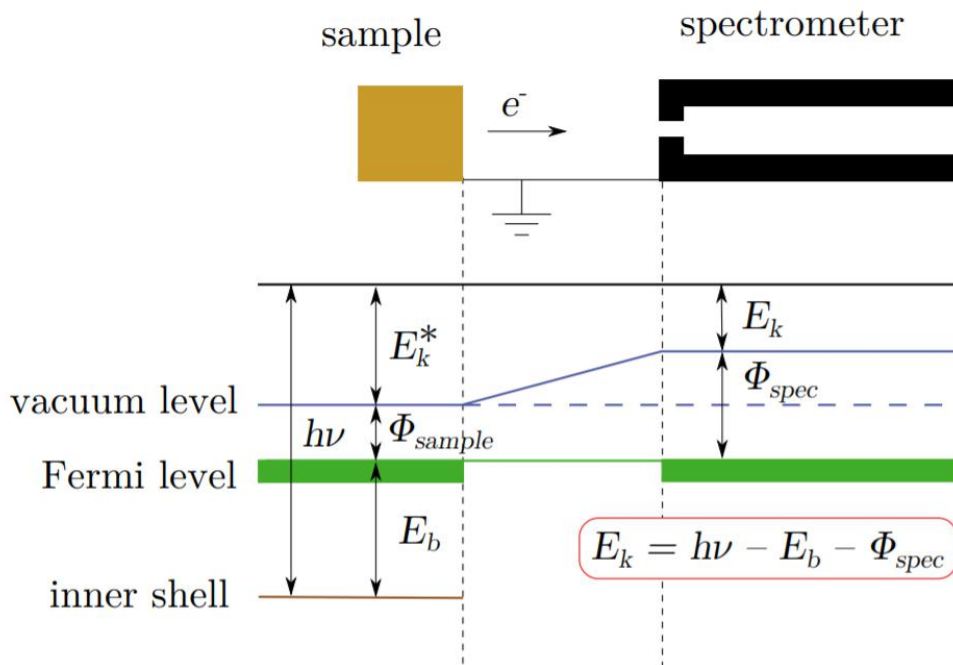


Fig. 2.4: Illustration of the general principle of XPS technique. Picture reprinted from [61]

### 2.3.2 Construction Design

In order to excite electrons from inner shells of the sample, high energy radiation must be absorbed. For this purpose, soft X-ray or synchrotron radiation is used in this technique. Source of such radiation (Fig. 2.5) must satisfy various design and material requirements to achieve best resolution and energy spectrum width. The best materials for anode design appeared to be Aluminium and Magnesium. With characteristic X-ray energy of  $E_{\text{Al}}=1486.6\text{ eV}$  and  $E_{\text{Mg}}=1256.6\text{ eV}$ , they provide wide enough spectrum to detect all elements of periodic table. Moreover, full width at half maximum of characteristic lines are small enough to provide good resolution for detection of fine peak splitting and shifts.

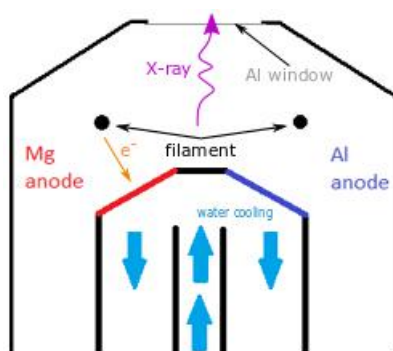


Fig. 2.5: Schematic view of the X-ray source used in XPS. The voltage of 15 kV is applied between filament and the selected anode. Al window limits transmissivity of secondary electrons produced by bombardment of the anode.

Analysis with this technique is based on measuring kinetic energies of photoelectrons. These electrons of a specific kinetic energy are measured by setting voltages for the lens system that both focus them onto the entrance slit and retards their velocity so that their kinetic energy matches the pass energy of the analyzer. This lens system can be operated in two modes. In *high magnification* mode are electrons collected with high angular acceptance which results in measuring smaller areas of the sample. Second mode is *low magnification* mode. In this mode the angular acceptance is much lower resulting in larger areas of the sample being measured.

Hemispherical analyzer (Fig. 2.6) is most common type used for XPS. It consists of two concentric hemispheres which are kept at negative potentials in such way that potential in absolute value on outer hemisphere is greater than on inner hemisphere. Trajectory of electrons in analyzer are then circular with radius equal to arithmetic average of radius of the hemispheres. Analyzer can be operated in two modes, namely, Fixed Analyzer Transmission (FAT), also known as Constant Analyzer Energy (CAE), or Fix Retard Ratio (FRR) also known as Constant Retard Ratio (CRR).

In FAT, the pass energy of analyzer is kept constant and the velocity of electrons are only influenced by transfer lens system. The most measurements of XPS spectra is done in this mode as it provides good resolution over broad spectrum of energies. In FRR, the ratio of analyzer pass energy and initial electron kinetic energy is constant. This results in increased resolution in high kinetic energy part of spectra and thus enhance intensity of weak peaks while restricting intense background.

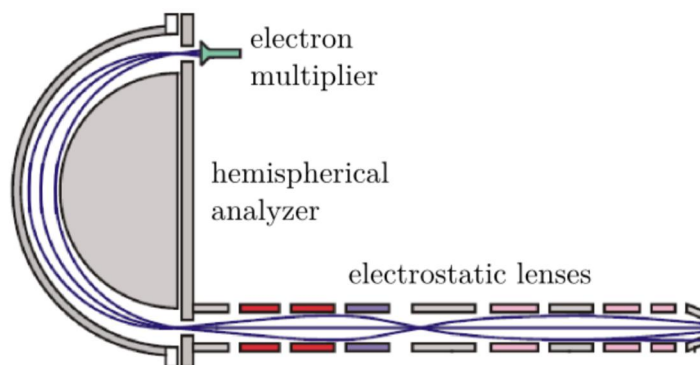


Fig. 2.6: Schematic view of the electron optics and analyzer used in XPS. Picture reprinted from [61]

### 2.3.3 Interpretation of the XPS Spectrum

The XPS spectra can be labeled both by kinetic and binding energy, both with its advantages. While in binding energy labeling, photoelectron peaks keep their position while using another anode, in kinetic energy labeling Auger peaks stay the same.

There are several processes that can be seen in XPS spectra and the most common are described in following text.

#### Photoelectron Peaks

Every element has a specific set of photoelectron peaks and by their energy, photoelectrons can be assigned to electrons in specific orbitals. The electronic structure of an atom changes, when it is bound in a compound, therefore the photoelectron peaks shift for atoms to lower or higher binding energies. In all orbitals apart from s, the spin-orbital splitting takes place and there are two peaks for every orbital.

#### Auger Electron Peaks

These peaks in XPS spectrum arise from phenomena called Auger effect. In this process (Fig. 2.7) a electron is emitted from core energy level shell, leaving vacancy

behind. To minimize the energy of the system, electron from higher level falls into vacancy resulting in release of energy. This energy is then emitted as photon or is transferred nonradiatively to electron in higher energy shell which is then emitted. This electron is called Auger electron.

Since the Auger effect is an intrinsic process, the kinetic energy of a specific Auger electron is always the same, meaning in the binding energy spectrum its position changes with different anode. As some Auger peaks may overlap with photoelectron peaks, it is advantageous to use both anodes for measurement to better understand chemical composition of the sample.

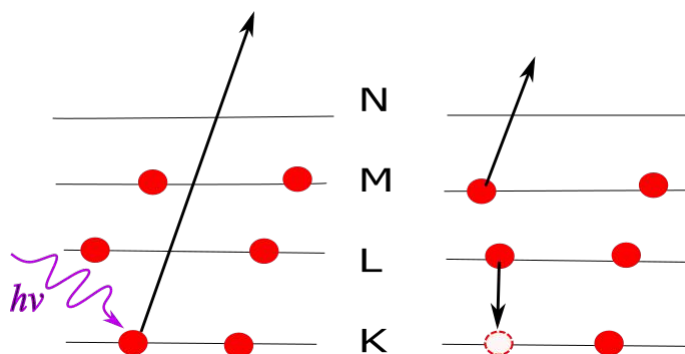


Fig. 2.7: Process of generation of Auger electron in XPS

### Satellite Peaks

The x-ray source in principle does not produce monochromatic radiation. Although the intensity of  $K_{\alpha}$  line is the greatest, there are other lines present, which results in multiple peaks with constant offset. Because the intensity of the satellite peaks is much lower than that of the original peaks, usually they are only distinguishable next to peaks with high intensity.

### Plasmon and „Shake-up“ Peaks

For an ion there is finite probability of staying in excited energy state. Photoelectron emitted from such ion exhibits lower kinetic energy, which is seen in spectrum as „shake-up“ peak at higher binding energy. These peaks are common for paramagnetic state of an atom. The classic example being Cu  $2p_{3/2}$  in CuO and Cu(OH)<sub>2</sub>.

Plasmon peaks involve loss of a set amount of energy due to the interaction between the photoelectron and other electrons. Plasmon peaks occurs for example near the Al 2s region in aluminum metal spectrum.

## 2.4 Additional Experimental Techniques

### 2.4.1 Low Energy Ion Scattering (LEIS)

Low Energy Ion Scattering also known as Ion Scattering Spectroscopy (ISS) is one of the several methods used for analysing surface structures. This method uses ions of noble gases (He, Ar, Ne) with low energies (0.1 to 10 keV), which are scattered elastically from surfaces. Ions scattered from deeper layers have higher probability of neutralization and thus the primary signal come from scattering on the surface. Thanks to neutralization, the LEIS excels in exceptional surface sensitivity. Depth resolution reaches up to 10 Å [67].

Different types of events may take place as a result of the ion beam impinging on a surface. These events include electron or photon emission, electron transfer, scattering, adsorption, and sputtering. As the name suggests, LEIS is primarily concerned with scattering phenomena.

As the energies of the impinging ions in this technique are far greater than energies of thermal vibrations, phonon oscillations, and interatomic binding, these effects can be ignored and the interaction of particle and surface may be thought of as a binary elastic collision shown in Fig.2.8,

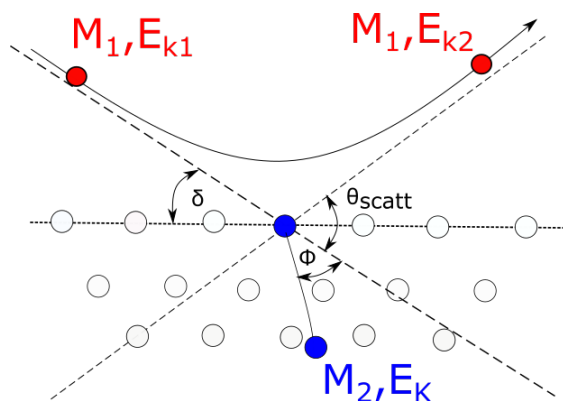


Fig. 2.8: Schematic view of the binary collision of the impinging ion of noble gas onto sample surface.

where the mass of impinging ion projectiles is  $M_1$ , and its kinetic energy  $E_{k1}$ .  $M_2$  is the mass of scattering center in stationary state with kinetic energy equal to zero. After the collision the projectile retains its mass, but scattering event changes its kinetic energy to  $E_{k2}$  and gives energy  $E_K$  to target atom.

To take quantitative approach to this method, one has to take into consideration effects like repulsive influence of atomic cores, multiple scattering events, shadowing and interaction potentials are not discussed in this text and reader is referred to literature like [52] and [68].

Noble gases are usually used for the primary ions in LEIS as they avoid contamination of the surface that would occur with more reactive material being used. Often used helium provides the widest mass range detection, with only hydrogen being not detectable. Other elements used as ion probes are argon, neon.

For ion source a simple sputter gun design can be used. The gas is introduced into gun volume and thus also into vacuum system by leak valve and is to desired pressure. To ionize the gas the thermal emission tungsten cathode is often used. Ions are extracted by extractor electrode and focused by objective lens onto sample. For scanning of the sample surface, deflector plates can be implemented inside the ion source.

Scattered ions are detected by using an energy analyzer either of the sector cylindrical mirror or hemispherical type as mentioned in section 2.3.2 and an electron multiplier detector. For most instruments, the scattering angle ( $\Theta_{scatt}$ ) is fixed, but in custom-made spectrometers it may be varied. For detecting neutrals often Time of Flight (ToF) analyzer is used. This mass analyzer is a system in which a packet of ions in the source is accelerated by a high potential into a field free flight tube. Lighter ions move with higher velocities, and thus arrive at the detector sooner than do the slower-moving heavier ions. Typical flight times range from 10 ns up to 800  $\mu$ s [68].

### 2.4.2 Scanning Tunneling Microscopy (STM)

This Nobel prize awarded technique was introduced by Binnig and Rohrer in 1982 [70]. By taking advantage of the quantum-mechanical tunneling effect, the STM operation principle is based on moving a sharp tip in the vicinity of a surface. The gathered information is the convolution of the topography and electronic structure of the sample. The ability of precise local probing gives STM a major advantage over other surface sensitive techniques that provide averaged information over a certain surface area. However, it is advantageous to use this technique in conjunction with diffraction techniques such as LEED and spectroscopic techniques such as XPS to obtain full crystallographic and chemical information.

Basic principle of STM lays in quantum tunneling effect through potential barrier. In regions before and after potential barrier the energy  $V(x)$  making wave vector a real number and thus wave function is propagating as a normal wave. In region, where  $V(x) > 0$ , the tunneling coefficient is an imaginary number causing exponential decrease of probability density of wave function. If the width of the barrier is less than extinction length of the  $\psi(x)$ , the wave can tunnel through the barrier and propagate on the other side. This process is schematically shown in Fig.2.9.

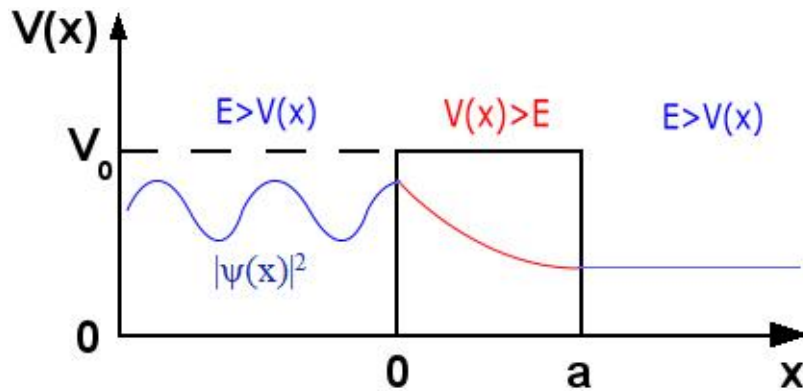


Fig. 2.9: Schematic illustration of the tunneling process of the electron through the potential barrier. Wave function propagates in the first region as wave until it hits barrier. Inside the barrier the wave function exponentially decays through it. In region behind barrier wave with much lower amplitude.

In real situation the wave function for tunneling electron and shape of the barrier might be more complicated, but basic principle described above with vacuum between sample and the tip acting as barrier still applies. Traditional theoretical STM simulation methods are based on either a nonperturbative approach [71] or a perturbative approach [72] to achieve best agreement of the model to experimental results.

STM instrumentation is simple, yet it encompasses different technological branches that have little in common with each other. These areas include tunneling experiments, surface science and microscopy. For proper technological implementation, knowledge of different disciplines such as mechanical, electrical and control engineering is needed [73].

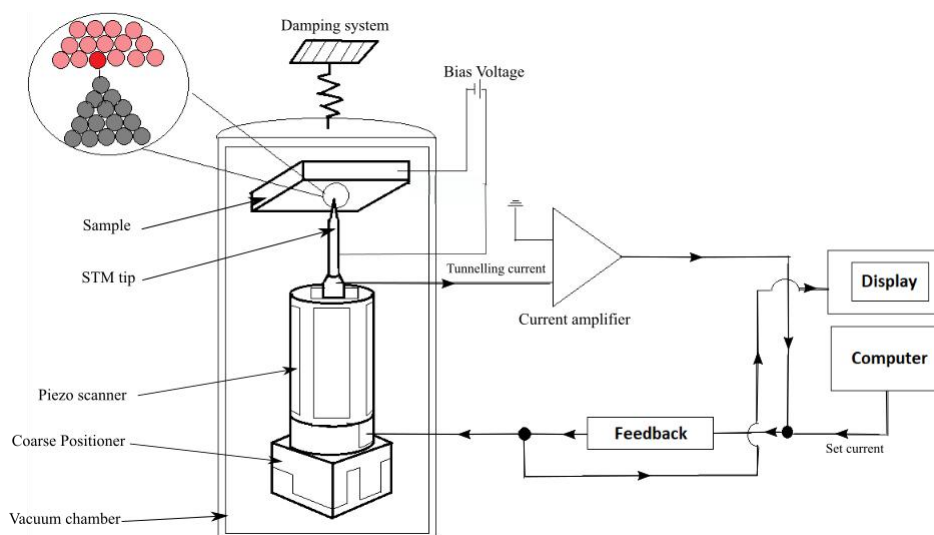


Fig. 2.10: Scheme of the instrumentation of the STM microscope. The microscope head is located in the vacuum chamber, which is insulated from outside vibrations. The tunneling current is amplified and the feedback loop adjusts the tip-sample distance to obtain a set value for current intensity. The feedback loop signal is imaged on the display as a convolution of the topography and electronic structure of the surface of the sample.

On the Fig. 2.10 the schematic view of the STM setup is shown. A STM microscope setup consists of a microscope head where a sample, tip and positioning system is located, a chamber providing the required environment varying from UHV for surface science experiments to liquid electrolyte for electro-chemistry, a damping system, electronics and in case of low temperature STM the liquid nitrogen or liquid helium cooled cryostat. Basic requirement for the measurement is the conductivity of the sample. The bias voltage in range between 0.1 to 2 V must be applied between the tip and the sample allowing the tunneling of the electrons in between those two. The tip for the STM is often made of tungsten (W) or platinum-iridium (Pt-Ir) [74], though for spin polarized measurement the ferromagnetic material such as nickel (Ni) or iron (Fe) is used. The tip-sample distance controlled by the feedback loop and the element is usually in range of 4 to 7 Å, which is equilibrium distance in between repulsive ( $W \leq 3 \text{ \AA}$ ) and attractive ( $W \geq 10 \text{ \AA}$ ) interactions [73].

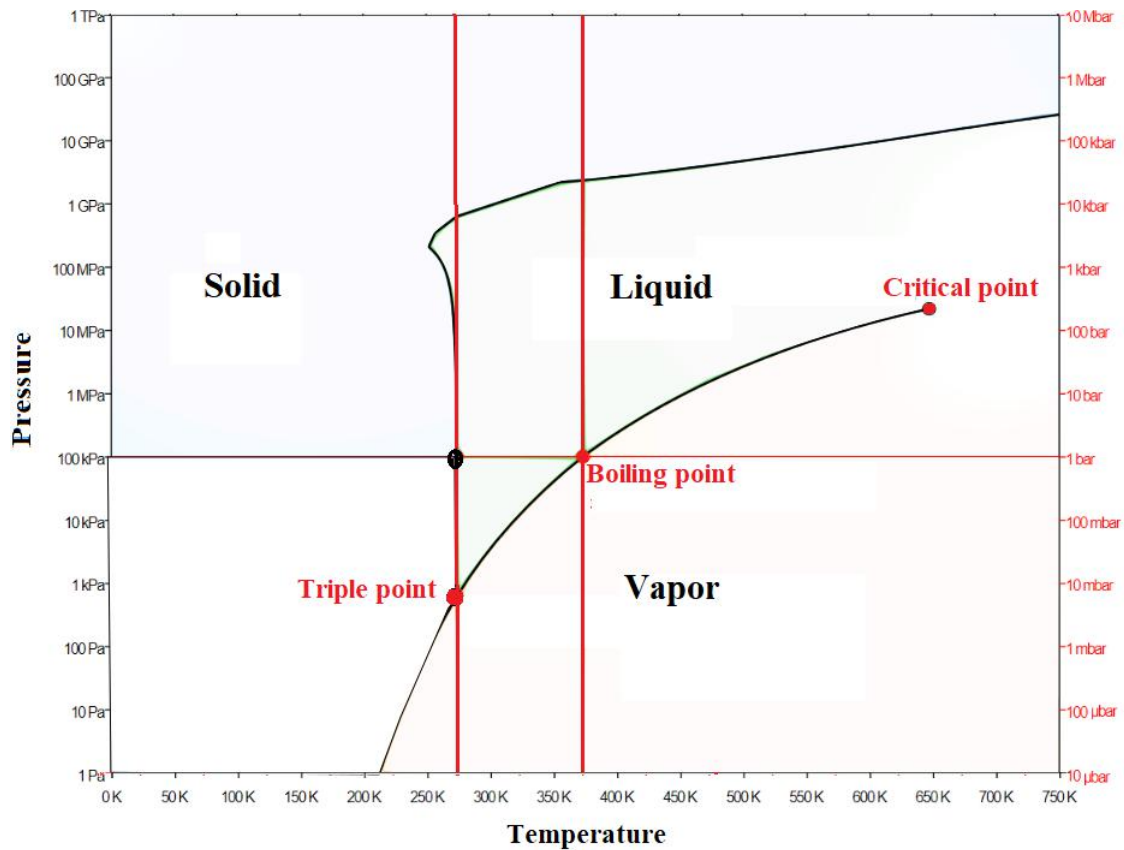
There are two basic imaging modes used in STM: constant current mode and constant height mode. In constant current as the most often used mode, the feedback system keeps constant value of tunneling current between tip and sample by adjusting the voltage while scanning the surface. The change in  $z$  direction on the piezo element is recorded and can be correlated to the topography of the sample.



## 3 DESIGN OF CONDENSATION LIQUID WATER DOSING DEVICE

### 3.1 General Principle

Water exists in three phases: gas, liquid and solid. The equilibrium phase in range of pressures and temperatures can be plotted into phase diagram (Fig. 3.1).



vapor pressure of H <sub>2</sub> O [mbar]	Temperature [K]	Temperature [°C]
$1.03 \times 10^{-10}$	130	-143
$5.78 \times 10^{-8}$	150	-123
6.03	273	0
35.4	300	27

Fig. 3.1: Phase diagram of water with table of relevant values to this work. Calculated with online vapor pressure calculator [62]

In order to achieve high purity of the experiment, samples are moved in and out of the experimental setup at low pressures with water already present in chamber dedicated for the experiment. As can be seen in phase diagram in Fig. 3.1, water at room temperature has vapor pressure at 23.4 mbar and has to be cooled to low

temperatures to decrease its vapor pressure for ultra high vacuum (UHV) transfer of the sample. With cooling of the water to temperatures lower than 130 K, vapor pressure reaches values lower than  $1 \cdot 10^{-10}$  mbar. Within this pressure range it is possible to transfer samples under conditions of UHV. The difference of performing experiment this way compared to making water drop in Argon atmosphere lays not only in cleanliness of conditions in which it is performed, but also in procedure of exposure to a water. While in the previous experiments before depositing liquid water, the sample was in the contact with Ar gas at atmospheric pressure, in this setup the sample is exposed to high pressure of water vapor as the melting process of ice increases its vapor pressure to values in order of millibars.

Principle of the „cold finger“ drop-maker is to cool the small area at the tip to low temperatures and then introduce the water vapor into previously pumped volume closed by a valve from vacuum system. The pressure raises in separated volume to approximately to orders of tens of millibar as it is vapor pressure of water at room temperature. Cooled tip of cold finger then causes vapor to freeze on it and create the layer of ice. For sample to be able to be transferred from vacuum system into water drop setup the layer of ice needs to have its vapor pressure low enough, so it wouldn't evaporate when reaching low pressures ( $\leq 10^{-8}$  mbar), which are present in load-lock part of vacuum system. As can be seen in Fig.3.1 to get stable layer of ice in low pressures, one must achieve temperatures preferably lower than  $-130$  °C or 143 K, by which the vapor pressure of H<sub>2</sub>O is  $8.14 \cdot 10^{-9}$  mbar. With pressures within this range it takes approximately 160 s or more for contaminants to form a monolayer dependent on sticking coefficient of the contaminant. It is an imperative for experiment to preserve its cleanliness for further analysis of samples. For this purpose cooling was chosen to be preformed using liquid nitrogen as its temperature at boiling point is 77 K. With a sample transferred into drop-maker setup, the process of melting ice layer into drop can begin. Pressure again reaches saturation vapor pressure and clean water can drop onto sample. Water is then again pumped to achieve low pressures and enable transfer to main chamber for further analysis.

## 3.2 Condensation Liquid Water Dosing Device (Cold Finger)

„Cold finger“ drop maker depicted in Fig.3.5 is based on flow cryostat principle. Liquid nitrogen is introduced at the top and guided by thin stainless steel capillary to a small reservoir at the tip. To achieve the flow of liquid nitrogen and to limit its expansion inside drop maker as it heats up, excess nitrogen is again guided to the top of the cold finger, where it is pumped through the KF port. To confine the cooled area near the tip, a thin stainless steel wall (thermal conductivity  $16 \text{ W}\cdot\text{m}^{-1}\cdot\text{K}^{-1}$ ) was designed to surround it. To limit water adsorption to the tip of dosing device, the cold finger has a built-in counter heating to create sharp temperature gradient with one end at temperature higher than a room temperature and other end with temperatures of liquid nitrogen.

### 3.2.1 Vacuum Connections

Cold finger outer part that protrudes to the chamber for liquid water dosing is welded to custom designed CF16 flange (see Fig. 3.2). This flange consists of two cylinders in between tube-like connection. Bottom cylinder is standard CF16 flange. Top cylinder is custom flange with three M3 threaded holes on which the top part of cold finger is mounted. Other than that, there is extruded area with H7/h6 tolerance, which ensures tight fit of top part onto flange.

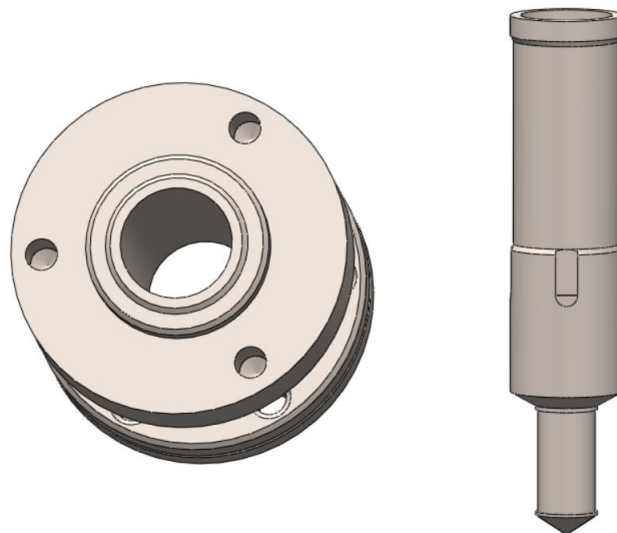


Fig. 3.2: 3D model of custom CF16 on a left and body of the cold finger on a right.

Cold finger body has tube-like shape with tip ending. For easier welding of body to custom flange, the thickness of top of the body matches protruding area of the

flange with 1 mm wall. To avoid creating a hardly accessible volume (virtual leaks) from the inner side of flange, thickness of the body is reduced ifrom here to length of the flange and is finished with four grooves, to achieve better pumping efficiency inside the chamber.

To minimize heat transfer from „hotter“ areas at he top of device to the cold tip and thus creating sharp temperature gradient the thickness of the area near the tip is reduced to 0.3<sup>1</sup> mm.

### 3.2.2 Heating and Temperature Measurement

Counter heating inside the cold finger is designed to create temperature gradient on the outer walls and thus create well defined interface between frozen water and upper parts of the drop maker. This is performed by copper heating body(see Fig. 3.3) inside the cold finger body that is pressed by spring loaded washer (spring A, Fig. 3.5) that provide pressing force of 18.5 N to ensure good contact of heating body with the wall. At the bottom, the heating body is widened to provide its straight guidance into drop maker. Heating is implemented by resistive wire (diameter of 0.25 mm, Kapton insulated Chromel) with total resistance of 39.8  $\Omega$ .

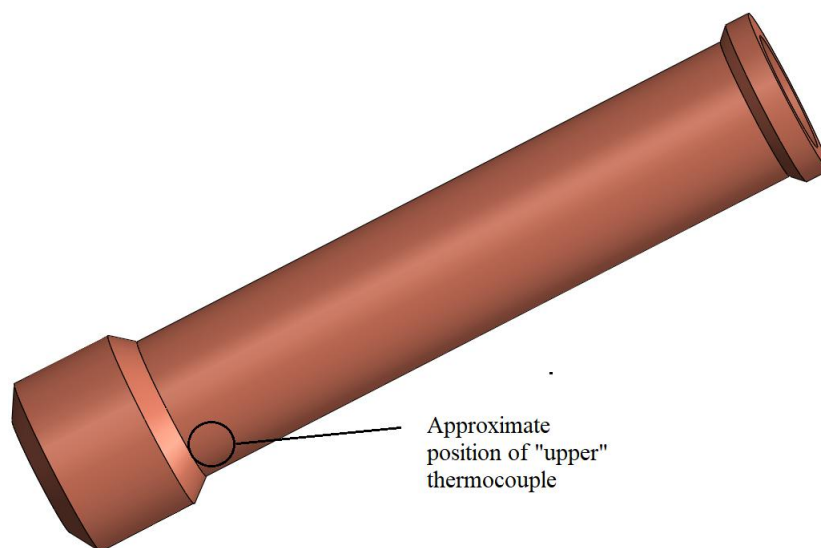


Fig. 3.3: Heating body of the cold finger

Temperature measurement is carried out by two K-type thermocouples at exhaust tube near the heat-exchanger and other one on the copper heating body. Measurement on the „low temperature“ thermocouple is intended to be used as reference for the experiment. When the temperature reaches set value ( $\approx -80^{\circ}\text{C}$ ) the process of

<sup>1</sup>smallest thickness that could be machined in workshop

freezing water may begin. Temperature of „hot temperature“ part (set to 40°C) is controlled by PID-regulated power supply.

Both the outputs for temperature measurement and heating input are connected to single KF16 feed-through with three K-type thermocouple pairs. Schematic view of connections in feed-through is in Fig.3.4. A-B port is used for thermocouple measuring low temperatures, with A being Chromel connection and B being Alumel connection. C-D (C-Chromel, D-Alumel) port is used for thermocouple for controlling the temperature of heating body. E-F (E-Chromel, F-Alumel) port is used for the heating.

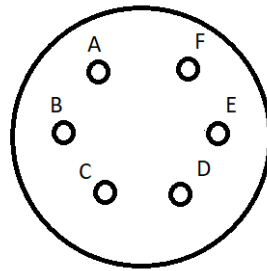


Fig. 3.4: Schematic view of the feed-through input/output ports. A-B thermocouple for low temperatures, C-D thermocouple for heating control, E-F heating wire

As power supply CreaTec CU-3504-S1-DC capable to supply up to 13 A and 120 V was used. This power supply is also equipped with PID controller Eurotherm 3504 used for temperature stabilization of the heating element. For the cold finger the maximal power is set to 50 %, which is roughly 100 W (55 V and 1.8 A) and the PID parameters were auto-tuned during the cooling of the drop maker at low temperatures. These parameters give the good stability during the experiments.

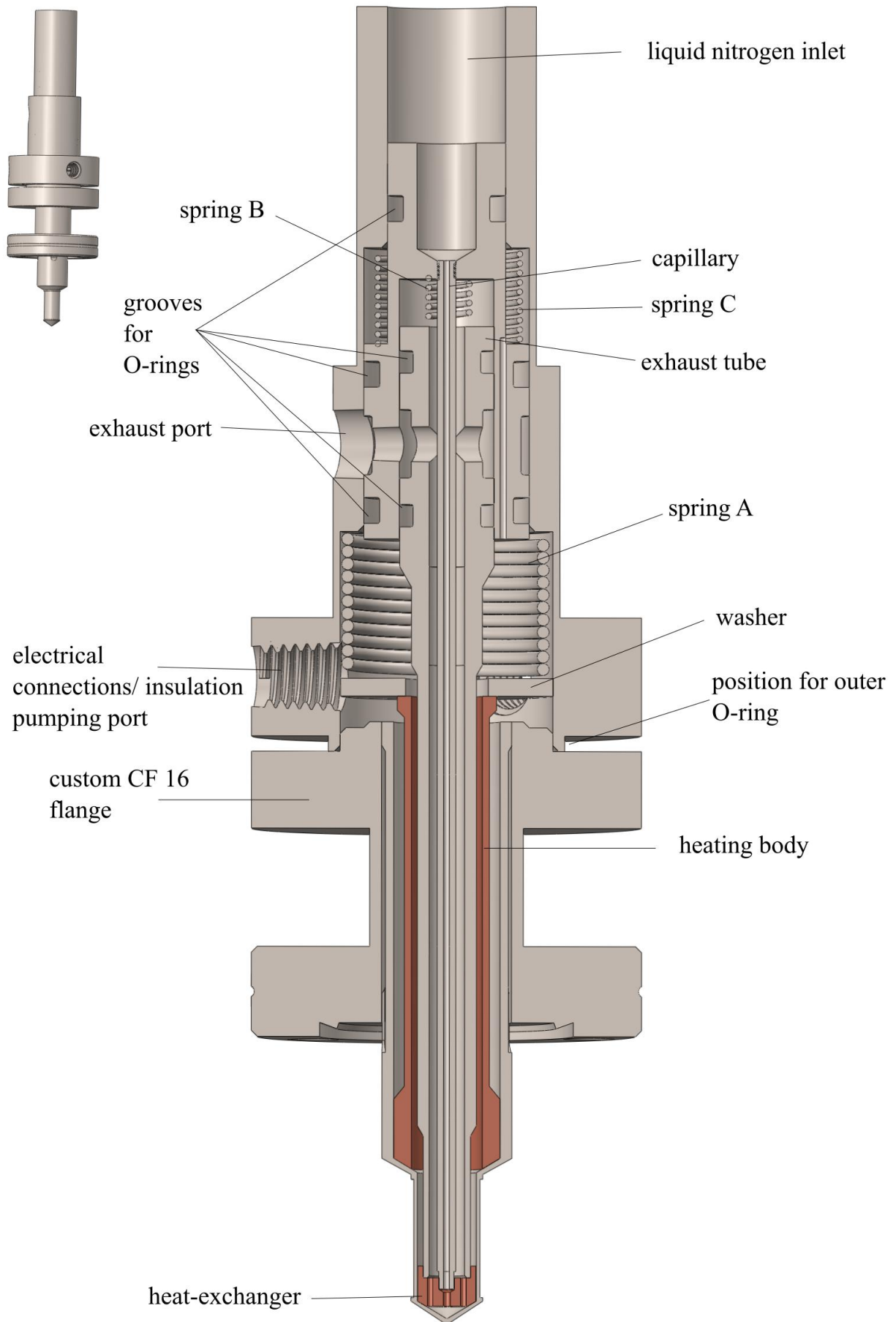


Fig. 3.5: Section view of the cold finger.

### 3.2.3 Liquid Nitrogen Supply

The cooling of the cold finger is realized by introducing liquid nitrogen inlet (Fig. 3.5) at the top of the drop maker. Nitrogen then flows (Fig. 3.7) through the capillary fixed to an adapter part with the thread insulated by Teflon tape. This eliminates the flow of nitrogen around capillary into other parts of the cold finger. The thickness of the walls of the capillary is reduced at the bottom part and the capillary is pressed with interference fit into copper part in the bottom (shown in Fig. 3.8).

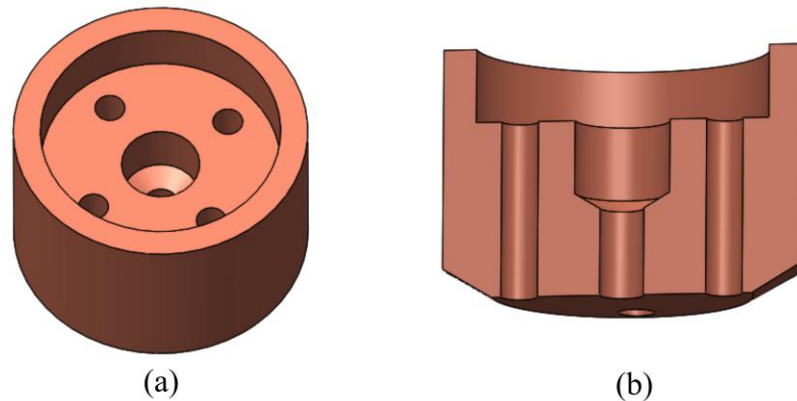


Fig. 3.6: Heat-exchanger of the cold finger. (a) Top view. (b) Section view.

This part(see Fig. 3.6), also manufactured with h6 tolerances to ensure tight fit into body of the cold finger, acts as holding piece for the capillary and the exhaust tube at the bottom as well as heat exchanger due to large thermal conductivity of copper ( $401 \text{ W}\cdot\text{m}^{-1}\cdot\text{K}^{-1}$ ), to effectively cool walls around it. Under the heat-exchanger there is small reservoir of nitrogen with volume of approximately  $3.2 \mu\text{l}$ , which is also the coldest area effectively on a temperature of liquid nitrogen.

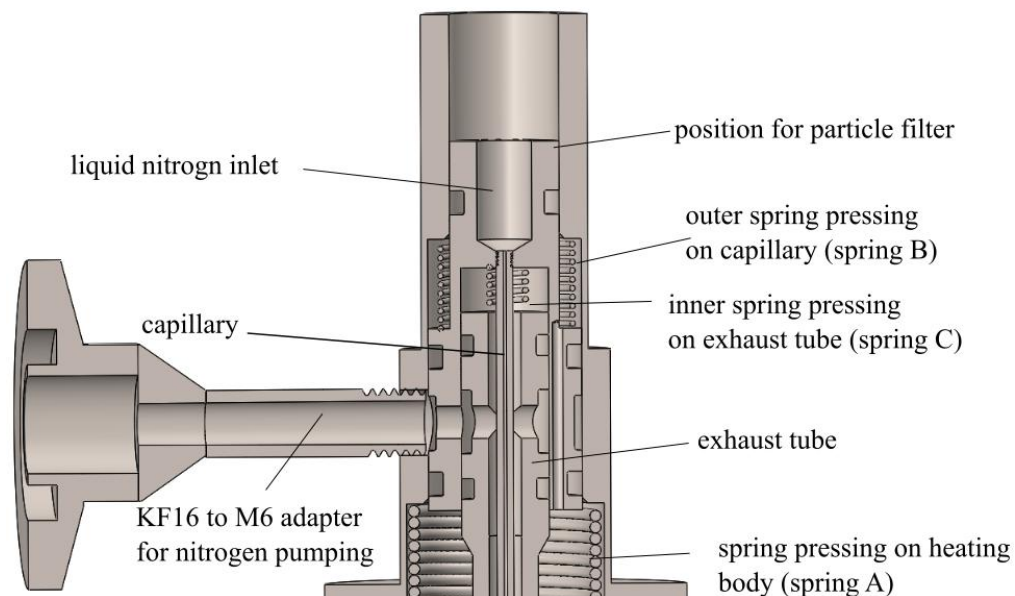


Fig. 3.7: Section view of the liquid nitrogen exhaust in upper part of the cold finger

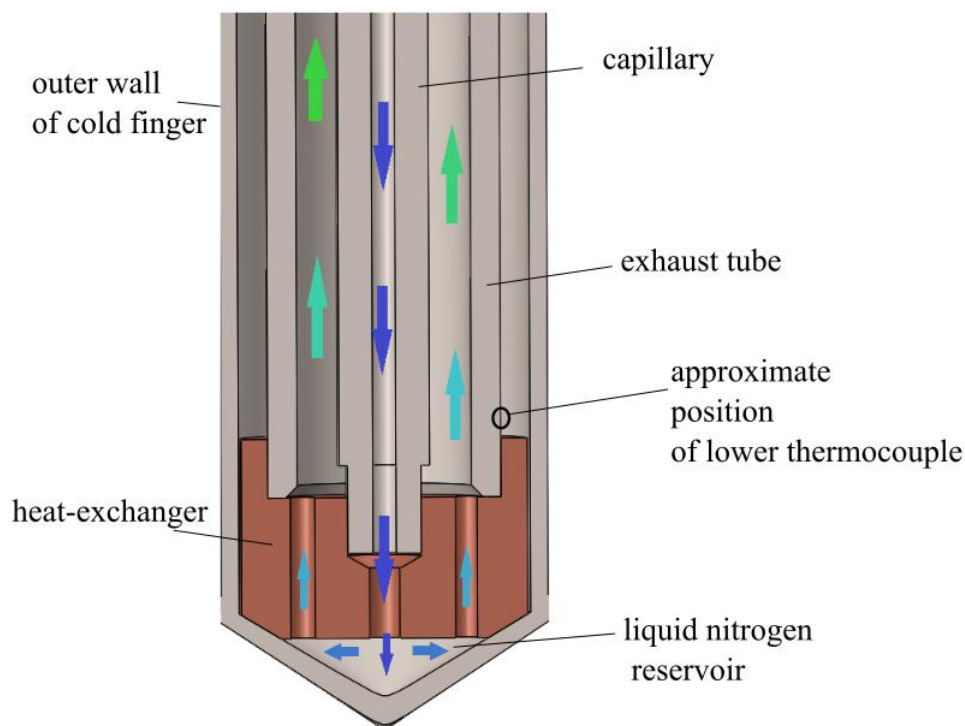


Fig. 3.8: Section view of the tip of the cold finger. Arrows symbolize the flow of liquid nitrogen in the cold finger.

To ensure flow through drop maker and limit unwanted expansion of gaseous nitrogen, which could damage inner parts, excess nitrogen is pumped through the exhaust line. It was designed as stainless steel tube concentric to capillary. It is also pressed to copper heat exchanger with a tight fit. In heat-exchanger four exhaust

holes with diameter of 0.5 mm around central inlet hole were designed to ensure flow of expanding nitrogen into the exhaust tube. Nitrogen is then pumped through the exhaust tube to upper part of the cold finger (see Fig. 3.7) and through KF16 to adapter out of the device. The sealing of the exhaust line, is ensured by H7/h6 fit of exhaust tube into adapter at the top, as well as the O-rings in it. Concerning the low temperatures involved in experiment, the proper material has to be considered to be used for O-rings. The O-rings made out of polytetrafluoroethylene (PTFE) for their mechanical stability at low temperatures are usually used. However, as this is case of static sealing, viton O-rings provide sufficient sealing with lower cost and better flexibility.

To store the liquid nitrogen during the experiment, a double walled container (see Fig.3.9) with volume of 0.3l is used. For the use in cold finger it had to be modified so the flow of nitrogen would lead directly into liquid nitrogen inlet port without any streaming into space around it. This is done by using adapter made out of polyether ether ketone (PEEK) ( Fig. 3.9) mounted in between the top of the cold finger and the container. This material was chosen for its small thermal conductivity ( $0.25 \text{ W}\cdot\text{m}^{-1}\cdot\text{K}^{-1}$ ) because lowest possible heat transfer is required in nitrogen input line. The top of the adapter is meant to be secured inside the container with a nut screwed on the thread. This nut also a press on the O-ring inserted in between the nut and the container to provide sealing of outer wall from the nitrogen. Bottom of the adapter is designed to precisely fit on the top of the cold finger with groove for another O-ring for a better sealing. It has proven to be important to always have filter present in between the adapter and the cold finger in order to stop particles that might clog the capillary and stop the flow of the nitrogen. Filter used for this purpose was cut off from KF particle filter secured by stainless steel grid and weighted down by two washers.

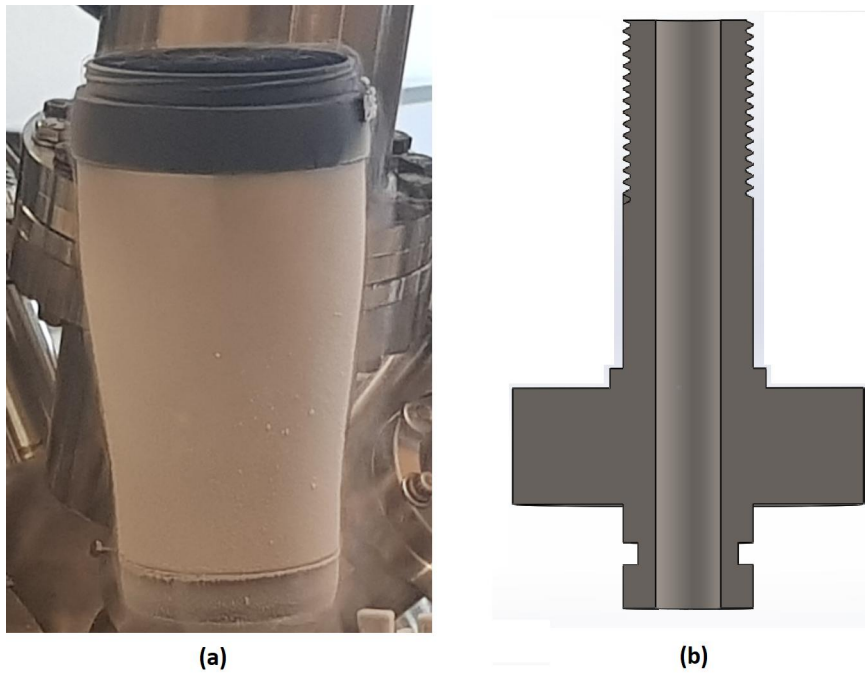


Fig. 3.9: Container for liquid nitrogen (a) and section view of adapter for liquid water doser (b).

Another option for liquid nitrogen supply is to use larger double walled container with volume of 2l. In this case the adapter to cold finger is more complicated as it requires welded connections and a pumping port for insulation. This adapter is shown in Fig. 3.10. Top of the adapter is welded on the inner wall of the double walled container and lower platform with pumping port is welded to outer wall of the container. From top side, there is drilled hole with M8 fine thread intended for plug that would control the flow and stop it after the ice layer is formed. The bottom part is drilled with precision for good fit around cold finger's outer diameter and is followed also with M8 threaded hole. Connecting part made out of PEEK is fitted inside to provide better insulation and a platform for particle filter on the top.

To achieve better insulation and thus more effective nitrogen cooling in double walled container, M6 threaded port (Fig. 3.10) was designed, intended for pumping and thus creating rough vacuum insulation in container.

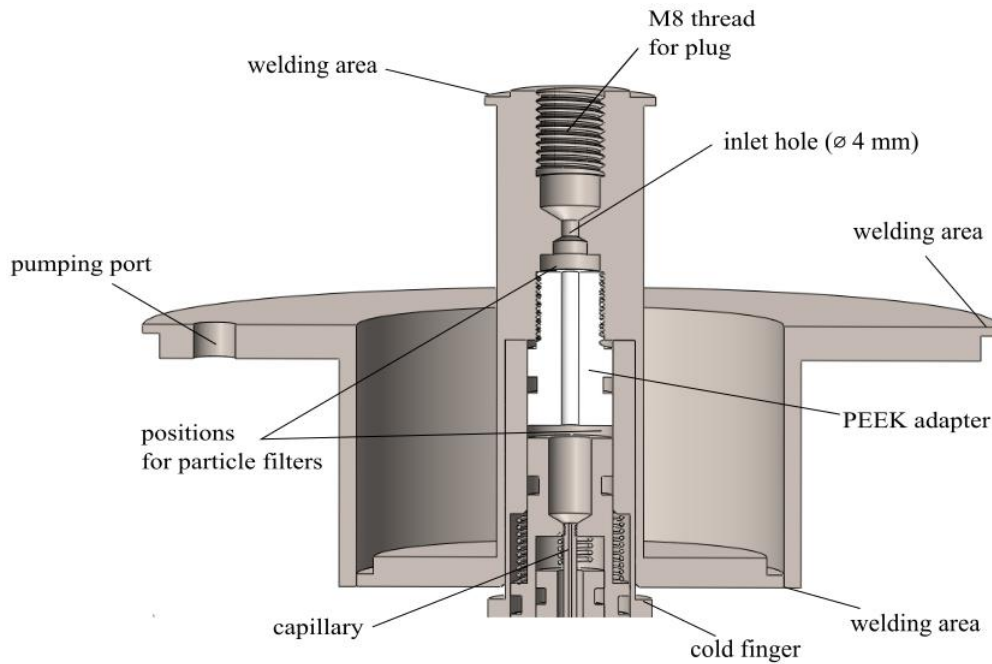


Fig. 3.10: Section view of the adapter for larger vacuum insulated container for liquid nitrogen.

### 3.2.4 Insulation

To limit the decrease in cooling power through the heat transfer by convection, the design of the drop maker allows for pumping areas around the liquid nitrogen flow line and heating element to create efficient heating/cooling system. As was mentioned in subsection 3.2.3 the series of the viton O-rings (Fig. 3.11) were put around liquid nitrogen inlet and outlet to guide the flow into pumping port. These O-rings together with H7/h6 tolerances ensures sealing of the parts that come into contact with liquid nitrogen. Another O-ring is placed on the top part of the cold finger near the flange (Fig. 3.5) to ensure sealing inner parts from ambient pressure.

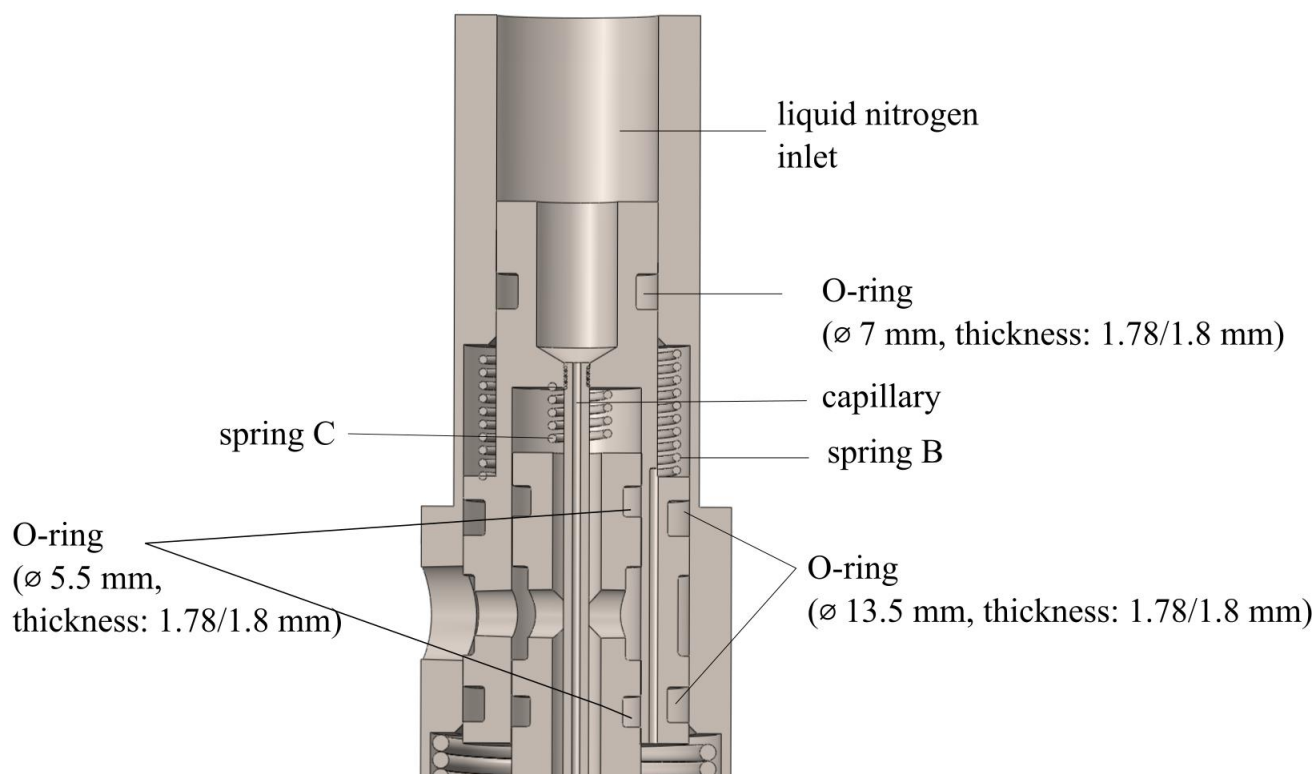


Fig. 3.11: Sectional view of the top of the Cold finger with marked grooves for O-rings

To ensure sealing of the bottom parts, the heat-exchanger, capillary and the exhaust tube are pressed by compression springs (section 3.2, Fig. 3.5 and Fig. 3.11). Table with relevant values are shown in Fig. 3.12. The smallest of the springs (spring C) is pressing directly on a exhaust tube with effective force of 2 N. Medium sized spring (spring B) is pressing through inner adapter on a capillary with effective force 26 N. With negligible weight of inner adapter the total force pressing on copper heat exchanger is around 28 N. The biggest spring (spring A), as mentioned in subsection 3.2.2, presses on heating body to make a better thermal contact between it and cold finger body.

Pumping is carried out through the port with M6 thread under the nitrogen exhaust. The same adapter as mentioned in subsection 3.2.3 can be used. To reduce inner volume, feed-through with heating wire and thermocouples is combined with pumping port through KF16 T-tube. Using a rotary pump to create an insulating vacuum, the pressure of  $3.0 \cdot 10^{-1}$  mbar (measured on Pirani gauge) can be achieved.

Springs	Force[N]
A	18.5
B	26
C	2

Fig. 3.12: Table of used springs and their pressing forces.

### 3.3 Experimental Setup

Experimental setup (see Fig. 3.13) consists of small chamber designed exclusively for water drop experiments separated by a gate valve from the load-lock of the main chamber. It contains drop maker for dosing liquid water situated over the sample and container for clean water connected to chamber via Fujikin valve. On the opposite side, there is liquid-nitrogen-cooled sorption pump connected again by valve to chamber for pumping residual water vapors. The sample is transferred into setup by magnetic rod and is held in place by spring loaded custom made holder.

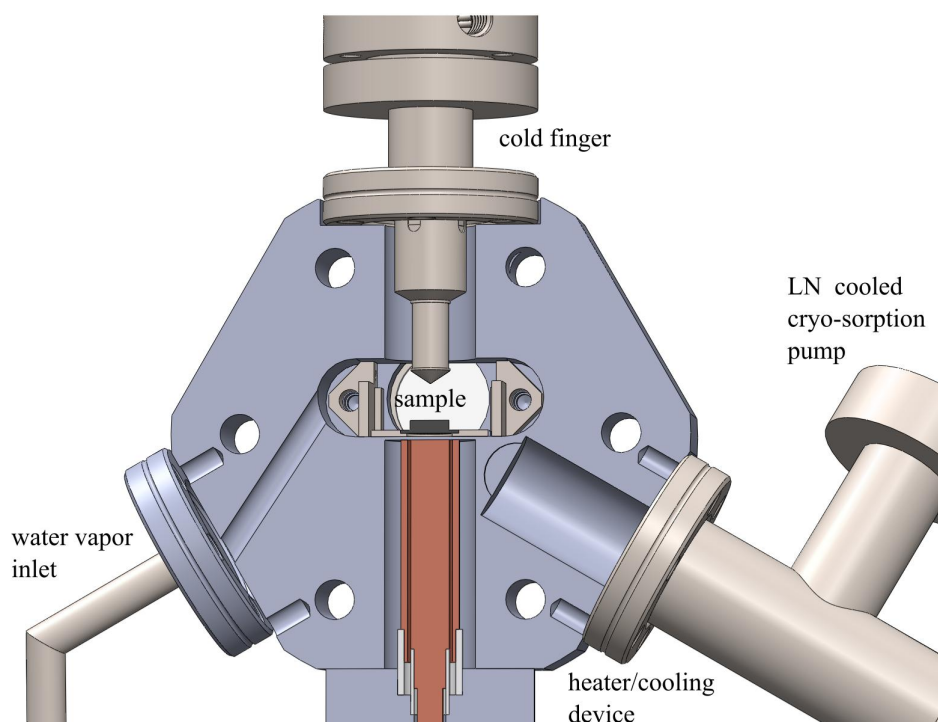


Fig. 3.13: Section of the experimental setup for water drop experiments

#### 3.3.1 Chamber for Liquid Water Dosing Experiments

As there is need to transfer the sample in and out of the setup at low pressures ( $\approx 10^{-7}$  mbar) quickly to keep them as clean as possible, the setup has to be pumped

and ready at short time. Water tends to adsorb on surfaces at high (atmospheric) pressures and desorb as vapor during pumping, as described in phase diagram in Fig. 3.1, making it difficult to achieve desired vacuum. For this reason the chamber was designed with aim to minimize volume and inner surface area.

To eliminate the need of mounting the chamber to the gate valve through the nipple, and thus greatly reduce inner volume and surface area, the custom chamber (see Fig. 3.14) was designed. It was chosen to be a hexagonal shape with CF40 port in the front and CF16 on sides. This shape allows for mounting holes to go through whole chamber and install it directly on a gate valve. The inner volume of the hexagonal chamber is 64.45 ml. As the means of observation of the sample during the transfer and water drop experiments, standard CF16 port was positioned in the back side of the chamber with offset of 6 mm from the axis for the best possible view through the view port.

Main volume consisting of slot with curved sides with depth of 30 mm (Fig. 3.14) is intended as the space where the water drop experiment is performed. In order to move sample into desired position with magnetic rod can half circular slot (Fig. 3.14) located below the main volume was designed. Its length of 10 mm is set precisely for a sample to be centered under the drop maker.

Bottom port is intended to hold heating/cooling body that would transfer heat through thin wall onto sample. It was designed under the platform where sample plate slides in, with thin wall of 0.5 mm in between it and sample plate (see Fig. 3.15).

Top port (see Fig. 3.14 and Fig. 3.15) is meant to hold the drop maker. To minimize the water drop spreading in chamber, this CF16 is embedded into hexagonal chamber by 4 mm. The distance between the tip of the drop-maker and the bottom plane of the chamber is set to 8.1 mm. Using standard UHV sample plates it makes vertical space of 7.1 mm from surface of the plate to the tip.

For water vapor inlet a side CF16 port is used. Water container is mounted on the CF16 port and separated by Fujikin valve. This port holds the inlet hole (Fig. 3.15) tilted from the axis of CF port. It was designed to limit the restrictions in the path for the water vapor flow to reach drop maker. To increase the cleanliness of the experiment and effective pumping of the vapor, another CF16 port on the other side was designed (Fig. 3.15) to hold custom made cryo-sorption pump. This port (diameter of 14 mm) is intersected with hole with diameter of 10 mm from the front side (see Fig. 3.14). Purpose of this pumping port is to achieve growth of ice layer under the flow of vapor rather than in water vapor environment. This decreases the possibility of contamination from surrounding walls and provides better control over growth of the ice layer and to pump remaining vapors after experiment.

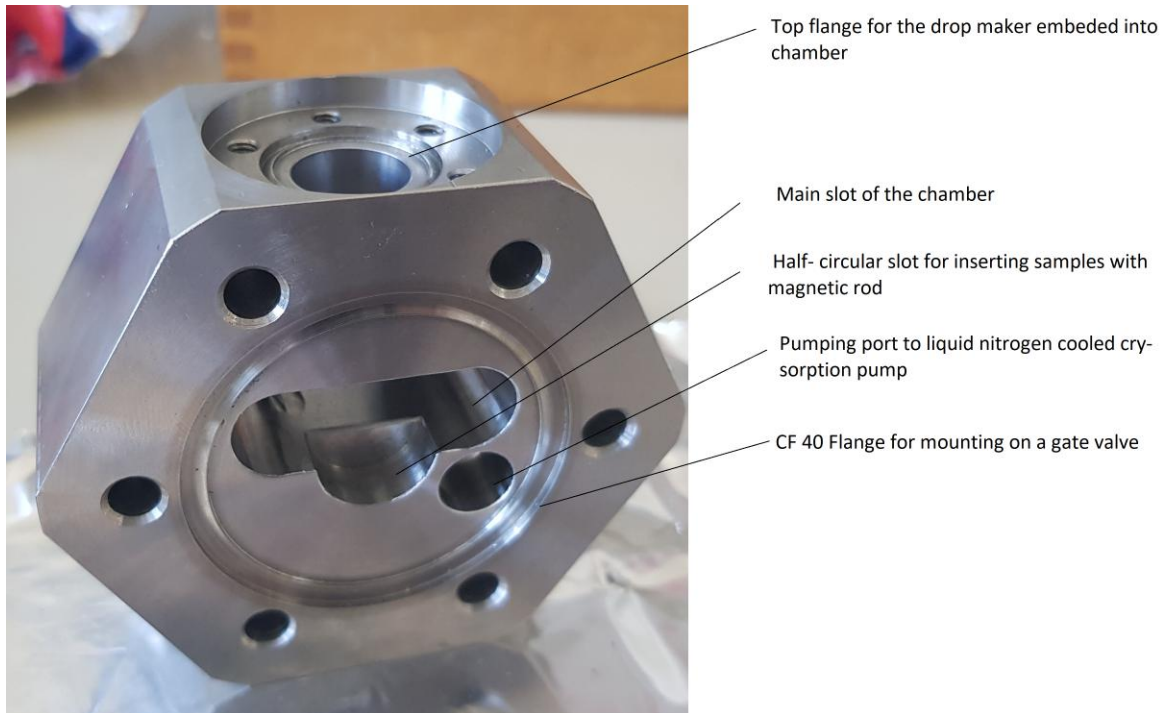


Fig. 3.14: Chamber for water drop experiment

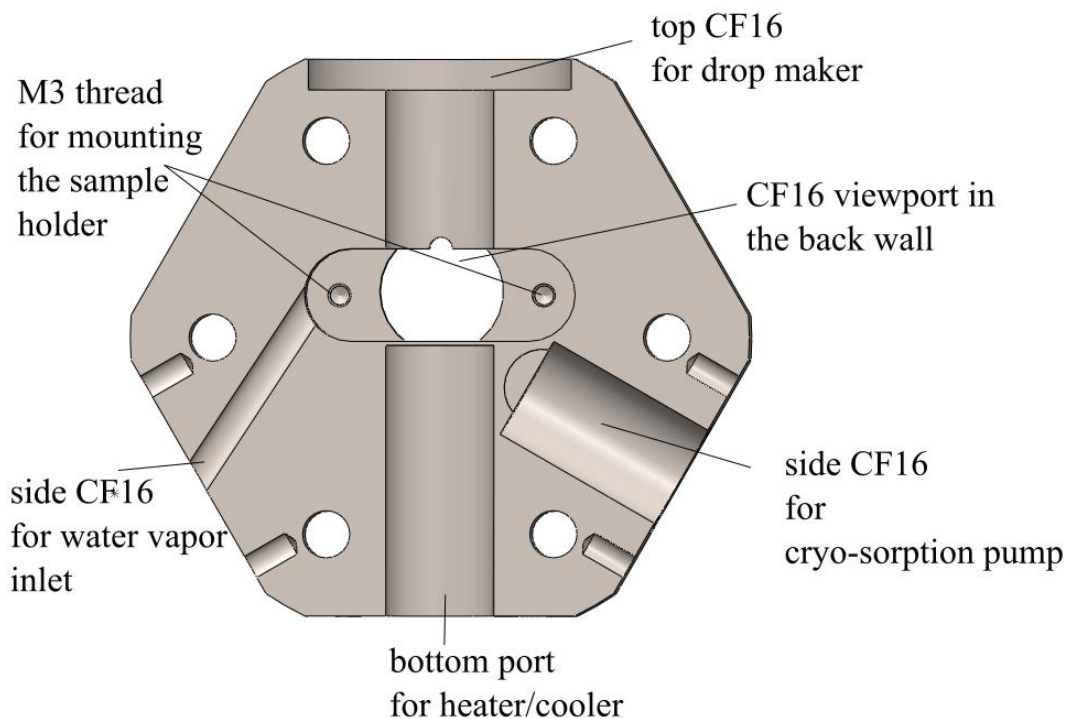


Fig. 3.15: Section view of chamber for water drop experiment

### 3.3.2 Sample Holder

As the material for the sample holder, stainless steel AISI 304 again was chosen. It is secured by two M3 screws to the back wall (see section 3.3.1, Fig.3.16). The height of the holder was designed and manufactured with such precision (h6 tolerance) to fit exactly into main slot of the chamber to avoid rotation. For centering of the sample plate under the drop maker, 1 mm sheet of stainless steel of the same width with length (5 mm) was inserted to holder to act as stop mechanism for the plate. In order to unmount the sample plate from magnetic rod a pressing force must be applied to keep the sample in place This done by springs made out of stainless steel wire (diameter of 1 mm) secured by M2 screws in top part of the holder.

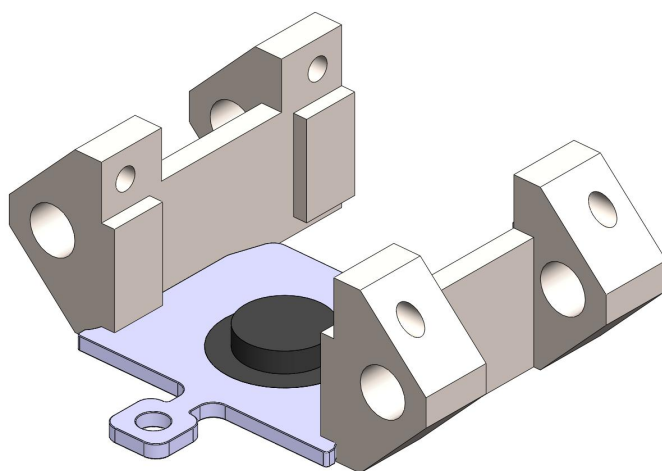


Fig. 3.16: Model of the sample holder

### 3.3.3 Cryo-Trap

In order to improve and maintain sufficiently low pressures ( $\approx 10^{-7}$  mbar) an in situ LN<sub>2</sub> cryo-sorption pump (Fig.3.17) contained in CF40 T-tube was designed. Stainless steel (AISI 304) reservoir is welded onto standard CF40 flange, with input and exhaust ports protruding through the flange. In order to mount copper sheet cylinder with thickness of 1 mm, two M4 threaded holes were designed in thickened bottom of the reservoir. The cylinder acts as effective adsorption area while being cooled with liquid nitrogen.

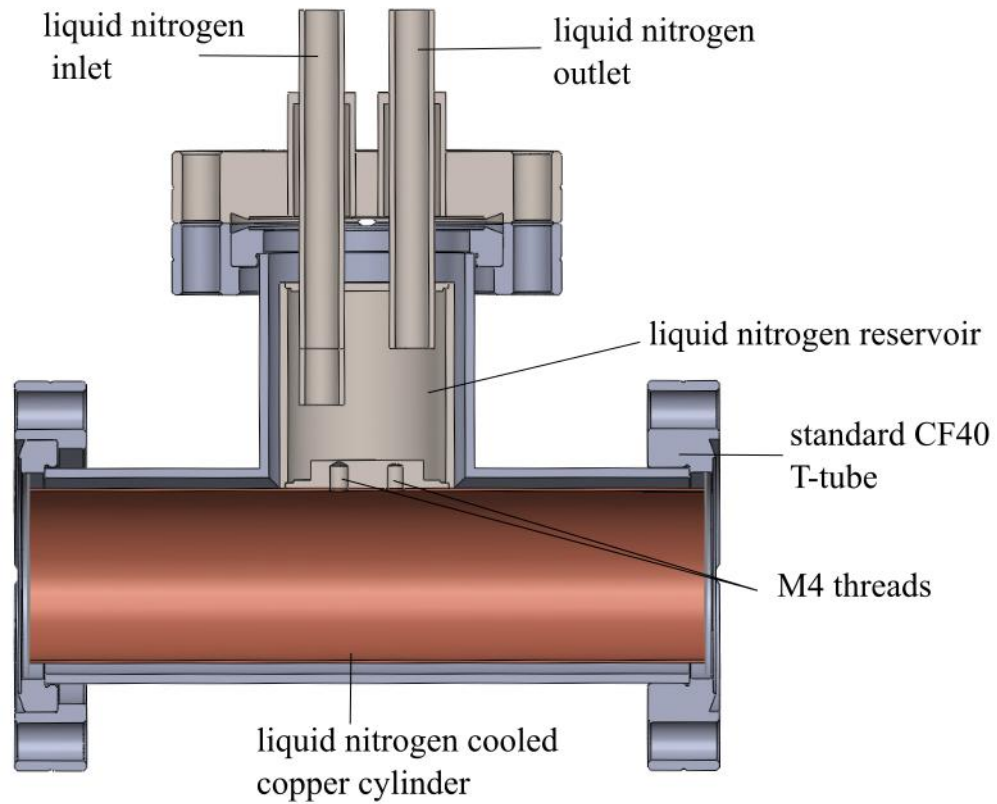


Fig. 3.17: Section view of Cryo-trap model used for improving pressures in vacuum system during sample transfer.



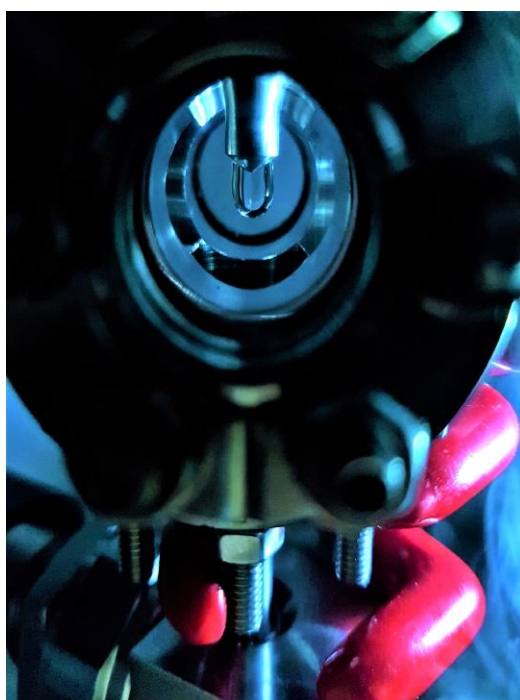
## 4 TESTING OF THE EXPERIMENTAL SETUP

### 4.1 Experimental Procedure

Experimental procedure of dosing liquid water onto samples starts with pumped system with sample in analysis/preparation chamber. The gate valve separating chamber for water drop experiments from other parts of the system is closed and the cooling of the drop maker can begin. After achieving stable low temperature on the drop maker, the valve to pre-cooled cry-sorption pump is opened. This step is done to limit exposure of the inner walls to water vapor and achieve growth of the ice layer under flow, which decreases probability of contamination of water. Afterwards the Fujikin valve to water container is opened and water vapor is introduced into chamber and to cryo-sorption pump, passing through the drop maker and condensing on the tip. With water at the room temperature, 30 s of exposure is enough in order to condense enough water that will drop by its own weight after melting. With ice layer present on the tip of the drop maker (Fig. 4.1(a)) the both valves into water container and cryo-sorption pump are closed. Sample is now moved from main chamber into transfer line and the gate valve into drop maker is opened and sample is inserted inside. With sample ready for liquid water drop, the gate valve into setup is again closed and process of melting the ice layer begins. By stopping the supply of the liquid nitrogen, the temperature rises assisted by counter heating, which leads to melting of the ice and rising the pressure inside the chamber to vapor pressure of the liquid water (Fig. 4.1(b)). After the liquid is dropped on the sample the valve into cryo-sorption is opened again and liquid is pumped away to achieve UHV conditions again. After water is pumped away the gate valve into transfer line is open and sample is moved into main chamber for its analysis.



(a)



(b)

Fig. 4.1: Water drop on the drop maker.(a) Frozen state during sample transfer. (b) Water drop just before deposition on the sample. Images were taken in test setup.

## 4.2 Results of the Experimental Testing

The water in contact with cold finger may get contaminated by elements present in stainless steel (chromium, nickel, iron, etc.). Moreover, other contaminations adsorbed on the inner surfaces of experimental setup that might be soluble in water might influence purity and thus results of performed experiment. Therefore these possible contaminants have to be inspected and evaluated.

### 4.2.1 Ag Foil

To inspect the contaminations present within experimental setup, the water drop experiment was performed on silver foil sample. Sample was prepared in main chamber by sputtering in Ar ( $p = 1.5 \cdot 10^{-6}$  mbar,  $E = 1000$  eV,  $t = 30$  min). Analysis of the chemical composition was done by X-ray Photoelectron Spectroscopy (XPS) and Ion Scattering Spectroscopy (ISS/LEIS). Overview spectrum measured with Mg (excitation energy of 1253.6 eV) anode is shown in Fig. 4.2 in red color. It can be seen that there is signal from C 1s at 284.5 eV, which is assigned to adventitious carbon on the sample. This carbon is common contamination on samples in vacuum and can be eliminated by increased number of cleaning cycles.

In XPS spectrum after water drop experiment (Fig. 4.2, blue color) an increase of signal from C 1s at 284.5 eV is detected. This may be caused by exposing sample to higher pressure in load-lock ( $\approx 10^{-6}$  mbar). At energy around 531 eV, the signal from oxygen O 1s is present, which can indicate water present on the surface, but can also be caused by increased carbon signal if carboxylic species are adsorbed on the surface. Metal contaminants of Cr, Ni and Fe were not detected.

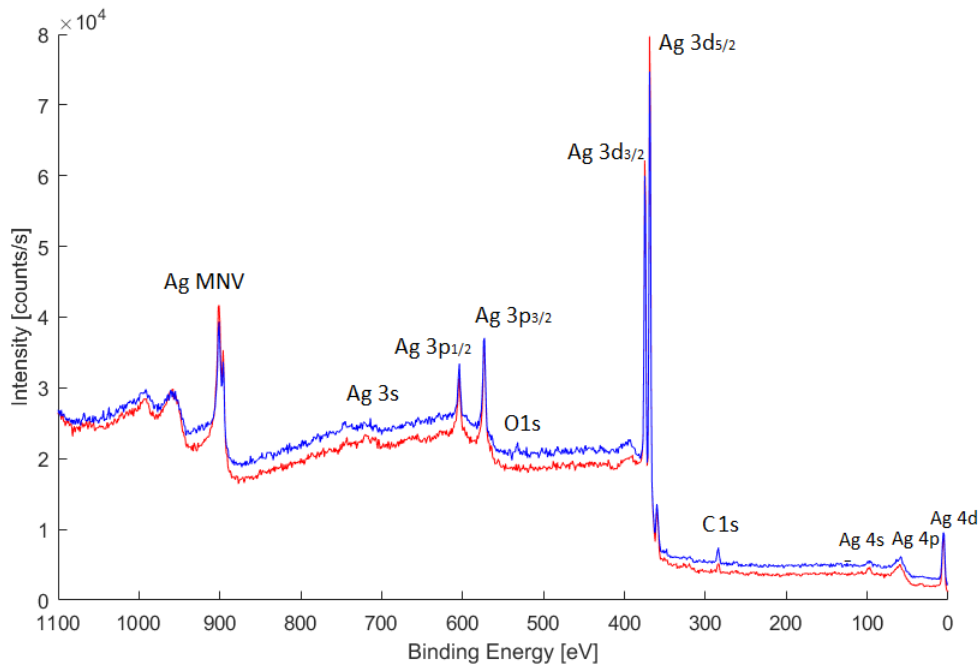


Fig. 4.2: XPS spectrum of cleaned silver foil surface (red) and after water drop experiment (blue).

LEIS was measured using He ions ( $p_{\text{He}} = 5 \cdot 10^{-8}$  mbar) with incident energy of 1225 eV with scattering angle of  $137^\circ$ . Due to inelastic processes, actual peak energies in LEIS are lower than the values calculated. The energies are calibrated to the high-energy baseline of the peak for identification of elements. In the spectrum ( Fig. 4.3 and Fig. 4.4, purple color) of cleaned Ag foil, there is main peak of Ag at kinetic energy of 1077 eV. Second peak with low intensity is detected at 825 eV (Fig. 4.4, purple). This energy roughly corresponds to chlorine and it is visible in both spectra before and after the water drop.

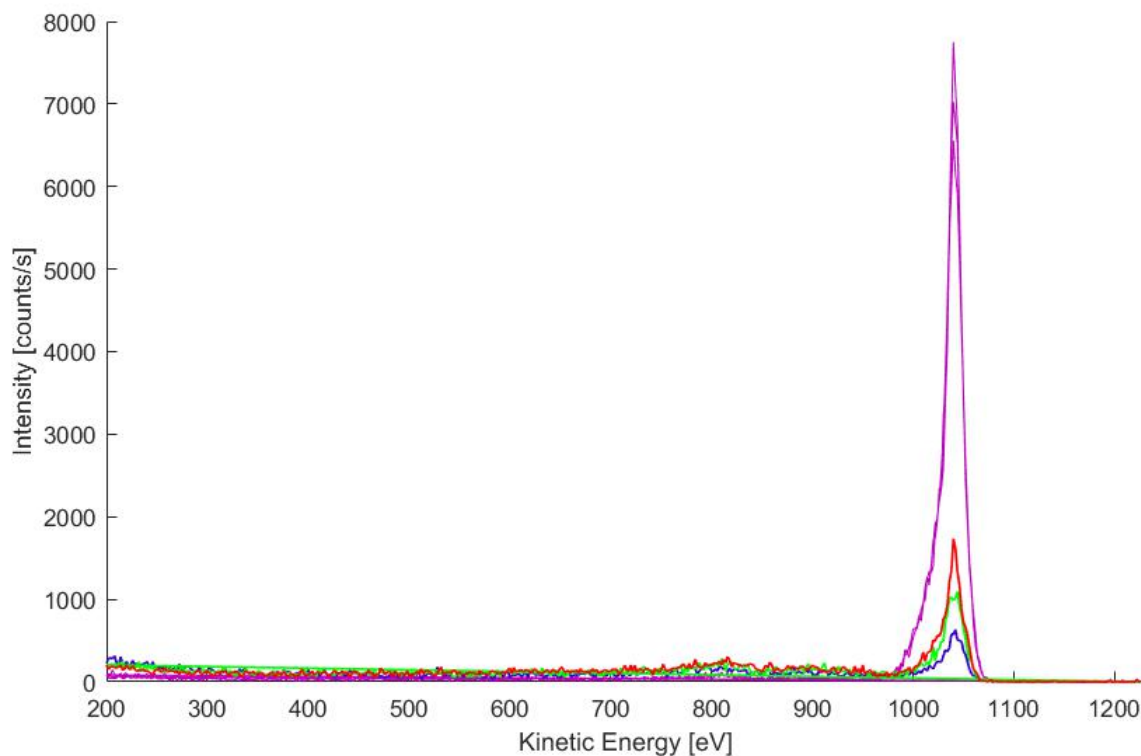


Fig. 4.3: LEIS spectrum of cleaned silver foil surface (purple), 1<sup>st</sup> scan after water drop (blue), 2<sup>nd</sup> scan after water drop (green), 3<sup>rd</sup> scan after water drop (red)

In the first scan after water drop experiment (Fig. 4.3, blue color) signal from the Ag (1077 eV) is significantly reduced as well as the background raised at lower energies. This indicates the presence of adsorbed layer on the sample. This is supported by the fact that with repeating scans in the same position (green and red color) the intensity of substrate signal is increasing, meaning that layer on the surface is desorbed or sputtered away. From chemical analysis point of view, the scan shows three distinct elements present in the sample. Considering detailed spectrum in Fig. 4.4, it can be seen that besides main peak of Ag (1077 eV) there are smaller peaks at 825 eV and 950 eV. Whereas the first one was detected also on the clean sample and can be associated with bulk contamination of sample, the second peak at 950 eV appears only after water-drop experiment. This can be interpreted as a contamination of water droplet by stainless steel as the energy of the peak corresponds with Fe (955 eV).

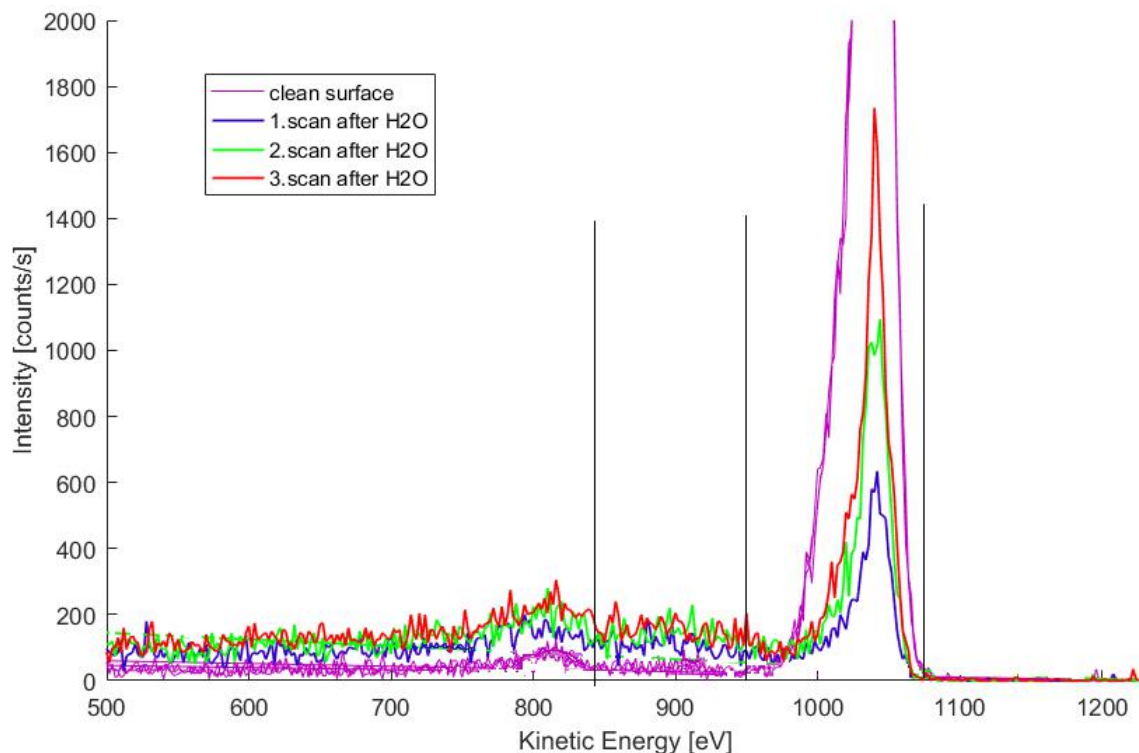


Fig. 4.4: Detail of LEIS spectrum of silver foil surface before and after water drop.

### 4.2.2 $\text{Fe}_3\text{O}_4(001)$

To get a more accurate view on the effects of possible contaminations on single crystal oxide surface, the  $\text{Fe}_3\text{O}_4(001)$  was selected as the testing surface as its structure is quite well understood; the reader is referred to [15] and [24] for more comprehensive information on this material.

#### Sample Preparation

The clean  $\text{Fe}_3\text{O}_4(001)$  surface can be prepared by cycles of Ar sputtering ( $p_{\text{Ar}}=1.5 \times 10^{-6}$  mbar, 1.5 kV,  $2 \mu\text{A}$ ) and annealing ( $630^\circ\text{C}$ , 20 min) with the last annealing step done in  $\text{O}_2$  ( $p_{\text{Ar}}=1.0 \times 10^{-6}$  mbar,  $630^\circ\text{C}$ , 20 min). This step is done in order to regrow new layers of pristine surface with Surface Cation Vacancy termination. Omitting the  $\text{O}_2$  annealing leads to characteristic defects appearing on the surface or reducing the surface to Fe-dimer termination [15]. Another important step is to cool the sample in UHV after  $\text{O}_2$  annealing, otherwise the surface is covered with small islands instead of large atomic terraces.

## Clean Surface

The clean surface can be recognized as it features characteristic rows in the STM image. The „wide“ and „narrow“ sites can be identified on the rows. Such surface can be seen in Fig.4.5, which represents empty states STM image. Rows in this image consists of Fe cations as they have higher density of states in vicinity of Fermi level compared to O anions which are topographically on a same level.

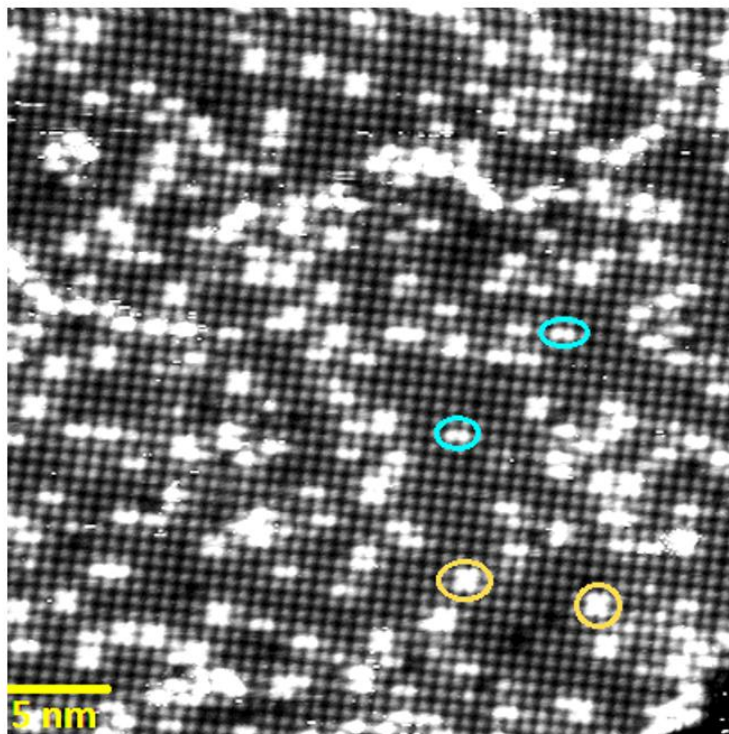


Fig. 4.5: The  $30 \times 30$  nm STM image (1.4 V, 0.113 nA) of clean surface of  $\text{Fe}_3\text{O}_4$  (001). Image displays characteristic defects found on the surface: adsorbed hydroxyls (blue ovals) and wide site defects (orange ovals).

Freshly prepared surface always exhibits defects and abnormalities from theoretical model. The most common are *adsorbed hydroxyls* (orange ovals Fig.4.5) from residual gas in vacuum chamber, which reacts with surface oxygen vacancies, *stationary wide site defects* (blue ovals Fig.4.5), which are unreconstructed unit cells and *Anti-phase boundary domains*, which are formed by meeting of forming reconstruction from different nucleation sites. For more detailed explanation, reader is again referred to [15].

## Chemical Analysis of Water Drop Experiment

Similarly to subsection 4.2.1, the goal was to inspect contaminations present in experiment and their interaction with surface as well as the interaction of water drop itself with  $\text{Fe}_3\text{O}_4(001)$ . Chemical composition was analyzed by XPS using Mg anode (excitation energy of 1253.6 eV) at grazing emission ( $70^\circ$  from sample normal) and is shown in the Fig. 4.6. It is important to note that the detailed spectra including carbon C 1s and oxygen O 1s were normalized to the ten last values of constant background at low energy side of spectra. From XPS spectra of first water drop it can be seen that significant Na contamination is present on the sample with Na 1s (1072 eV) and Na Auger (260 eV) peaks visible.

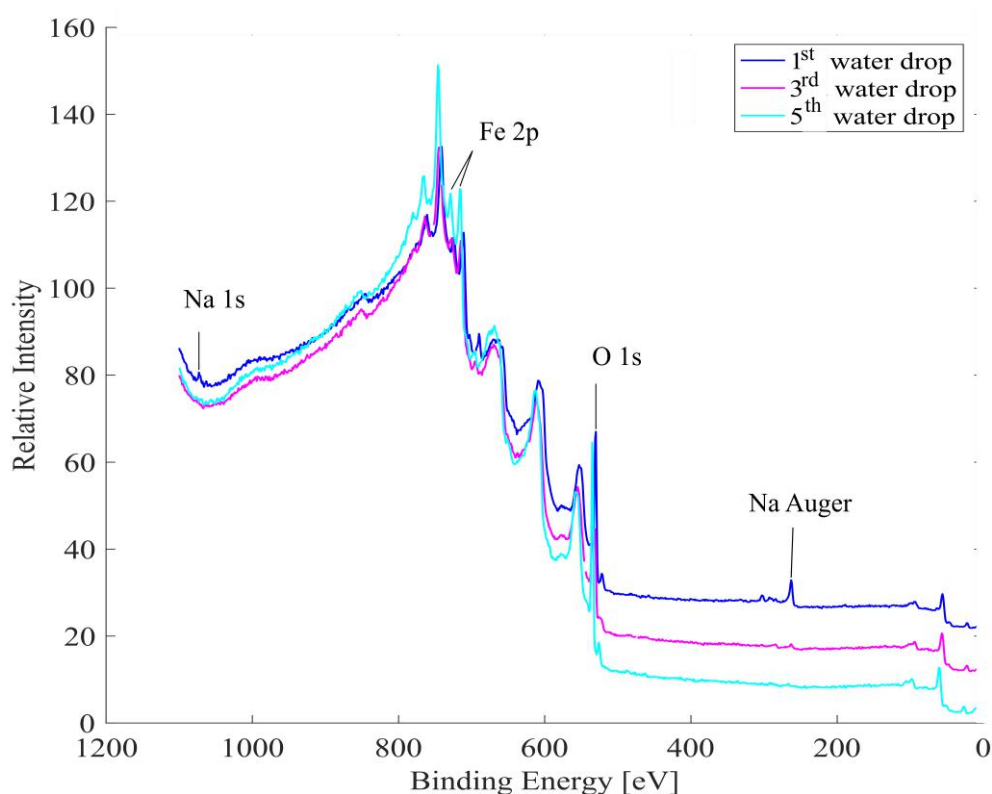


Fig. 4.6: XPS wide spectrum taken after water drop experiments on  $\text{Fe}_3\text{O}_4(001)$  using Mg anode. Graph shows wide spectra from different consecutive water drop experiments on the sample with characteristic Fe 2p and O 1s peaks as well as peaks from Na contamination labeled.

To get rid of sample contamination, it was cleaned with sputtering and annealing cycles according to procedure mentioned in subsection 4.2.2. Moreover, in between the experiments the water drop was condensed and pumped to eliminate soluble contaminations inside experimental setup. As can be seen from spectra of 3<sup>rd</sup> water drop (Fig.4.6, red color) and 5<sup>th</sup> water drop (Fig. 4.6, yellow color) the signal from

Na contamination gradually decreased until almost no signal from these peaks was detected.

Carbon is element which has to be considered regarding contaminations in the water drop experiment as it is the common contamination found on samples in UHV. For this reason the detailed spectra of C 1s were taken after each water drop experiment. These spectra are shown in Fig. 4.7. In first water drop experiment, it can be seen that two carbon signals at 288.8 eV and 284.5 eV. The signal at 284.5 eV correspond to adventitious (284.5-285.0 eV), while the 288.8 eV can assigned to carbon found in carboxyl groups. Corresponding to spectra in Fig.4.6 Na Auger line (293.0 eV) is also visible in detailed spectra of carbon . With continuous experiments and thus decreasing signal from Na contamination, the ratio of carbon in formic acid and adventitious carbon changes with almost all carbon being of carboxylic nature in 5th. water drop experiment.

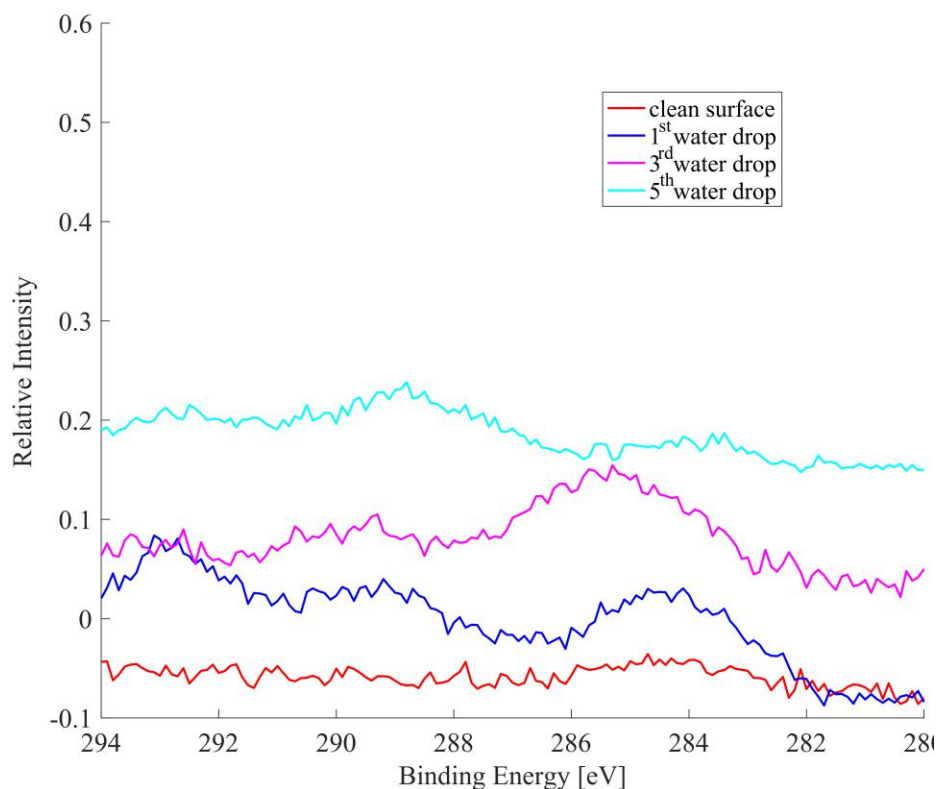


Fig. 4.7: Detailed XPS spectra of C 1s peak. Water drop experiments exhibit adventitious carbon (284.5 eV) peak and peak from carbon in carboxyl groups (288.8 eV) with lower intensity of latter in first experiment . In the first water drop experiment (blue color) there is also visible Na Auger line at 293 eV.

For examination of the liquid water interaction with oxide surface the detailed XPS spectra of O 1s were taken and they are shown in Fig.4.8. Blue spectra shows O 1s peak after water drop experiment with no Na signal detected. It can be seen

that this peak shows characteristic high binding energy shoulder compared to signal from the clean surface (red color) indicating that this signal is superposition of signal from lattice oxygen (530.1 eV) as well as hydroxyl groups (531 eV) adsorbed on the surface. Presence of this hydroxyl signal suggest that water binds to surface dissociatively, meaning that it splits hydroxyls ( $\text{OH}^-$ ) and Hydrogen ( $\text{H}^+$ ).

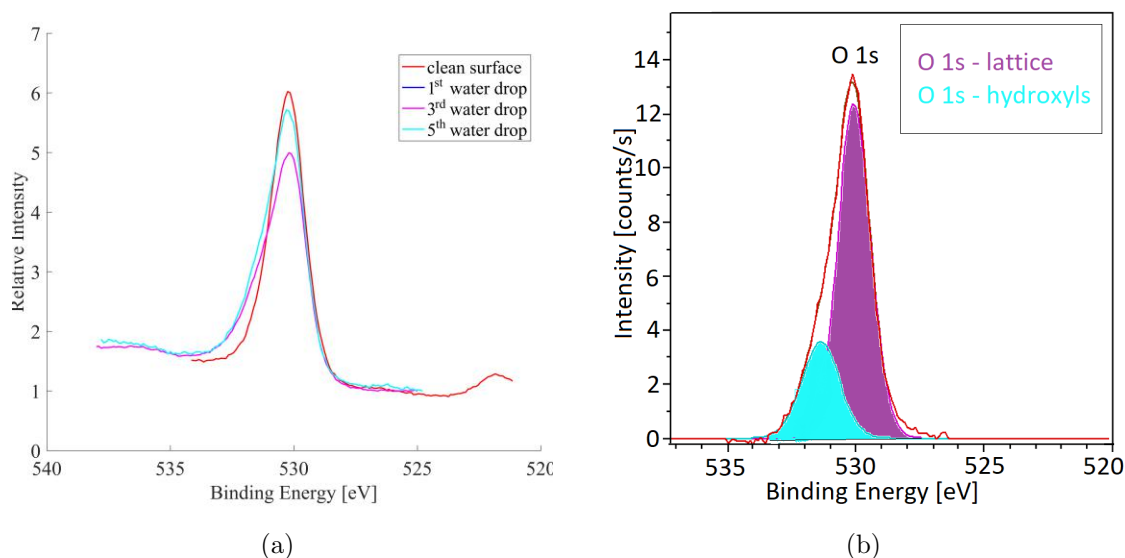


Fig. 4.8: Detailed XPS spectra of O 1s peak (a). Sample with water adsorbed on surface (blue color) indicates secondary peak at higher binding energy side compared to signal from clean surface (red color). Peak fit performed by software CasaXPS with subtracted background (b). This fit reveals secondary peak at 531 eV corresponding with adsorbed hydroxyls on the surface.

### Morphology Analysis

To inspect the morphology of the surface STM technique was employed. STM images after exposure to water are shown in Fig. 4.9. The surface is difficult to scan after the water drop experiment, but shows adsorbed atomic „chains“ on the surface. These chains exhibit preferential direction of binding, which alternates with different atomic layers (Fig. 4.10). It is also apparent that with repeating experiment the coverage of the surface with these „chains“ is increasing. To calculate the coverages of the STM images the FFT of clean surface STM image (Fig. 4.5) was performed to calculate the lattice vector of the surface. With the lattice vector known, the number of unit cells present on the surface was calculated and normalized to  $1 \times 1 \text{ nm}^2$  area. This value is then recalculated for dimensions of STM images after water drop experiments and the coverage is calculated as a ratio of atoms/molecules to number

of unit cells on the surface. These values were found to be 0.17 particles/unit cell, 0.21 particles/unit cell and 0.30 particles/unit cell respectively.

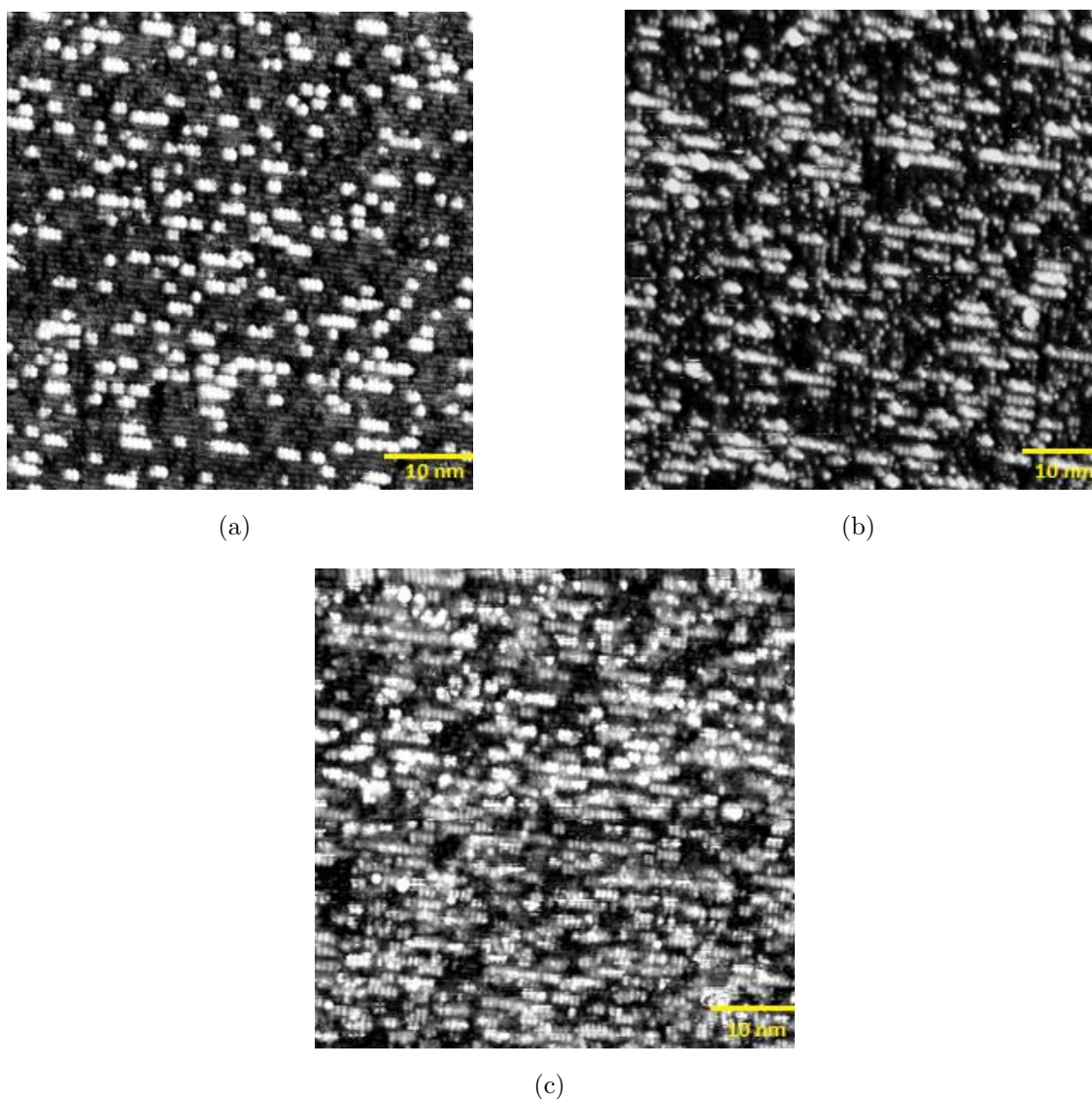


Fig. 4.9: The  $50 \times 50 \text{ nm}^2$  STM images of  $\text{Fe}_3\text{O}_4(001)$  after water drop experiments: (a) 1<sup>st</sup> water drop (1.2 V, 0.277 nA), (b) 3<sup>rd</sup> water drop (1.5 V, 0.123 nA), (c) 5<sup>th</sup> water drop (2 V, 0.169 nA).

## Discussion

Water drop experiment was tested on the  $\text{Fe}_3\text{O}_4(001)$  surface as this system is far better understood than that of  $\alpha\text{-Fe}_2\text{O}_3(012)$ . Clean surface exhibits usual „wide“ and „narrow“ sites in Fe cation rows characteristic for this surface. Moreover, this

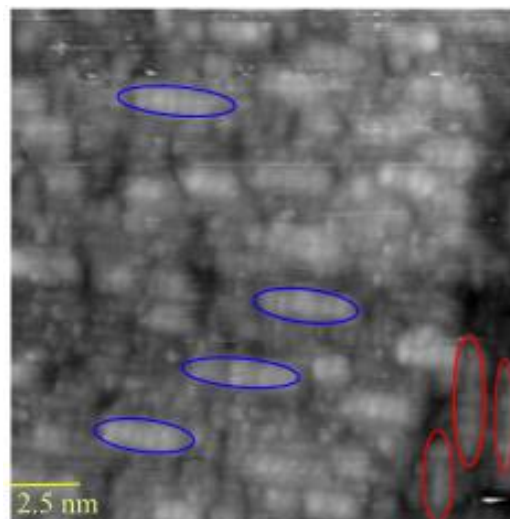


Fig. 4.10:  $12.5 \times 12.5 \text{ nm}^2$  STM image (1.625 V, 0.212 nA) of  $\text{Fe}_3\text{O}_4(001)$  after 3<sup>rd</sup>. water drop experiment. On a image two preferential directions of binding of the „chains“ are shown in red and blue ovals. These binding directions are present on different atomic layers suggesting alternating pattern similar to that of „wide“ and „narrow“ sites of clean surface.

surface also exhibits characteristic defects as wide site defects and adsorbed hydroxyls are visible in Fig. 4.5.

After water drop experiment the XPS spectra were taken in order to determine chemical composition of the surface. It can be seen that after first experiment, the surface was significantly contaminated by sodium. As Na 1s and Na Auger peaks present in Fig. 4.6. Origin of this contamination is ,however, not determined. One explanation could be provided by considering material of glass vial, were liquid water is stored . This material is pyrex glass, which contains volatile sodium oxide. This oxide could be evaporated during bake-out of the experimental chamber and adsorbed on the inner surfaces during cooling down. It is possible that during experiment this oxide was „washed off“ by condensed water and transported onto the sample.

With Na contamination being removed by repetitive „washing off“, attention was shifted towards carbon as common contamination on the single crystal oxide surface. There are two carbon signals present in detailed XPS spectra in Fig. 4.7 adventitious at 284.5 eV and secondary peak. With Na contamination still present on the sample the adventitious signal dominates, but is overcome by 288.8 eV signal in 5<sup>th</sup> experiment with no Na contamination detected on the sample. Explanation for these carbon signals might come from adsorption of organic acids from residual atmosphere present in load-lock chamber. The adventitious signal at 284.5 eV might

come from carbon-carbon bond in acetate<sup>1</sup>, whereas the carboxyl signal at 288.8 eV might come from double carbon-oxygen bond in formate<sup>2</sup>.

Studying STM images show interesting, yet unexplained structure. It is apparent that after water drop experiments atomic/molecular „chains“ form on the surface. Molecules/atoms in these chains bind in one preferential direction, which seems to be alternating with each atomic layer (Fig. 4.10). This would suggest that these particles binds to Fe sites, but as the clean surface underneath couldn't be resolved, this hypothesis cannot be confirmed. One possibility is that structures being Na atoms bound to surface. This doesn't correspond with XPS measurement, where the intensity of Na signal decreases while coverage of these structures seems to be increasing. Another possibility is that these „chains“ are adsorbed hydroxyls from water drop experiment. XPS analysis of the oxygen, however doesn't show any differences with amount of adsorbed hydroxyls, which would correspond to increased number of chains with later experiments. Third possibility is to consider said structures to be adsorbed salts of organic acids considering carbon signal from XPS. Carboxylic carbon (288.8 eV) corresponds to adsorbed formate. These molecules could correspond to the „chains“ in STM image while the adsorbed layer underneath could be assigned to dissociated water from the water drop. XPS measurement shows that in 5<sup>th</sup> water drop experiment the majority of carbon species on the sample display carbon signal at 288.8 eV, which would correspond with the large coverage of the chains in STM image. From the O 1s detailed spectrum no conclusion can be derived as the peaks of hydroxyls and formate have similar binding energy at 531 eV.

### 4.3 Possible improvements of the Experimental setup

As this work deals with initial development of condensation liquid water doser, there are some improvements that can be implemented in design to further improve its functionality and overall purity of the experiment.

Outer body of the cold finger mentioned in 3.2.1 is made out of stainless steel AISI 304, due to availability and relatively easy machining. For better chemical stability one could consider usage of stainless steel AISI 316. This would however involve higher price of the material and more difficult machining of the parts. Worth a consideration are also protective coatings like Gold, which provide the best chemical stability. On the other hand this would require galvanic coating of the drop maker which doesn't guarantee uniformity of gold layer and can lead to same results

---

<sup>1</sup>Salt formed from acetic acid ( $C_2H_3O_2$ )

<sup>2</sup>Salt formed from formic acid HCOOH

achieved with stainless steel. To get better control over size of the water droplets in experiment, cold finger can be redesigned with sharper tip at the bottom. This would allow smaller droplet to form and thus get better control over the volume of liquid in setup by temperature and time of water vapor exposure adjustments.

To improve the vacuum insulation (subsection 3.2.4) and to limit possible leaks of liquid nitrogen into insulation parts one could simply use stronger springs.

As mentioned in section 4.2, contamination of the sample in the experiment might be caused by elevated pressures during the transfer. The solution to this problem is to implement custom designed liquid nitrogen cooled absorption pump (subsection 3.3.3) attached to a CF40 T-tube between the liquid water dosing setup and the load-lock. High surface area cooled by liquid nitrogen provide sufficient pumping for remaining water vapors as well as other elements present in load-lock. This leads to lower pressure and cleaner transfer of the samples from the main chamber into liquid water dosing setup.

## 4.4 Design Summary

In this chapter the design of new condensation liquid water dosing device is described. Its principle lies in dosing water vapor onto liquid nitrogen cooled drop-maker, where it freezes and forms a layer of ice with sufficiently low vapor pressure, to transfer sample under conditions of ultrahigh vacuum. Water then melts and drops on the sample in closed volume under saturation vapor pressure of  $H_2O$ . Liquid and vapors are then pumped with liquid nitrogen-sorption pump and sample is transferred again at low pressure into main chamber for analysis.

Liquid water dosing setup is designed to be UHV compatible, using materials like stainless steel, copper, pyrex glass and viton. Chamber for liquid water dosing is designed to provide small surface area and volume, which increases the pumping speed of residual water vapors after dosing. Hexagonal shape of the chamber provides possibility to mount it directly onto the gate valve, eliminating the need of connection via CF „nipple“ and thus reducing the surface area and volume for increased pumping speed. Sample holder consists of two customized stainless steel blocks fixed to the back wall of the chamber by threaded rods. Rotational movement of the holder is eliminated by its height, which is produced with „tight fit“ tolerances.

Condensation liquid water dosing device cold finger works on principle of a flow cryostat. Liquid nitrogen is introduced through thin capillary that leads into small reservoir at the tip. From there, it is pumped through the concentric exhaust tube and out of the cold finger. Flow of the liquid nitrogen provides sufficient cooling power to cool the tip to low temperatures. To create sharp interface between ice

layer and the stainless steel on the cold finger, narrow temperature gradient had to be achieved. This is done by combining thin walled stainless steel cylinder to provide poor thermal conductance and counter heating on one side to endless reservoir of the heat. In order to achieve the most effective combinations of cooling/heating power, the cold finger was designed with rough vacuum insulation to limit heat transfer via convection. Proper sealing of all parts in drop maker is ensured by series of the O-rings as well as pressing springs to ensure vacuum seal of lower parts.

For proper functioning of cold finger preparation and operating procedure must be followed. Without following procedural steps operational problems were observed, which may lead into malfunctioning or damage to the experimental setup. One of the common problem that occurs is that liquid nitrogen starts to leak into insulation, which then affects the intended ice-stainless steel interface. Moreover it might also destabilize the counter heating of the drop maker controlled by PID regulator, leading to oscillation of the system and eventually to damage electrical or other components. Other functional problem might be congestion of the liquid nitrogen flow line. It can occur when the solid particles get into thin capillary and block the flow of the nitrogen. Commonly these particles consist of ice from the remaining humidity in drop maker or pieces of ice in liquid nitrogen supply. This can be determined by drop in a pressure in scroll pump with values under 15 mbar. To prevent this it is important to always have particle filter present at top of cold finger and to heat upper part of drop maker in between cooling processes to get rid of ice particles on the top.



## 5 $\alpha$ -Fe<sub>2</sub>O<sub>3</sub> (012) SURFACE INTERACTION WITH H<sub>2</sub>O

Water is common in residual gas and it is already known that the (012) surface dissociates water and adsorbs it at room temperature [50]. In this experiment performed at TU Vienna in Omega chamber, the effects of three different exposures were investigated. Firstly, the lowest exposure of 50 Langmuir (L) was performed by dosing water vapor ( $\approx 10^{-8}$  mbar) through the leak valve directly in UHV system for 666 s. High pressure experiment (18 mbar) of water vapor was performed in experimental setup for water drop experiment with water in container with temperature 16°C. Once the sample was in experimental setup, the valve to water container was opened and water evaporated into setup. After the exposure, the water vapor was pumped by cryo-sorption pump and sample was transferred back into analysis chamber. Lastly, the water drop experiment was performed according to procedure mentioned in section 4.1.

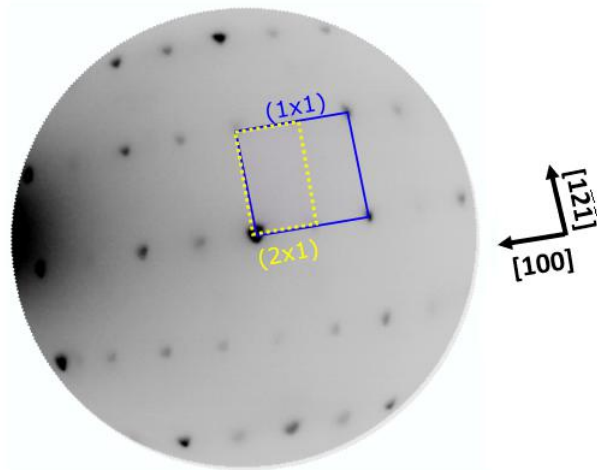
### 5.1 Sample Preparation

The natural crystal sample was purchased from SurfaceNet, with a nominal precision of  $\pm 0.1^\circ$ . Initial cleaning cycles upon sample insertion into UHV system were performed sputtering with 1 kV Ar<sup>+</sup> ions and annealing in UHV, which successfully removed all contaminants detectable by XPS from the sample (Al, Si, P, S, Cl, K, Ca or Ti, which were reported in [9]). After this preliminary preparation in UHV, the sample was analyzed by LEED and showed a weak (1×1) diffraction pattern. With a beam energy below 120 eV, the sample was charging, which was observed as a complete distortion of the LEED pattern. This is a result of poor conductivity of the crystal, which proves an inability to perform STM measurements on this sample. Usually, samples shouldn't exhibit charging effect in LEED below 20 eV in order to perform successful STM measurement. This requires 60-100 cycles of sputtering with 1 kV Ar<sup>+</sup> ion sputtering and annealing in UHV (T=630°C) to partially reduce the bulk and thus promote the conductivity [8]. Moreover, to prevent the surface from being reduced to Fe<sub>3</sub>O<sub>4</sub>, every 5-10 annealing cycle must be done in oxygen ( $p_{O_2} = 1 \times 10^{-6}$  mbar, T=400°C).

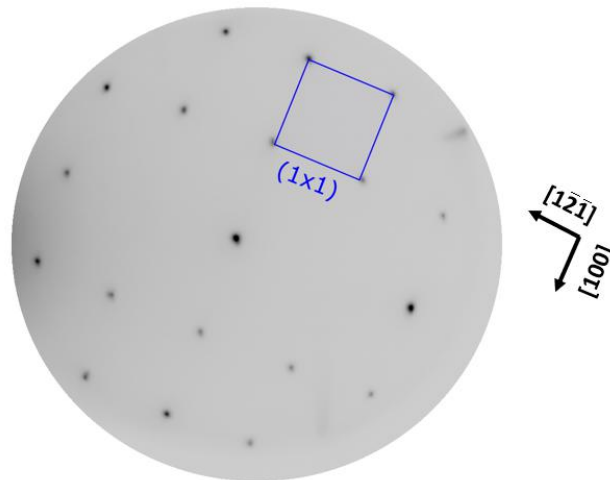
After initial cleaning procedure of the sample, the (2×1) reconstruction (Fig. 5.1(a)) could be prepared either after sputtering or directly from the (1×1) surface by annealing in UHV (T=500°C<sup>1</sup>). In the same way, the (1×1) surface (Fig. 5.1(b)) could be prepared from a freshly sputtered crystal or from the (2×1) termination

<sup>1</sup>Temperature measured by K-type thermocouple on the manipulator in the chamber

by annealing in oxygen ( $p_{\text{O}_2}=1\times 10^{-6}$  mbar,  $T=480^\circ\text{C}$ ). The surfaces were kept clean by occasional sputtering with 1.5 kV  $\text{Ar}^+$  ions ( TU Vienna Omega chamber:  $p_{\text{Ar}}=1.5\times 10^{-6}$  mbar,  $I=0.4\text{-}0.5\ \mu\text{A}$ , CEITEC preparation chamber:  $p_{\text{Ar}}=1.0\times 10^{-6}$  mbar,  $I_{\text{emission}}=10$  mA (wide beam)).



(a)



(b)

Fig. 5.1: Diffraction pattern of  $\alpha\text{-Fe}_2\text{O}_3$  (012) acquired in LEEM. (a) Diffraction pattern of  $(2\times 1)$  surface reconstruction at 40 eV. (b) Diffraction pattern of  $(1\times 1)$  surface reconstruction at 40 eV. Missing diffraction spots in pattern are result of glide plane along the  $[1\bar{2}1]$  direction. Dark cloud on left side represent secondary electrons emitted from the surface.

## 5.2 (1×1) Surface Reconstruction

The oxidized (1×1) reconstructed surface has been imaged by STM (Fig. 5.2) in work of Kraushofer [51]. Images acquired with positive and negative bias (the empty and filled states images) show distinctive zig-zag line pattern. The measured unit cell dimensions correspond to dimensions of the bulk terminated unit cell  $5.0 \times 5.4 \text{ \AA}^2$ .

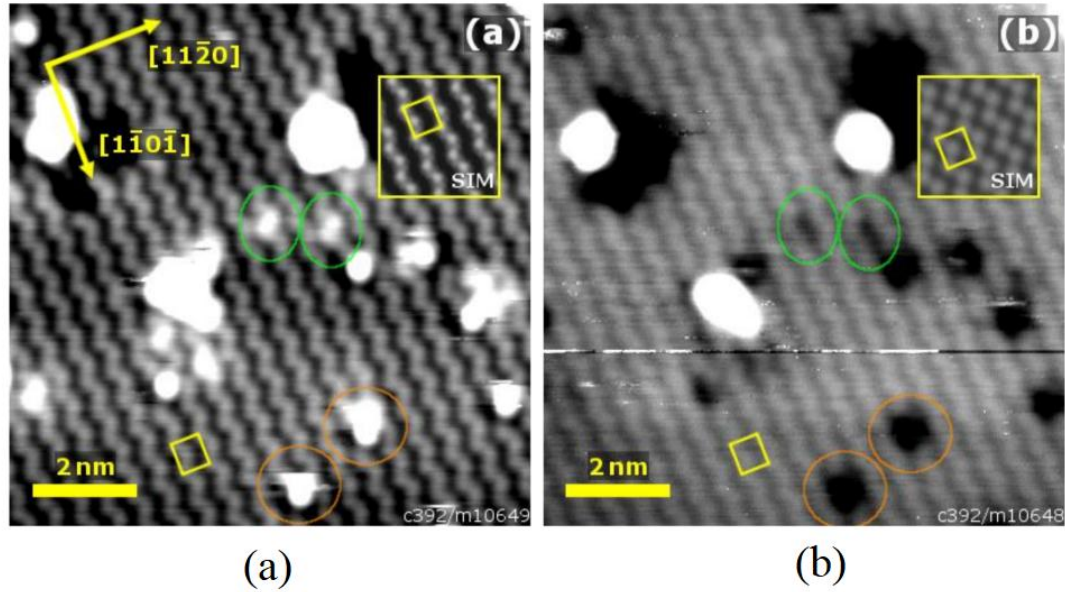


Fig. 5.2: STM images of the  $\alpha$ -Fe<sub>2</sub>O<sub>3</sub>(012)-(1×1) surface imaging (a) filled states ( $10 \times 10 \text{ nm}^2$ ,  $U_{\text{sample}} = -3 \text{ V}$ ,  $I_{\text{tunnel}} = 0.1 \text{ nA}$ ) and (b) empty states ( $10 \times 10 \text{ nm}^2$ ,  $U_{\text{sample}} = +3 \text{ V}$ ,  $I_{\text{tunnel}} = 0.1 \text{ nA}$ ). Both images were acquired on the same sample area, and exhibit zig-zag rows of bright protrusions running in the [100] direction. Picture reprinted from [51].

The drop of ultra pure Milli-Q water was placed on top of the sample using the Cold finger drop maker setup. The LEED analysis (Fig. 5.3) of the sample after this treatment shows that surface reconstruction is not lifted and surface still exhibits (1×1) reconstruction of oxidized surface.

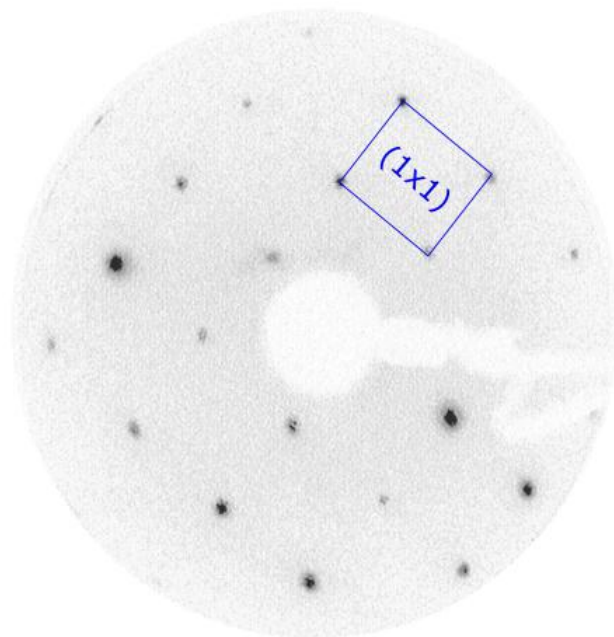


Fig. 5.3: LEED pattern of  $(1\times 1)$  surface reconstruction after exposure to liquid water.

Cleanliness of performed experiment was again studied by inspecting detailed XPS spectrum of carbon C 1s. This spectrum is shown in Fig. 5.4. It can be seen that there is only a little increase in carbon contamination in water drop and high pressure water vapor experiment, which might be connected with transfer of the samples through the load-lock of the chamber.

It has been previously reported, that dissociated water binds strongly to the  $(1\times 1)$  surface [50]. XPS spectra of the O 1s region after low pressure (50 L), high pressure (18 mbar) water vapor and liquid water have been dosed on the  $(1\times 1)$  surface are shown in Fig. 5.5. Red spectra shows O 1s peak of the clean surface with no water dosed. Spectra of 50 L, 18 mbar and liquid water dosing are shown in blue, purple and green, respectively. It can be seen that these peaks exhibit similar shape with characteristic high binding energy shoulder. After performing fit (Fig. 5.6), the spectra show that they consist of signals from lattice oxygen (530.11 eV) as well as peaks at 531.4 eV and 532.4 eV. Performing this fit reveals that the area of secondary peaks are roughly  $(50 \pm 4)\%$  with respect to each other.

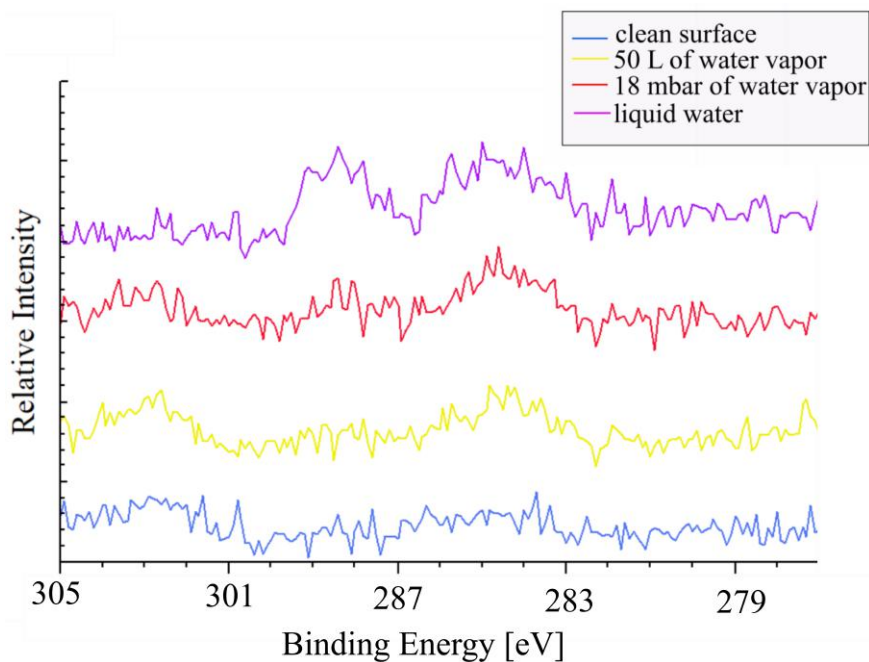


Fig. 5.4: Detailed XPS spectra of C 1s peak. Water drop and dosing experiments exhibit minimal carbon contamination with signal from adventitious (284.5 eV) and carbon in carboxylic acid (288.8 eV).

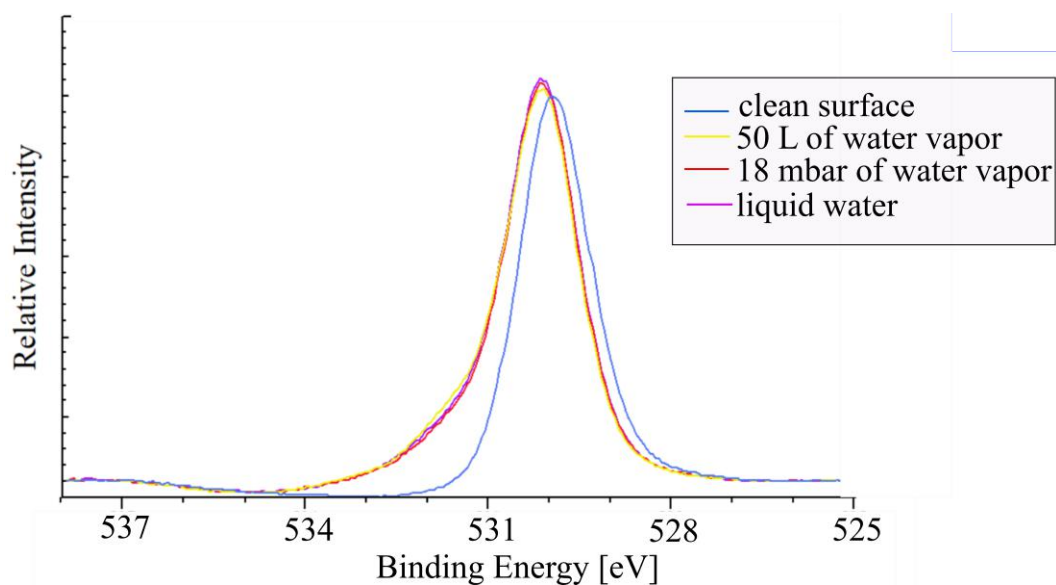


Fig. 5.5: Detailed XPS spectra of O 1s peak. All the experiment with water exhibit similar asymmetry at higher binding energy suggesting similar binding of the H<sub>2</sub>O to the surface with different exposures of surface.

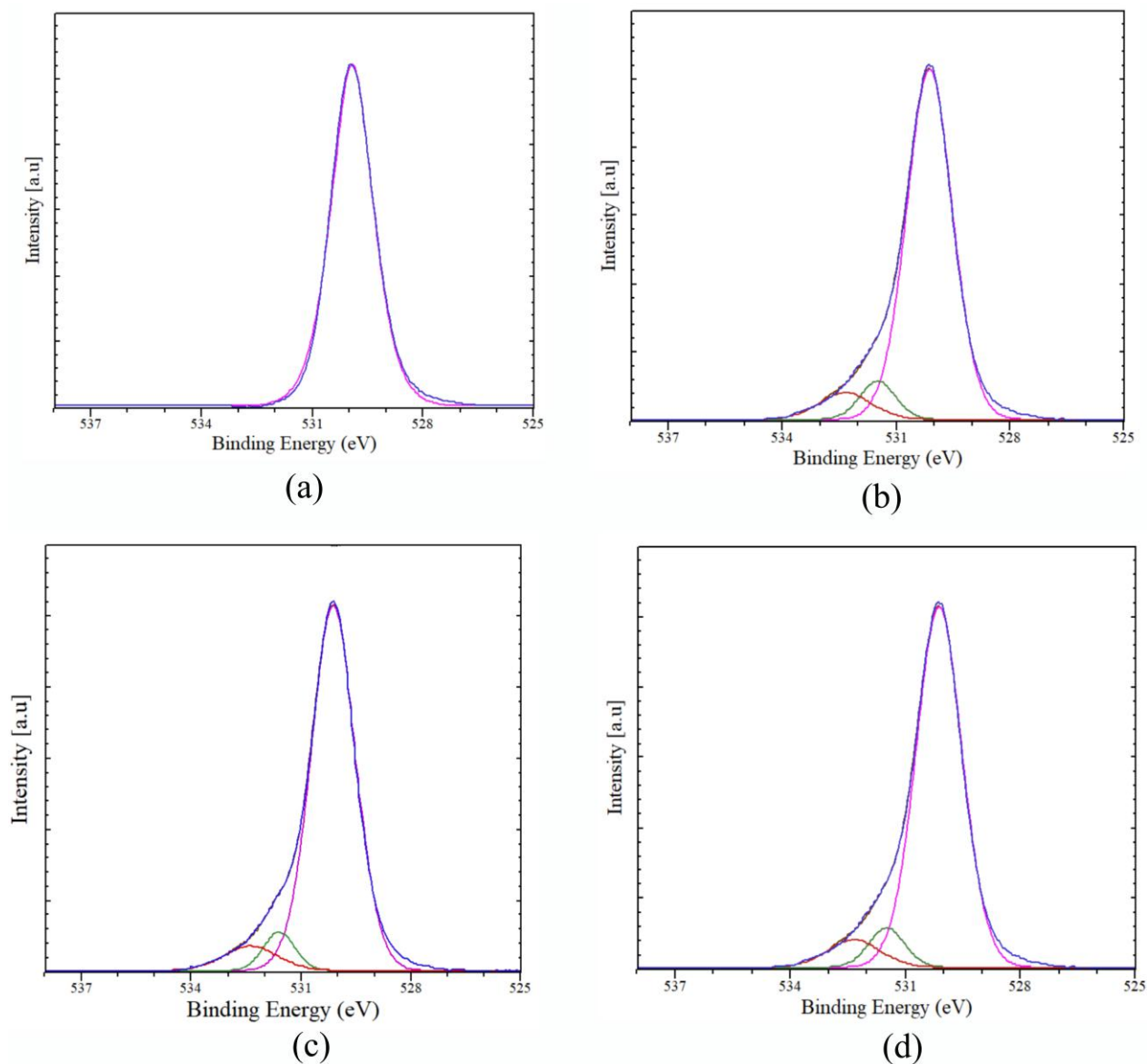


Fig. 5.6: Detailed XPS spectra of O 1s after normalization with performed fit of the signal. Signal exhibits peaks at 530.11 eV (lattice oxygen - purple), 531.41 eV (hydroxyls - green) and 532.40 eV (undetermined species - red) (a) Signal of the clean surface. (b) Oxygen signal after 50 L dosage of water vapor. (c) Oxygen signal after 18 mbar water vapor exposure. (d) Oxygen signal after liquid water drop experiment.

### 5.2.1 Surface Oxygen Exchange

An interesting phenomena has been observed on  $\alpha$ -Fe<sub>2</sub>O<sub>3</sub>(012) surface showing intermixing of lattice oxygen present on the surface and the oxygen present in adsorbed water on the surface. The experiment was carried out by preparing (1×1) surface reconstruction with oxygen isotope on the surface. After achieving labeled surface water drop experiment was performed and sample was returned to analysis chamber.

Before the analysis, the sample was heated to 200°C in order to desorb water from the surface and to analyze the sample by LEIS.

To perform this experiment pure oxygen gas was introduced into chamber with labeled O<sub>2</sub><sup>2</sup>. Goal was to prepare (1×1) surface reconstruction with only <sup>18</sup>O present on the surface. In Fig.5.7 the LEIS spectrum of  $\alpha$ -Fe<sub>2</sub>O<sub>3</sub>(012) is shown. Red spectra shows clean surface with only <sup>16</sup>O (505 eV) and Fe (955 eV) present. Blue spectra are taken after first cycle with annealing in <sup>18</sup>O ( $5 \times 10^{-7}$  mbar) at 480°C. It can be seen that this spectrum exhibits additional peak at 559 eV attributed to mentioned <sup>18</sup>O. At this point the ratio of the height of the peaks of <sup>16</sup>O to <sup>18</sup>O was roughly 4:3. This ratio remained constant for several additional cycles, so it was decided to decrease annealing temperature to 350°C and continue with oxidizing process. The purple spectra shows the surface after 14<sup>th</sup>. oxidizing cycle in <sup>18</sup>O<sub>2</sub>. The peak ratio of <sup>16</sup>O to <sup>18</sup>O was established to be roughly 2:4 and at this point it was decided to carry on with the water drop experiment.

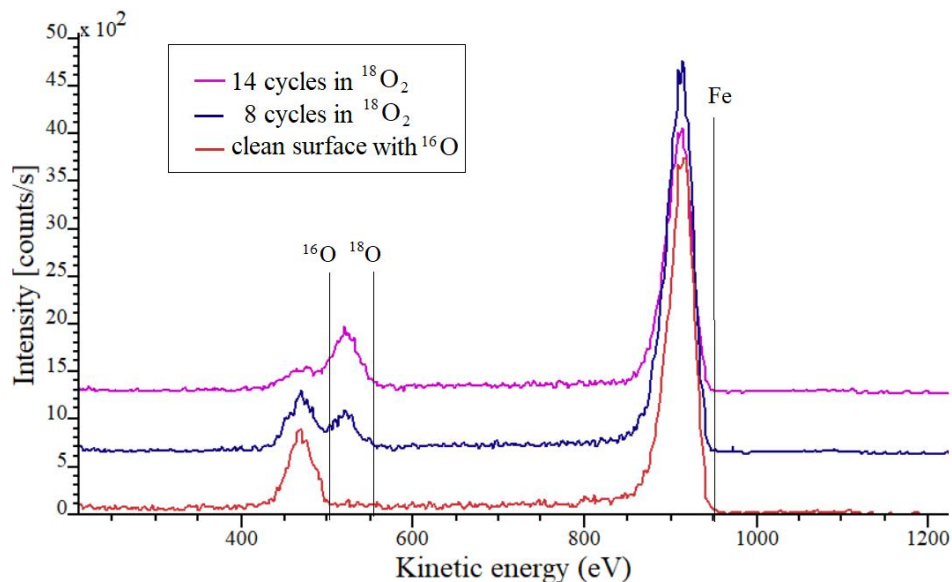


Fig. 5.7: LEIS/ISS spectra of „labeling“ the surface with <sup>18</sup>O. In red there is the spectrum of clean surface with only <sup>16</sup>O. After eight cycles in <sup>18</sup>O the surface exhibits both <sup>16</sup>O and <sup>18</sup>O. After fourteen cycles the two oxygen signals are still visible with higher <sup>18</sup>O peak.

After the water drop experiment, the sample was transferred back into analysis chamber, where it was heated up to 200°C to desorb all the water on the surface and it was again analyzed by LEIS. The LEIS spectra after the experiment are shown in Fig. 5.8. It is clearly visible that the signal from <sup>16</sup>O (505 eV) increased

<sup>2</sup>Labeled oxygen in meaning of oxygen isotope with atomic number  $N = 18$  (<sup>18</sup>O) instead of standard <sup>16</sup>O.

and is comparable to one from  $^{18}\text{O}$  (559 eV). This suggests that some interchange mechanism between lattice oxygen and oxygen contained in water is taking place during water adsorption on this surface.

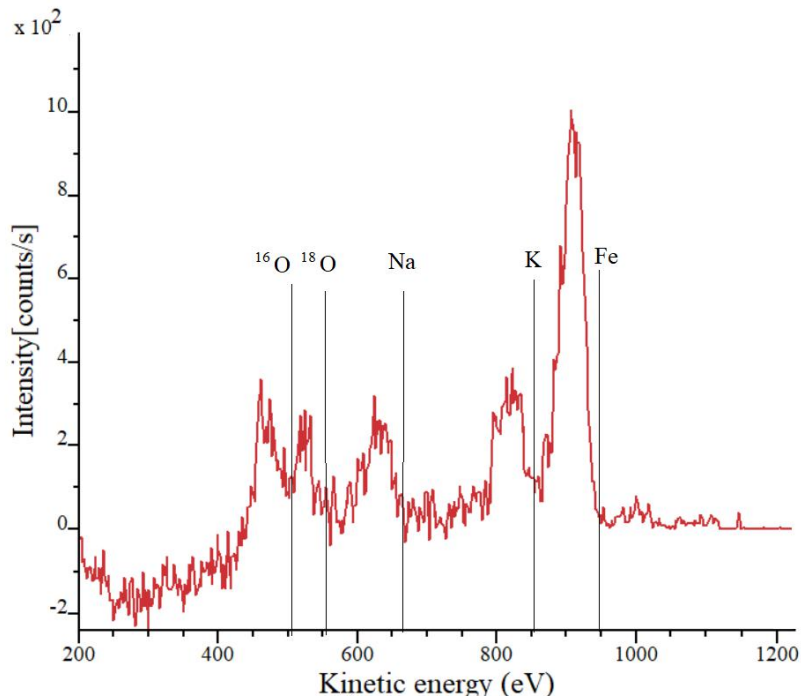


Fig. 5.8: LEIS/ISS spectra of the surface after the experiment. The spectrum exhibits higher signal from  $^{16}\text{O}$ , suggesting exchange of the oxygen between lattice and adsorbed water. This spectrum, however, exhibits also peaks from the Na and K contamination making the experiment inconclusive.

Unfortunately this experiment was burdened by the contaminations, which again appeared in water drop experiment as can be seen in Fig. 5.8. This spectrum contains signals of Na (666 eV) and K (858 eV) as well as signals of both isotopes of oxygen and signal from lattice Fe.

### 5.3 $(2\times 1)$ Surface Reconstruction

The reduced  $(2\times 1)$  phase was again imaged by STM in work of Kraushofer [51] (Fig. 5.9). He shows that this periodicity is caused by paired rows of atoms in the  $[1\bar{2}\bar{1}]$  direction, with a phase shift of every other row and a more pronounced gap between each pair. The unit cell is twice as wide as on the  $(1\times 1)$  surface, which was the expected result.

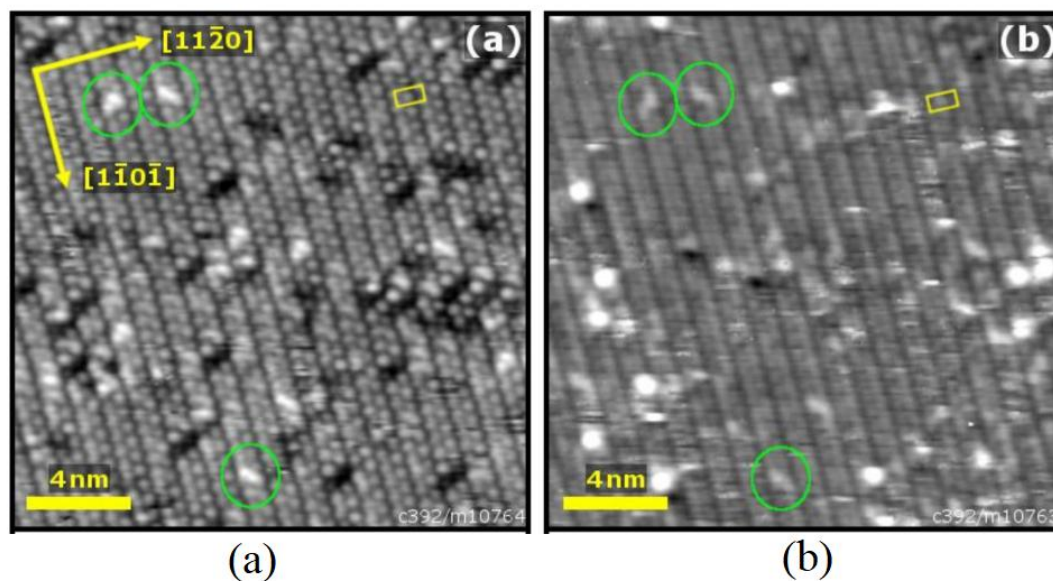


Fig. 5.9: STM images of the  $\alpha$ -Fe<sub>2</sub>O<sub>3</sub>(1102)-(2×1) surface in (a) filled states ( $20 \times 20 \text{ nm}^2$ ,  $U_{\text{sample}} = -2.5 \text{ V}$ ,  $I_{\text{tunnel}} = 0.1 \text{ nA}$ ) and (b) empty states ( $20 \times 20 \text{ nm}^2$ ,  $U_{\text{sample}} = +2.5 \text{ V}$ ,  $I_{\text{tunnel}} = 0.1 \text{ nA}$ ), recorded over the same sample area. The bright protrusions form zig-zag lines, with a pronounced gap between each zigzag. Picture reprinted from [51].

From the LEED measurement of the surface structure of the  $\alpha$ -Fe<sub>2</sub>O<sub>3</sub>(012), it seems that liquid water lifts the surface reconstruction to (1×1) periodicity as is shown in Fig.5.10 (a). This water induced reconstruction seems to be stable during heating of the sample up to 320°C, where the faint half-order spots start to appear at low energies of electron beam (40 eV) (Fig. 5.10 (b)). Experiment involving dosage of 20 L seems not to lift reconstruction as the surface still exhibits (2×1) surface reconstruction with slightly diffused diffraction spots (Fig. 5.10 (c)). Fig. 5.10(d) shows diffraction pattern after several minutes of exposure to electron beam. Diffraction pattern displays characteristics of (1×1) surface reconstruction with some blurred half-order spots present.

As in section 5.2 the detailed spectrum of C 1s was measured (Fig. 5.11). Clean surface (red color) exhibits little carbon signal with slight increase in adventitious carbon after dosing 20 L of water vapor (blue spectra) into UHV system. With high pressure water vapor experiment of 18 mbar the signal of carbon from carboxyl species starts to appear. This signal is even more pronounced in experiment with liquid water, where it comprises the majority of carbon signal from sample surface.

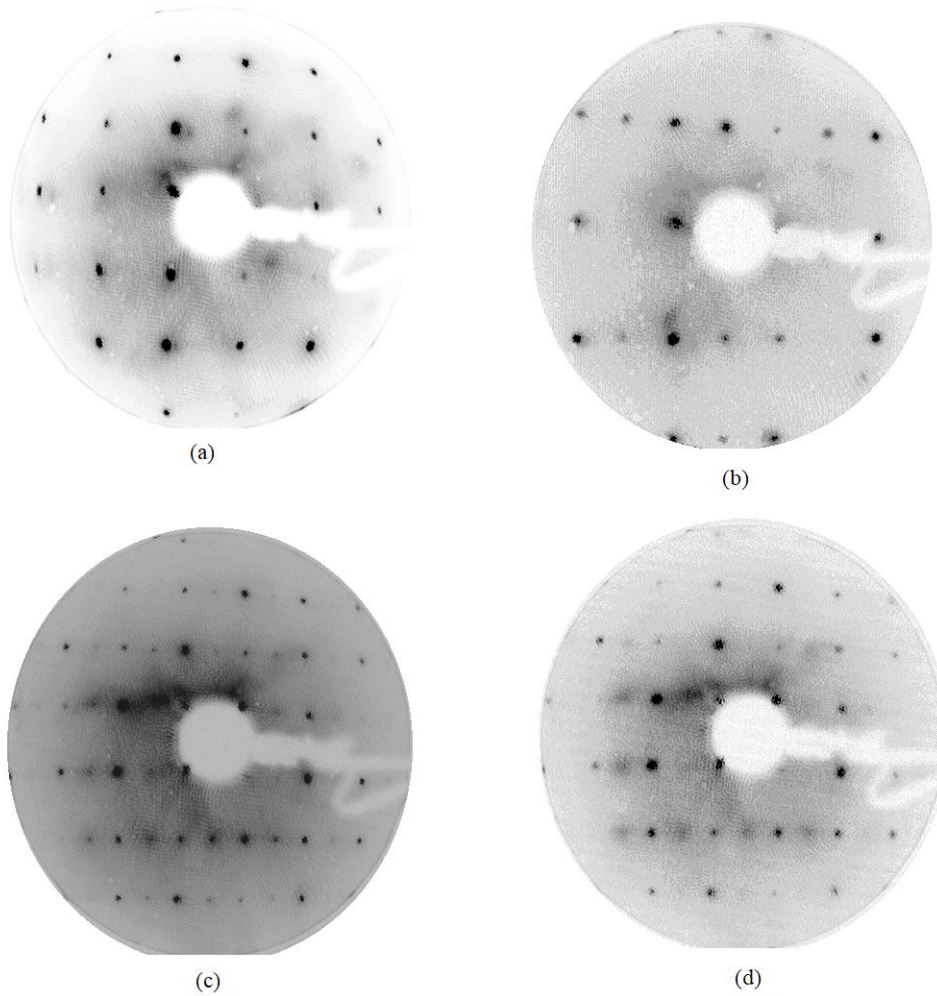


Fig. 5.10: LEED pattern of  $(2\times 1)$  surface after exposure to liquid and gaseous water. (a) LEED pattern (90 eV) after exposure to liquid water with sample at  $60^\circ\text{C}$ . Surface exhibits lifted  $(2\times 1)$  into  $(1\times 1)$  surface reconstruction. (b) LEED pattern (40 eV) after exposure to liquid water with sample at  $320^\circ\text{C}$ . Pattern correspond to that of mixed surface with some  $(2\times 1)$  visible. (c) LEED pattern of  $(2\times 1)$  surface after dosage of 20 L of water vapor. Surface still exhibits  $(2\times 1)$  periodicity with lower intensity of half-order spots. (d) LEED pattern of  $(2\times 1)$  surface after dosage of 20 L of water vapor after several minutes of exposure to e-beam. Half-order spots are barely visible and display diffused character.

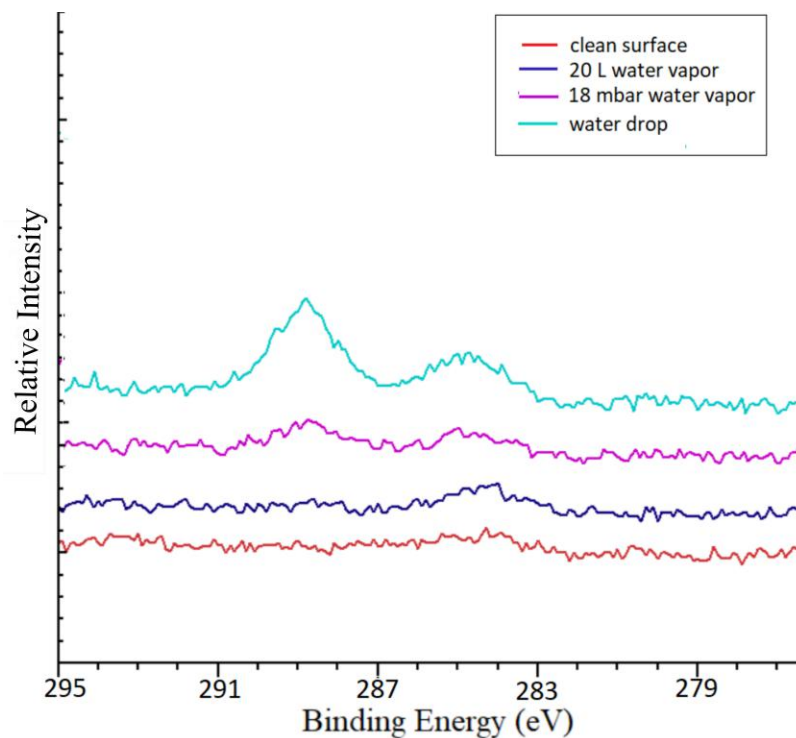


Fig. 5.11: Detailed XPS spectra of C 1s peak. Exposure to low pressure of water vapor (blue spectrum) causes only minimal contamination from adventitious carbon (284.5 eV). Exposure to 18 mbar (purple spectrum) causes slight increase in both adventitious (284.5 eV) and carboxylic (288.8 eV) carbon. After water drop (cyan spectrum) the signal of carbon increased with larger peak at 288.8 eV.

Again XPS spectra of the O 1s region after different low pressure (20 L), high pressure (18 mbar) water vapor and liquid water have been dosed on the (2×1) surface are shown in Fig. 5.12 with main peak of lattice oxygen at 530.11 eV. It can be seen that these peaks exhibit similar shape with characteristic high binding energy shoulder. Performing the fit of the data reveals that one secondary peak at 531.41 eV is present with 13.7% of area of the detected signal after dosing 20 L of water vapor. After exposing surface to 18 mbar of water vapor in the cold finger setup third peak arises at 532.4 eV with 2.9% with respect to detected signal (17.6% area with respect to 531.41 eV peak). With surface exposed to liquid water, the signal of peak at 532.4 eV further increased with area of 8.7% with respect to detected signal and 43.4% with respect to signal at 531.41 eV.

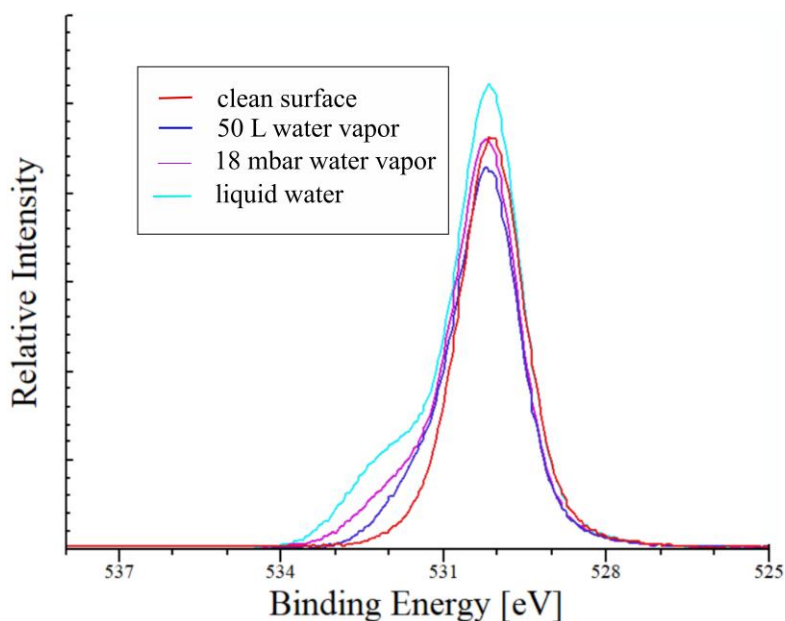


Fig. 5.12: Detailed XPS spectra of O 1s after normalization with performed fit of the signal. Signal exhibits peaks at 530.11 eV (lattice oxygen - purple), 531.41 eV (hydroxyls - green) and 532.40 eV (undetermined species - red). (a) Shows the spectrum of clean surface with peak corresponding to lattice oxygen. (b) Detailed spectrum of O 1s after exposure to 20 L of water vapor. From fitting the spectra it can be seen that the signal consists of two peaks. (c) Detailed spectrum of O 1s after exposure to 18 mbar of water vapor. This signal exhibits the third peak present on the surface. (d) Detailed spectrum of O 1s after water drop experiment exhibiting roughly same peak-to-peak ratio of the second and the third peak.

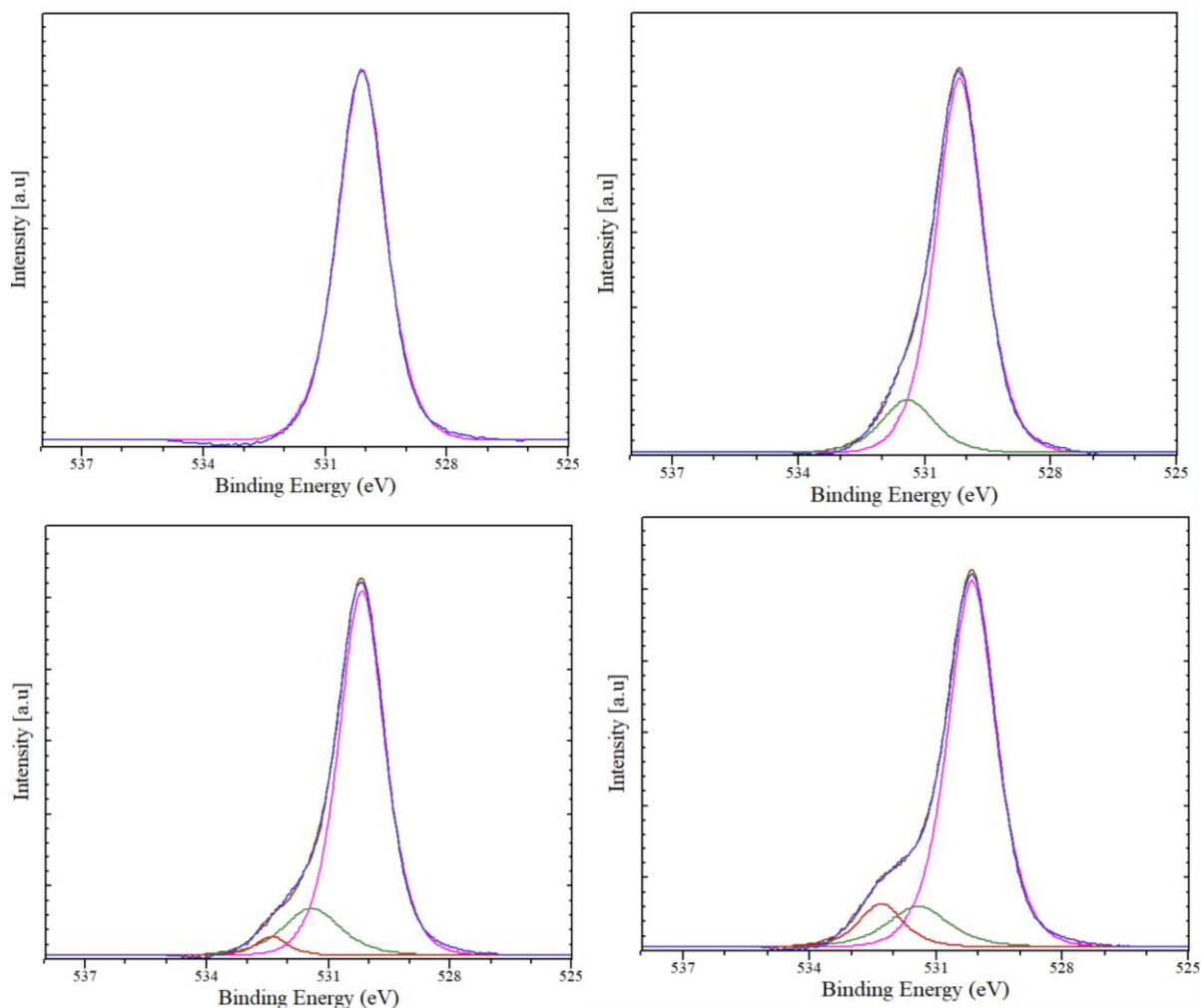


Fig. 5.13: Detailed XPS spectra of O 1s after normalization with performed fit of the signal. Signal exhibits peaks at 530.11 eV (lattice oxygen - purple), 531.41 eV (hydroxyls - green) and 532.40 eV (undetermined species - red) (a) Signal of the clean surface. (b) Oxygen signal after 50 L dosage of water vapor. (c) Oxygen signal after 18 mbar water vapor exposure. (d) Oxygen signal after liquid water drop experiment.

## 5.4 Discussion

Water drop experiment was performed on the  $\alpha$ -Fe<sub>2</sub>O<sub>3</sub>(012) surface in order to determine its interaction mechanism of liquid and gaseous water. Clean surface was prepared according to standard procedure in agreement with [8, 50, 51]. This procedure yielded either (2×1) surface reconstruction after reducing surface in UHV or (1×1) after oxidization with diffraction pattern with sharp spots.

After the exposure to the water the (1×1) surface reconstruction survives both the high pressure environment and contact with liquid water. This suggests that long range ordering of adsorbed water and hydroxyl groups is a minor effect com-

pared with the adsorbate–substrate interaction which favors adoption of periodicity of substrate and is in agreement with results obtained in [9]. Yet, the effect of water on  $(2\times 1)$  differ. Henderson [9] claims that reconstruction is also not lifted even in this case. While somewhat true that at low pressure dosing experiment (20 L) the  $(2\times 1)$  is not lifted with slight blurring of half-order spots. With prolonged exposure of this surface to an electron beam from LEED, the change to  $(1\times 1)$  surface reconstruction appears to happen as the similar effect was observed in [7]. It seems that some sort of beam induced surface reordering happens, but clear explanation is yet to be provided. After exposing the  $(2\times 1)$  to high pressure (18 mbar) vapor and liquid water, this reconstruction appears to be lifted into  $(1\times 1)$ . It has to be noted that LEED in case of high pressure vapor experiment was measured after XPS measurement, so effect of surface transformation induced by X-ray irradiation cannot be fully excluded. In liquid drop experiment the  $(2\times 1)$  reconstruction appeared to be fully lifted into  $(1\times 1)$  and this reconstruction appears to be stable up to  $320^\circ\text{C}$ , when the half-order spots start to appear at 40 eV energy of e-beam.

The XPS measurement was focused on detailed spectra of O 1s and C 1s. On both surface reconstructions the oxygen signal was found to be composed of three peaks after high pressure and liquid drop experiment. These peaks can be found at 530.1 eV attributed to lattice oxygen and 531.4 eV and 532.4 eV of secondary peaks. While it would be rational to assume that these peaks are attributed to adsorbed hydroxyl groups and molecular water adsorbed on the surface, these peaks need to undergo careful evaluation. In study of same system [8], it has been reported, although not explicitly stated, that binding energy for hydroxyl groups is at 531.5 eV in agreement with 531.4 eV detected peak in this experiment. On the other hand, the peak attributed to molecular water was reported to be at around 533.5 eV, which is 1.1 eV difference from the position of the peak measured in this experiment. In work of Knipe [63] studying water adsorption of iron sulfides, the peak at 532.4 eV is attributed to molecular water bound to already adsorbed hydroxyl.

Second interpretation of XPS measurements comes from studying detailed spectra of C 1s. This signal consists of two peaks at 284.5 eV and 288.8 eV that can be attributed to adventitious and carbon in carboxyl groups signal respectively. Signal at 288.8 eV could be attributed to adsorbed formic acid, which would correspond to results obtained in study of adsorption of formic acid on  $\text{TiO}_2$  (110) and (441) in [64]. Oxygen signal at 532.4 eV assigned again to adsorbed formic acid would also correspond to one measured in this experiment. In study of titanate nanotubes [65], the measured peak at 532.4 eV again correspond to oxygen double bond and the peak 531.0 eV single oxygen bond in in formic acid  $\text{HO-C=O}$ . In this experiment the second peak mentioned would overshadowed by adsorbed hydroxyls from dissociated water.

From possible interpretations presented above the one assuming the water bound on already adsorbed hydroxyl seems to be more feasible. In experiment with (1×1) surface reconstruction both peaks at 531.4 eV and 532.4 eV are present in all water adsorption experiments ranging from 50 L dosage to deposition of liquid water drop with roughly 1:1 peak-to-peak ratio in all experiments. On the other hand, the carbon C 1s show minimal formic acid carbon signal during dosing water vapor only with increased intensity after water drop experiment. On the (2×1) surface it appears that at low dosage the water dissociate and binds to the surface only as hydroxyl groups. With high pressure experiment and liquid water experiment it seems that there is only partial dissociation with remaining molecular water binding to already adsorbed hydroxyls.

The surface oxygen exchange is phenomena yet to be explained. From the experiment it is apparent that after deposition of liquid water on surface with labeled oxygen <sup>18</sup>O and subsequent heating the sample in order to desorb the hydroxyls bound to surface, the intermixing of lattice and hydroxyl oxygen occurs with roughly same peak-to-peak ratio in LEIS. This experiment was however burdened by contamination a thus explanation of this phenomena is hardly reachable.



## 6 $\alpha$ -Fe<sub>2</sub>O<sub>3</sub> (012) (1×1)-TO-(2×1) SURFACE RECONSTRUCTION TRANSITION

The (1×1)-to-(2×1) surface reconstruction of  $\alpha$ -Fe<sub>2</sub>O<sub>3</sub>(012) was examined using Low Energy Electron Microscopy (LEEM) and Low Energy Electron Diffraction (LEED). The experiment was carried out at CEITEC Nano facility using preparation chamber (base pressure  $p_{\text{base}} = 5 \times 10^{-10}$  mbar) and LEEM chamber (base pressure  $p_{\text{base}} = 1 \times 10^{-10}$  mbar).

### 6.1 Sample preparation

Sample preparation for a LEEM measurement followed the procedure described in 5.1 with 15 min sputtering ( $p_{\text{Ar}} = 1 \times 10^{-6}$  mbar) and 20 min annealing at  $T_{\text{pyrometer}} = 520^\circ\text{C}$  ( $U = 1$  kV,  $I_{\text{emission}} = 25.5$  mA) with oxidation every fifth cycle ( $T_{\text{pyrometer}} = 390^\circ\text{C}$ ,  $p_{\text{O}_2} = 1 \times 10^{-6}$  mbar). For (1×1) surface the oxidation was done right after annealing step to increase size of individual terraces. Prepared samples were then transferred in vacuum into the LEEM setup.

#### 6.1.1 Surface Inclusions

The sample #604 provided for this experiment by surface physics research group of prof. Diebold exhibited surface inclusions of polycrystalline surface among atomically flat traces. These inclusions (Fig. 6.1) covered the majority of the surface making it impossible to perform any meaningful experiment in LEEM. To improve the quality of the surface, the sample was taken into Pulsed Laser Deposition (PLD) setup at TU Vienna. In this setup, the annealing in 1 mbar of O<sub>2</sub> at 800°C. The results can be again seen in Fig. 6.1. It is apparent that while the size of inclusion increased the coverage of the surface is much lower making it possible to perform LEEM experiment on atomically flat terraces.

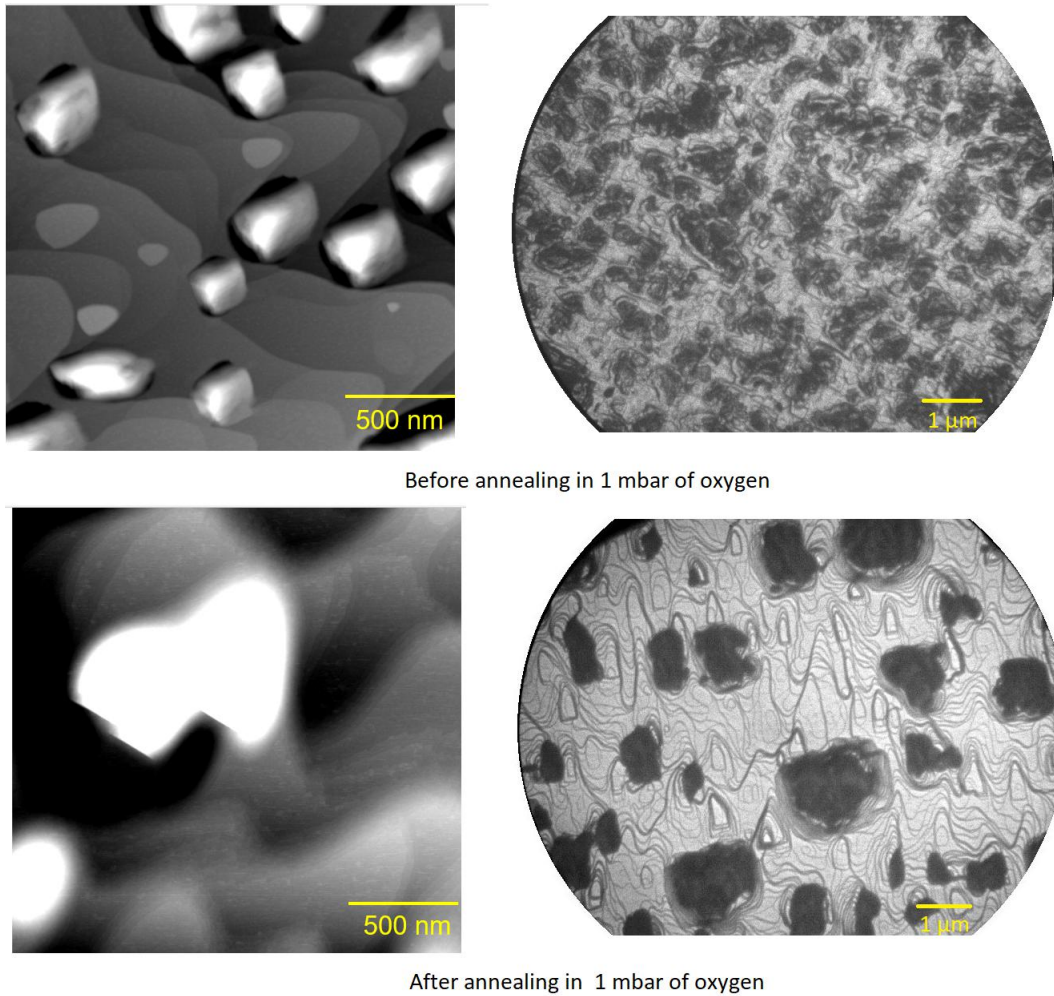


Fig. 6.1: AFM/LEEM images of the surface inclusion. Before annealing in high pressure of oxygen, the inclusion with size of  $\approx 200$  nm in diameter cover majority of the surface. After high pressure annealing the inclusions increased in size with diameter in range of micrometers, but with notably lower coverage of the surface.

## 6.2 $(1\times 1)$ -to- $(2\times 1)$ Surface Reconstruction reduction

The experiment in LEEM was performed on  $(1\times 1)$  surface prepared in LEEM setup by annealing the sample in  $5\times 10^{-7}$  mbar at  $T_{\text{pyrometer}}=380^\circ\text{C}$ . To limit the drift of the image, the crystal was tempered at  $T_{\text{thermocouple}}=350$  K for 20 min. The LEEM was set into diffraction mode observing the pattern until half-order spots of mixed surface started to appear (Fig. 6.2). These weak spots started to appear at around 400 K.

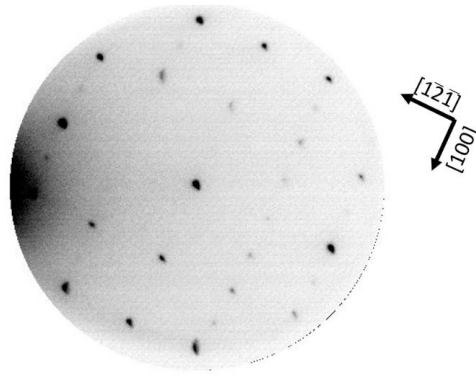


Fig. 6.2: Diffraction pattern of (1×1) surface during annealing. The weak half order spots appear along [100] direction at around 400 K.

After these spots appeared, the bright-field aperture was inserted into position of (0,0) spot and LEEM was switched into real-space mode with energy of beam set to 6.3 eV. The results of the measurement of real-space sample surface are shown in Fig. 6.3. The black areas across the surface represent the inclusions described in 6.1.1. The bright areas are assigned to (2×1), while dark grey areas represent (1×1) reconstruction. It is visible that at beginning of the transformation the (2×1) areas copy the shape and position of edges of atomic terraces and step bunches as well as the areas near the inclusions. In time, these bright areas seem to increase from the edges inwards at earlier points of experiment. After roughly 3100 s and at 500 K (Fig. 6.3) the change in contrast became more gradual rather than sudden. This suggests that the (1×1)-to-(2×1) transition at this point is rather happening evenly on the whole surface rather than step-by-step change from edges of atomic steps towards the center of the terrace. After roughly 4000 s the imaged area exhibits even contrast displaying complete transformation, which was confirmed by (2×1) pattern in diffraction mode.

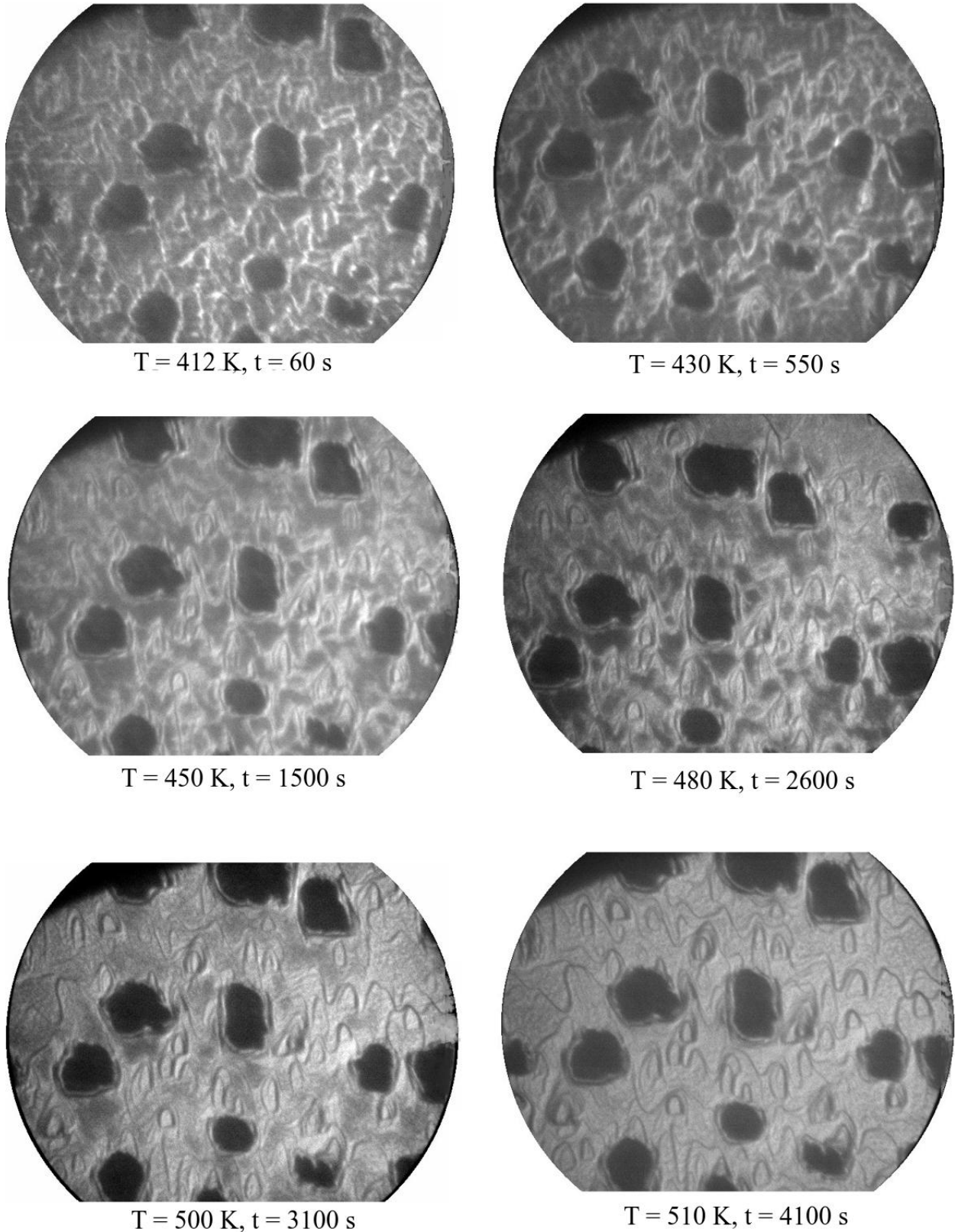


Fig. 6.3: LEEM images of  $(1\times 1)$ -to- $(2\times 1)$  transition measured in bright-field mode ( $10 \mu\text{m}$ ,  $6.3 \text{ eV}$ ). Black islands on images are inclusions of polycrystalline iron oxide. Bright areas depict growing  $(2\times 1)$  reconstruction and dark grey areas receding  $(1\times 1)$  reconstruction.

It has to be noted that electron beam considerably influence observed transformation. In Fig. 6.4 the image taken after the experiment, but shifted the sample by several micrometers is shown. There is evident contrast edge between previously observed and not observed area of the sample. This contrast difference implies that electron beam even at low energies influence the temperature at which the transition occurs.

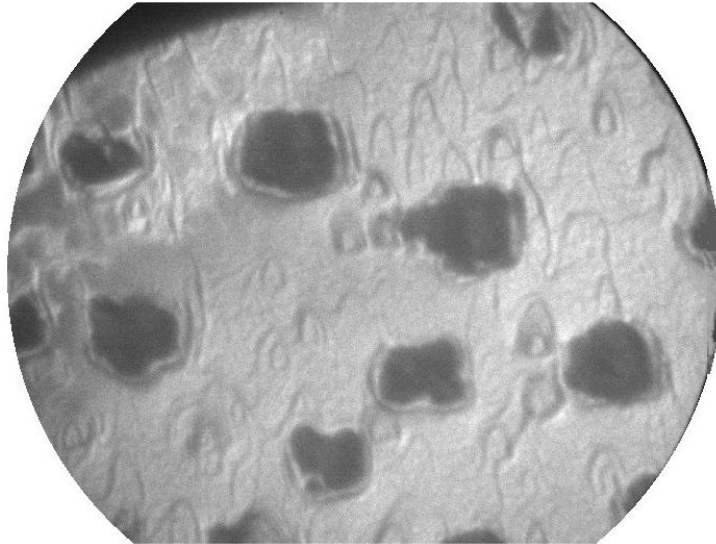


Fig. 6.4: LEEM image(10 $\mu\text{m}$ , 6.3 eV) of previously unobserved area during experiment. On upper left corner there is previously observed area that already undergoes transition, while the rest of the image shows still not transformed (1×1) surface.

This experiment was repeated with measuring at 12.5 eV in bright-mode and at 31.5 eV in dark-field mode with results shown in Fig. 6.5. The measurement contrast is inversed in bright-field mode compared to previous measurement due to different energy of incident beam. Similar to previous case the beam damage seems to play a role in the transition as after image drifted into another position no visible contrast was detected. The dark-field image shows an inverse contrast with (2×1) appearing brighter than areas of (1×1).

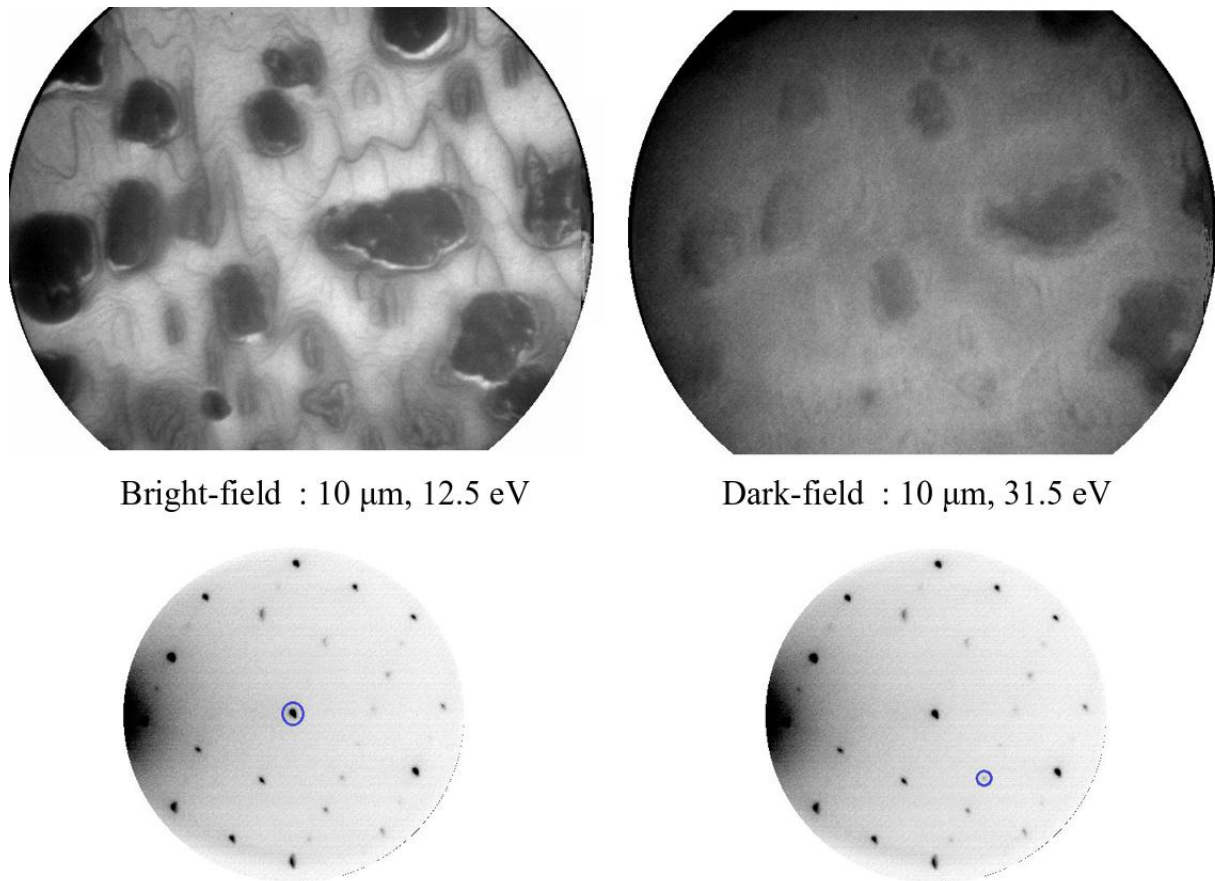
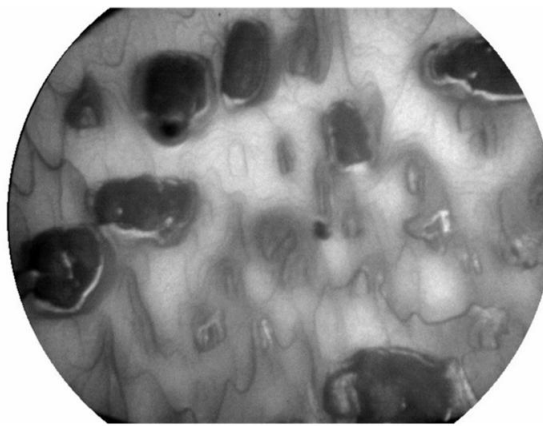
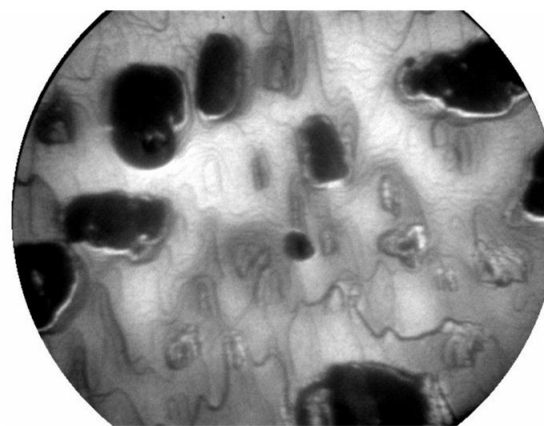


Fig. 6.5: LEEM bright-field and dark-field measurement of  $(1\times 1)$ -to- $(2\times 1)$  transition taken at 470 K. In bright-field the bright areas represent  $(1\times 1)$  surface, while dark areas represent  $(2\times 1)$  surface. Dark-field image taken at same position exhibits reversed contrast of corresponding areas in bright-field. The blue circle around diffraction spots indicates the spot from which the real-space image was taken.

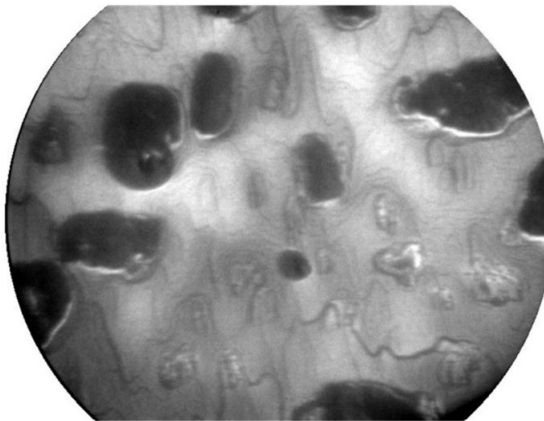
In Fig. 6.6 the results from measuring transition at 12.5 eV are shown. At 470 K surface already seems to be partially transformed. The behavior of this transition seems to correspond with results obtain in previous experiment as it again follow the step edges in begining and it progresses towards the middle of terraces at later stages. In this experiment there was no sudden change in contrast, but rather gradual „fading“ of the brighter areas until uniform contrast is reached (after  $\approx 6000$  s at 470 K)



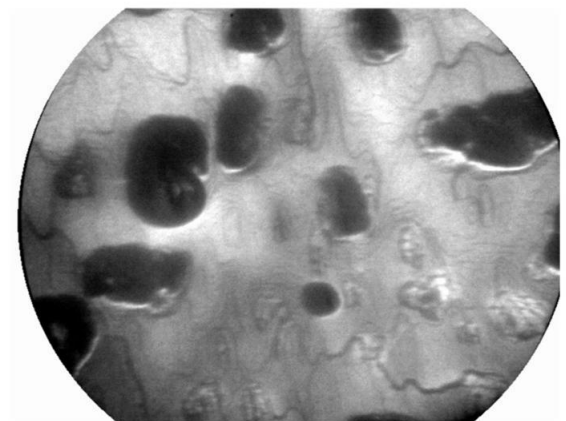
T = 470 K, t = 500 s



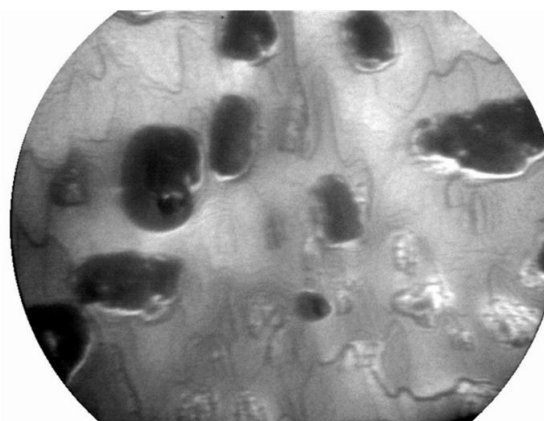
T = 470 K, t = 2000 s



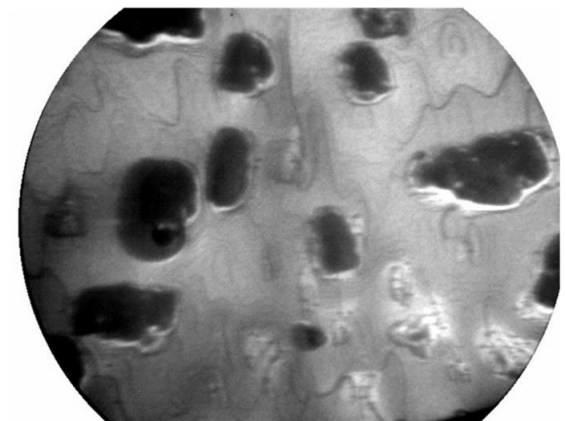
T = 470 K, t = 3000 s



T = 470 K, t = 4000 s



T = 470 K, t = 5000 s



T = 470 K, t = 6000 s

Fig. 6.6: LEEM images of (1×1)-to-(2×1) transition measured in bright-field mode (10  $\mu\text{m}$ , 12.5 eV). Black islands on images are inclusions of polycrystalline iron oxide. Bright areas depict receding (1×1) reconstruction and dark grey areas growing (2×1) reconstruction.

## 6.3 Discussion

The previous studies on  $(1\times 1)$  and  $(2\times 1)$  surface reconstruction were done by Henderson [9, 49, 50] and by Kraushofer [51]. The results from preparation of mixed surface seems to be in agreement with [9] as the same diffraction pattern was achieved, however, at much lower temperatures (400 K) than 600 K reported. This is attributed to electron beam induced damage on the sample as it was observed in experiments in Fig.6.4. It also had to be noted that the temperature sensor in experiment is located on sample stage of the LEEM apparatus and as the sample is heated by electron beam its temperature is considered higher than the one measured.

In real-space images measured at 6.3 eV (Fig. 6.3) the areas assigned to  $(2\times 1)$  reconstruction (bright areas) seem to originate at step edges and near the inclusions or generally defects present on the surface. These areas then seems to increase in areas towards the center of terraces where the  $(1\times 1)$  seem to be more thermodynamically stable and thus remain on the surface longer.

With increased temperature at above  $\approx 470$  K the progression of  $(2\times 1)$  stops and the transition seems to gain much even effect with dark areas of  $(1\times 1)$  slowly fading into uniform contrast indicating the full transition into  $(2\times 1)$  reconstruction. Similar effect was observed in experiment measuring at 470 K with beam energy of 12.5 eV. The corresponding areas in dark-field image confirmed the contrast in bright-field to originate from  $(2\times 1)$  and  $(1\times 1)$  phases. In this experiment the first appearance of  $(2\times 1)$  phase at defect on the surface was confirmed and with some smaller terraces already transformed. The transition of remaining  $(1\times 1)$  surface exhibited gradual change in contrast corresponding with measurements at 6.3 eV, where such behavior was observed above 480 K.

The interpretation of the data presented is rather difficult and more experiments are required for better understanding of the phenomena. One explanation might be that this transition is caused by desorption of the surface oxygen causing charge transfer from  $\text{Fe}^{3+}$  to  $\text{Fe}^{2+}$  and surface reordering. The Henderson [9] claimed that in the process of  $(1\times 1)$ -to- $(2\times 1)$  transition, existing  $(2\times 1)$  domains grow at a faster rate than the rate at which new  $(2\times 1)$  domains are created. This results are consistent with this experiment where the initiation of  $(2\times 1)$  seems to happen at step edges and defects on the surface and then continue inwards to the center of terraces. This change is believed to be induced by beam with consideration of lower temperature of transition and beam damage observed in experiments. The effect of gradual change in contrast while annealing at higher temperatures could be explained by assuming creation of defects like oxygen vacancies at the center of domains. These defects then act as nucleation centers for  $(2\times 1)$  reconstruction and cause the gradual change of contrast visible in LEEM.

## 7 CONCLUSION

This thesis focuses on the design of the new experimental setup for dosing liquid water onto single crystal oxide surfaces to further study of the water interaction with  $\alpha$ -Fe<sub>2</sub>O<sub>3</sub>(012). The new liquid water dosing experiment is based the principle of low vapor pressure of water at low temperatures to achieve transfer the samples in and out of setup at low pressures. Principle of the experiment lays in freezing the water to sufficiently low temperatures to achieve UHV conditions during transfer. Frozen water is then melted and deposited onto sample in closed volume. All materials used in the design are compatible with UHV and including stainless steel, copper, viton and pyrex glass. This setup was also used in study of water interaction with surface of TiO<sub>2</sub> with results and description of this setup reported in [66].

Preliminary tests of the cleanliness of the liquid water was performed on the silver foil. As it was aimed for observing contamination that might be present in stainless steel, cleaning of the carbon was not the highest priority and can be seen in XPS spectrum of the sample. After a liquid water dosing a signal from O 1s can be observed, which most likely belongs to oxygen present in the water but can be also caused by adsorbed carboxyls as there is also increase in carbon signal. In general the preliminary testing of the cleanliness was not done in ideal conditions for the experiment. The increase in carbon contamination can be attributed to higher pressure of unbaked load-lock system ( $\sim 10^{-7}$  mbar) as well as elevated pressures during the experiment ( $\sim 10^{-6}$  mbar). In this range of pressures sample can be contaminated within seconds during its transfer into liquid water dosing chamber and the main chamber.

Second round of testing was done on single crystal Fe<sub>3</sub>O<sub>4</sub>(001). These tests showed the Na contamination on the samples after the first attempt for the experiment. It appears that this contamination gradually vanished by repeating condensation of the water drop. This contamination is thought to come from the pyrex glass containing sodium oxide, which was evaporated during baking of the chamber and adsorbed on the cold finger. XPS spectra of the O 1s region exhibit two distinct peaks corresponding lattice and hydroxyl oxygen. This suggests that water deposited on the sample dissociated and bound to surface as hydroxyl groups. Morphology of the sample surface also showed interesting results. STM images showed chain-like structures adsorbed on the surface. The increasing coverage of the surface by these „chains“ correlate with intensity C 1s of carboxyl groups. Hence these results can be interpreted as adsorbed formic acid on layer of dissociated water.

The interaction of water with  $\alpha$ -Fe<sub>2</sub>O<sub>3</sub>(012) was described for both (1×1) and (2×1) surface reconstructions. The (1×1) reconstruction appears to not be lifted after exposing surface to liquid water. From XPS analysis it is apparent that O 1s signal

is consisting of three distinct peaks. The main peak (530.1 eV) is assigned to lattice oxygen, second (531.4 eV) assigned to adsorbed hydroxyls and third (532.4 eV) assigned to molecular water bound to hydroxyl group on the surface. The (1×1) surface reconstruction exhibits these peaks in different water exposures (ranging from 20 L to liquid water) with roughly same concentration of hydroxyl groups and molecular water. The (2×1) surface exhibits lifted reconstruction into (1×1) at high pressure vapor and liquid water exposure. With low pressure dosage (50 L) the reconstruction remains (2×1), but began to transform to (1×1) after few minutes of exposure to e-beam. The XPS spectra of O 1s reveals that with low pressure water exposure (50 L) only peak at 531.4 eV is present. This suggests that only dissociated water binds to the surface. With high pressure experiment (18 mbar) third peak at 532.4 eV arises suggesting that molecular water binds on adsorbed hydroxyls. After water drop experiment the intensity of 532.4 eV increased even more implying more water adsorbed on the surface.

The last part of this thesis was to investigate (1×1)-to-(2×1) by annealing the sample in UHV. From experiments performed, it seems that transition starts at the atomic step edges and defects on the surface at temperatures around 400 K. While this temperature is not accurate as the temperature sensor is located on a sample stage and not on a sample, it is still lower than expected value. During the experiments it was found that electron beam plays role in initiating the transition as beam damage during experiment was observed. At temperatures higher than 470 K the transition seems to be more gradual, suggesting that at higher temperatures numerous small nucleation sites appear on the terraces transforming the surface more or less uniformly.

---

## BIBLIOGRAPHY

- [1] BERTELSEN, Pernille., Goetz W., Madsen MB., et al. *Magnetic properties experiments on the Mars Exploration Rover Spirit at Gusev crater*. Science, 2004, 305.5685: 827-829.
- [2] BRAGG, W. H. *The structure of magnetite and the spinels*. Nature, 1915, 95.2386:561.
- [3] NÉEL, L. *Proprietes magnetiques des ferrites – ferrimagnetisme et antiferromagnetisme*. Ann.Phys.3, 1948, 137–198.
- [4] ABRAHAM, M. C.; GHOSH, A. *Kinetics of Reduction of Iron Oxides and Ores by Carbon*. 1973.
- [5] BALAJKA, J., ASCHAUER, U. and SELLONI, et. al *Surface Structure of TiO<sub>2</sub> Rutile (011) Exposed to Liquid Water*, The Journal of Physical Chemistry C, 2017, 121.47: 26424-26431.
- [6] SONG, A., SKIBISNSKI, E. S., DeBENEDETTI, W. I. J., et al. *Nanoscale solvation leads to spontaneous formation of a bicarbonate monolayer on rutile (110) under ambient conditions: implications for CO<sub>2</sub> photoreduction*. The Journal of Physical Chemistry C, 2016, 120.17: 9326-9333.
- [7] JAKUB, Z. *UHV-EC Transfer System For Electrochemical Surface Science Studies* [Master's Thesis], Institute of Physical Engineering, Faculty of Mechanical Engineering, Brno University of Technology, 2016, Supervised by Ing. Miroslav Bartošik PhD.
- [8] KRAUSHOFER, F. *The Hematite (012) Surface: Structure and Reactivity* [Master's Thesis], Institute of Applied Physics, Vienna University of Technology, 2017, Supervised by Gareth Parkinson
- [9] HENDERSON, M. A. *Insights into the (1×1)-to-(2×1) phase transition of the α-Fe<sub>2</sub>O<sub>3</sub> (012) surface using EELS, LEED and water TPD*. Surface science, 2002, 515.1: 253-262.
- [10] CAILLETEAU, C., WEIGEL, C., LEDIEU, A., et al. *On the effect of glass composition in the dissolution of glasses by water*. Journal of Non-Crystalline Solids, 2008, 354.2-9: 117-123.
- [11] CORNELL, R. M.; SCHWERTMANN, U. "Crystal Structure." *The iron oxides. Structure, Properties*, 2004: 9-39.

- [12] CORNELL, R. M.; SCHWERTMANN, U. "Thermodynamics of the Fe-O<sub>2</sub>-H<sub>2</sub>O" *The iron oxides. Structure, Properties, Reactions, Occurrences and Uses, Second Edition*, 2004: 185-199.
- [13] KETTELER, G., WEISS, W., RANKE, W., et al. *Bulk and surface phases of iron oxides in an oxygen and water atmosphere at low pressure*. Physical Chemistry Chemical Physics, 2001, 3.6: 1114-1122.
- [14] MAO, H. K. *A discussion of the iron oxides at high pressure with implications for the chemical and thermal evolution of the earth*. Carnegie Inst, 1974, 73: 510-518.
- [15] PARKINSON, Gareth S. *Iron oxide surfaces*. Surface Science Reports, 2016, 71.1: 272-365.
- [16] FISCHER, R. A., CAMPBELL, A. J., LORD, O. T., et al. *Phase transition and metallization of FeO at high pressures and temperatures*. Geophysical Research Letters, 2011, 38.24.
- [17] EBNER, A. D., RITTER, J. A., PLOEHN, H. J., et al. *New magnetic field-enhanced process for the treatment of aqueous wastes*. Separation Science and Technology, 1999, 34.6-7: 1277-1300.
- [18] HONDA, H., KAWABE, A., SHINKAI, M., et al. *Development of chitosan-conjugated magnetite for magnetic cell separation*. Journal of fermentation and bioengineering, 1998, 86.2: 191-196.
- [19] ROGER, J., PONS, J. N., MASSART, R., et al. *Some biomedical applications of ferrofluids*. The European Physical Journal Applied Physics, 1999, 5.3: 321-325.
- [20] ENZEL P., ADELMAN N., BECKMAN K. J., et al. *Preparation of an aqueous-based ferrofluid*. J. Chem. Educ. 76, 1999, 943-948.
- [21] TIEFENAUER, L. X., TSCHIRKY, A., KÜHNE, G., et al. *In vivo evaluation of magnetite nanoparticles for use as a tumor contrast agent in MRI*. Magnetic resonance imaging, 1996, 14.4: 391-402.
- [22] HARUTA, M.. *Size-and support-dependency in the catalysis of gold*. Catalysis today, 1997, 36.1: 153-166.
- [23] FU, Qi; SALTSBURG, H.; FLYTZANI-STEPHANOPOULOS, M.. *Active non-metallic Au and Pt species on ceria-based water-gas shift catalysts*. Science, 2003, 301.5635: 935-938.

- 
- [24] BLIEM, R., McDERMOTT, E., FERSTL, P., et al. *Subsurface cation vacancy stabilization of the magnetite (001) surface*. *Science*, 2014, 346.6214: 1215-1218.
- [25] BLIEM, R., PAVELEC, J., GAMBA, O., et al. *Adsorption and incorporation of transition metals at the magnetite  $Fe_3O_4(001)$  surface*. *Physical Review B*, 2015, 92.7: 075440.
- [26] BLIEM, R., van der HOEVEN, J., ZAVODNY, A. et al. *An Atomic-Scale View of CO and H<sub>2</sub> Oxidation on a Pt/Fe<sub>3</sub>O<sub>4</sub> Model Catalyst*. *Angewandte Chemie International Edition*, 2015, 54.47: 13999-14002.
- [27] PARKINSON, Gareth S., NOVOTNY, Z., ARGENTERO, G., et al. *Carbon monoxide-induced adatom sintering in a Pd-Fe<sub>3</sub>O<sub>4</sub> model catalyst*. *Nature materials*, 2013, 12.8: 724.
- [28] SICKAFUS, Kurt E.; WILLS, John M.; GRIMES, Norman W. *Structure of spinel*. *Journal of the American Ceramic Society*, 1999, 82.12: 3279-3292.
- [29] VERWEY, E. J. W. *Electronic conduction of magnetite (Fe<sub>3</sub>O<sub>4</sub>) and its transition point at low temperatures*. *Nature*, 1939, 144.3642: 327.
- [30] HU, J., CHEN, G., L. O., Irene M. C., *Selective removal of heavy metals from industrial wastewater using maghemite nanoparticle: performance and mechanisms*. *Journal of environmental engineering*, 2006, 132.7: 709-715.
- [31] SOUSA, M. H., RUBIM, J. C., SOBRINHO, P. G., et al. *Biocompatible magnetic fluid precursors based on aspartic and glutamic acid modified maghemite nanostructures*. *Journal of magnetism and magnetic materials*, 2001, 225.1-2: 67-72.
- [32] SANTOS-CARBALLAL, D., et al. *A DFT study of the structures, stabilities and redox behaviour of the major surfaces of magnetite Fe<sub>3</sub>O<sub>4</sub>*. *Physical Chemistry Chemical Physics*, 2014, 16.39: 21082-21097.
- [33] WU, Ch., ROLDAN, A., GRAU-CRESPO, R., et al. *Synthesis of hematite ( $\alpha$ -Fe<sub>2</sub>O<sub>3</sub>) nanorods: diameter-size and shape effects on their applications in magnetism, lithium ion battery, and gas sensors*. *The Journal of Physical Chemistry B*, 2006, 110.36: 17806-17812.
- [34] BLESA, Miguel A.; MORANDO, Pedro J.; REGAZZONI, Alberto E. *Chemical dissolution of metal oxides*. CRC Press, 1994.

- [35] KRETZSCHMAR, R.; STICHER, H. *Transport of humic-coated iron oxide colloids in a sandy soil: Influence of  $\text{Ca}^{2+}$  and trace metals*. Environmental Science & Technology, 1997, 31.12: 3497-3504.
- [36] TARTAJ, P., MORALES, M. P., GONZALES-CARRENO, T. et al. *The iron oxides strike back: from biomedical applications to energy storage devices and photoelectrochemical water splitting*. Advanced Materials, 2011, 23.44: 5243-5249.
- [37] WANG, J.; WHITE, W. B.; ADAIR, James H. *Optical properties of hydrothermally synthesized hematite particulate pigments*. Journal of the American Ceramic Society, 2005, 88.12: 3449-3454.
- [38] IVANOVSKAYA, M., KOTSIKAU, D., FAGLIA, G., et al. *Influence of chemical composition and structural factors of  $\text{Fe}_2\text{O}_3/\text{In}_2\text{O}_3$  sensors on their selectivity and sensitivity to ethanol*. Sensors and Actuators B: Chemical, 2003, 96.3: 498-503.
- [39] ZHOU, H. S., MITO, A., KUNDU, D. et al. *Nonlinear optical susceptibility of  $\text{Fe}_2\text{O}_3$  thin film synthesized by a modified sol-gel method*. Journal of Sol-Gel Science and Technology, 2000, 19.1: 539-541.
- [40] MOCHIZUKI, S. *Electrical conductivity of  $\alpha\text{-Fe}_2\text{O}_3$* . Physica Status Solidi A, 1977, 41.2: 591-594.
- [41] GILBERT, B., FRANDBSEN, C., MAXEY, E. R., et al. *Band-gap measurements of bulk and nanoscale hematite by soft x-ray spectroscopy*. Physical Review B, 2009, 79.3: 035108.
- [42] TAMIRAT, A. G., RICK, J., DUBALE, A. A., et al. *Using hematite for photoelectrochemical water splitting: a review of current progress and challenges*. Nanoscale Horizons, 2016, 1.4: 243-267.
- [43] ZBORIL, R.; MASHLAN, M.; PETRIDIS, D. *Iron (III) oxides from thermal processes synthesis, structural and magnetic properties, Mössbauer spectroscopy characterization, and applications*. Chemistry of Materials, 2002, 14.3: 969-982.
- [44] MORIN, F. J. *Electrical properties of  $\alpha\text{-Fe}_2\text{O}_3$  and  $\alpha\text{-Fe}_2\text{O}_3$  containing titanium*. Physical Review, 1951, 83.5: 1005.
- [45] NAKAU, T. *Electrical conductivity of  $\alpha\text{-Fe}_2\text{O}_3$* . Journal of the Physical Society of Japan, 1960, 15.4: 727-727.

- 
- [46] IORDANOVA, N.; DUPUIS, M.; and ROSSO, Kevin M.. *Charge transport in metal oxides: a theoretical study of hematite  $\alpha\text{-Fe}_2\text{O}_3$* . The Journal of chemical physics 122.14 (2005): 144305.
- [47] GAUTIER-SOYER, M., M. POLLAK, M. HENRIOT, et al. *The  $(1\times 2)$  reconstruction of the  $\alpha\text{-Fe}_2\text{O}_3$  (012) surface*
- [48] LAD, R. J. and V. E. HENRICH. *Structure of  $\alpha\text{-Fe}_2\text{O}_3$  single crystal surfaces following  $\text{Ar}^+$  ion bombardment and annealing in  $\text{O}_2$* . Surface Science. 1988, vol. 193, no. 1-2, pp. 81–93.
- [49] HENDERSON, M. A. *Low temperature oxidation of  $\text{Fe}^{2+}$  surface sites on the  $(2\times 1)$  reconstructed surface of  $\alpha\text{-Fe}_2\text{O}_3(1\bar{1}02)$* . Surface Science. 2010, vol. 604, no. 13- 14, pp. 1197–1201.
- [50] HENDERSON, M. A.; JOYCE, Stephen A.; RUSTAD, James R. *Interaction of water with the  $(1\times 1)$  and  $(2\times 1)$  surfaces of  $\alpha\text{-Fe}_2\text{O}_3(012)$* . Surface Science, 1998, 417.1: 66-81.
- [51] KRAUSHOFER, F., JAKUB, Z., BILCHER, M. et al. *Atomic-Scale Structure of the Hematite  $\alpha\text{-Fe}_2\text{O}_3(012)$  “R-Cut” Surface*. The Journal of Physical Chemistry C, 2018, 122.3: 1657-1669.
- [52] LÜTH, H.. *Surfaces and interfaces of solid materials*. Springer Science & Business Media, 2013.
- [53] BAUER, E. "Low energy electron reflection microscopy." *Proceedings of the Fifth International Congress on Electron Microscopy*. 1962. p. 11-12.
- [54] TELIEPS, W.; BAUER, E. *An analytical reflection and emission UHV surface electron microscope*. *Ultramicroscopy*, 1985, 17.1: 57-65.
- [55] FLEGE, J. I.; TANG, W. X.; ALTMAN, M. S. "Low-Energy Electron Microscopy." *Characterization of materials*, 2012.
- [56] TROMP, R. M., HANNON, J. B., ELLIS, A. W., et al. "A new aberration-corrected, energy-filtered LEEM/PEEM instrument." *I. Principles and design*. *Ultramicroscopy*, 2010, 110.7: 852-861.
- [57] REMPFER, G. F. *A theoretical study of the hyperbolic electron mirror as a correcting element for spherical and chromatic aberration in electron optics*. Journal of Applied Physics, 1990, 67.10: 6027-6040.

- [58] ROSE, H.; PREIKSZAS, D. *Outline of a versatile corrected LEEM*. *Optik*, 1992, 92.1: 31-44.
- [59] GRIFFITH, O. H.; ENGEL, W. *Historical perspective and current trends in emission microscopy, mirror electron microscopy and low-energy electron microscopy: an introduction to the proceedings of the second international symposium and workshop on emission microscopy and related techniques*. *Ultra-microscopy*, 1991, 36.1-3: 1-28.
- [60] BAUER, E. *LEEM basics*. *Surface Review and Letters*, 1998, 5.06: 1275-1286.
- [61] ČEČHAL, J. *Analysis of the Surfaces and thin Films by X-ray Photoelectron Spectroscopy* [Dissertation Thesis], Brno University of Technology, Faculty of Mechanical Engineering, 2006
- [62] *Vapor pressure calculator* [online], Accessed on 9.1.2018, Available at: [https://www.iap.tuwien.ac.at/www/surface/vapor\\_pressure](https://www.iap.tuwien.ac.at/www/surface/vapor_pressure)
- [63] KNIPE, S. W., MYCROFT, J. R., PRATT, A. R., et al. *X-ray photoelectron spectroscopic study of water adsorption on iron sulphide minerals*. *Geochimica et Cosmochimica Acta*, 1995, 59.6: 1079-1090.
- [64] ONISHI, H., ARUGA, T., EGAWA, CH., et al. *Adsorption of CH<sub>3</sub>OH, HCOOH and SO<sub>2</sub> on TiO<sub>2</sub>(110) and stepped TiO<sub>2</sub>(441) surfaces*. *Surface science*, 1988, 193.1-2: 33-46.
- [65] BOUDON, J., PAPA, A., PARIS, J., et al. *Titanate nanotubes as a versatile platform for nanomedicine*. *Nanomedicine*, 2014, 403: 403.
- [66] BALAJKA, J., HINES, M.A., DeBENEDETTI, W.J.I, et al. *High Affinity Adsorption leads to Molecularly Ordered Interfaces on Model TiO<sub>2</sub> Photocatalysts in Air and Solution*. *Science*, 2018, [under review (23.05.2018)]
- [67] BRONGERSMA, H. H., GREHL, T., van HAL, P. D., et al. *High-sensitivity and high-resolution low-energy ion scattering*. *Vacuum*, 2010, 84.8: 1005-1007.
- [68] CZANDERNA, A.W; HERCULES D. M. . "Ion Spectroscopies for Surface Analysis." *Methods of Surface Characterization*. Springer, Boston, MA, 1991.
- [69] ALFORD, T. L.; FELDMAN, L. C.; MAYER, James W. "Atomic Collisions and Backscattering Spectrometry." *Fundamentals of Nanoscale Film Analysis*, 2007, 12-33.

- [70] BINNIG, G., ROHRER, H., GERBER, CH., et al. *Tunneling through a controllable vacuum gap*. Applied Physics Letters, 1982, 40.2: 178-180.
- [71] BLANCO, J. M.; FLORES, F.; PÉREZ, R. *STM-theory: Image potential, chemistry and surface relaxation*. Progress in surface science, 2006, 81.10-12: 403-443.
- [72] HOFER, W. A. Challenges and errors: Interpreting high resolution images in scanning tunneling microscopy. Progress in Surface Science, 2003, 71.5-8: 147-183.
- [73] CHEN, C. J. *Introduction to scanning tunneling microscopy*. Oxford University Press on Demand, 1993.
- [74] WIESENDANGER, R. (ed.). *Scanning probe microscopy: Analytical Methods*. Springer Science & Business Media, 1998.



---

## LIST OF SYMBOLS, PHYSICAL CONSTANTS AND ABBREVIATIONS

UHV *Ultra high vacuum*

AM *Air mass coefficient*

LEED *Low Energy Electron Diffraction*

LEEM *Low Energy Electron Microscopy*

CEITEC *Central European Insitute of Technology*

CCD *Coupled Charge Device*

SEM *Scanning Electron Microscopy*

TEM *Transmission Electron Microscopy*

MEM *Mirror Electron Microscopy*

XPS *X-ray Photoelectron Spectroscopy*

FAT *Fixed Analyzer Transmission*

FRR *Fixed Retard Ratio*

KF *Klein Flange*

CF *ConFlat*

PTFE *Polytetrafluoroethylene*

PEEK *Polyether ether ketone*

